

ARO Contract DAAG55-98-C-0044
Effective Date 22 June 1998
Requisition: P-39062-MA-SDI
TITLE: ADAPTIVE RF SENSING

US Army Research Office
ATTN: AMXRO-ICA (Johnson)
P.O. Box 1211 Research Triangle Park, NC 27709-2211

COR: US Army Research Office
ATTN: Dr. Robert Launer
Mathematical and Computer Sciences Division
P.O. Box 12211
Research Triangle Park, NC 27709-2211

FINAL TECHNICAL REPORT

Terence W. Barrett, Ph.D., BSEI, 1453 Beulah Road, Vienna, VA 22182
Tel: 703-759-4518; E-Mail: barrett506@aol.com

June 20th, 1999

Contents:

1.0 Preliminaries

- 1.1 Definition of the Scientific Problem
- 1.2 The Aim
- 1.3 State of the Art Benchmark from which BSEI Research Proceeds
- 1.4 Deficiencies in State of the Art Addressed by BSEI Research
- 1.5 Implementation by BMDO
- 1.6 What is new, innovative in BSEI's research results and what are the implications?
- 1.7 Implications of this research
- 1.8 Future work
- 1.9 Future needs

2.0 Summary of Results of Contract DAAG55-98-C-0044

3.0 Continuous Gabor Wavelets

4.0 Ambiguity Function.

5.0 Wigner-Ville Distribution.

6.0 Wavelets compared with spectrogram

- 6.1 Mexican hat wavelet.
- 6.2 Local Regularity of signals and Gaussian differential wavelets.
- 6.3 Spectrogram.

7.0 Zak Transform

- 7.1 Zak Transform Analysis
- 7.2 Relation of Zak Transform to Gabor Transform
- 7.3 Balian-Low Theorem
- 7.4 Exemplars

8.0 Adaptive Methods

- 8.1 Adaptive Gabor Representation (AGR).
- 8.2 Gabor Wavelet (constant Q).
- 8.3 Wigner-Ville of the AGR.

9.0 The Constant Q Gabor Wavelet.

- 9.1 Numerical Tests.

10.0 Extension of the Gabor Transform (CQOW)

19991101 061

DISTRIBUTION STATEMENT A
Approved for Public Release
Distribution Unlimited

REPORT DOCUMENTATION PAGE

Form Approved
OMB NO. 0704-0188

Public reporting burden for this collection of information is estimated to average 1 hour per response, including the time for reviewing instructions, searching existing data sources, gathering and maintaining the data needed, and completing and reviewing the collection of information. Send comment regarding this burden estimate or any other aspect of this collection of information, including suggestions for reducing this burden, to Washington Headquarters Services, Directorate for Information Operations and Reports, 1215 Jefferson Davis Highway, Suite 1204, Arlington, VA 22202-4302, and to the Office of Management and Budget, Paperwork Reduction Project (0704-0188), Washington, DC 20503.

1. AGENCY USE ONLY (Leave blank)		2. REPORT DATE 20th June 99	3. REPORT TYPE AND DATES COVERED Final Technical Rept, 21 June 98 - 20 June 99
4. TITLE AND SUBTITLE Adaptive RF Sensing			5. FUNDING NUMBERS DAAG55-98-C-0044
6. AUTHOR(S) Terence W. Barrett, Ph.D.			
7. PERFORMING ORGANIZATION NAMES(S) AND ADDRESS(ES) BSEI 1453 Beulah Road Vienna, VA 22182			8. PERFORMING ORGANIZATION REPORT NUMBER 12
9. SPONSORING / MONITORING AGENCY NAME(S) AND ADDRESS(ES) U.S. Army Research Office P.O. Box 12211 Research Triangle Park,, NC 27709-2211			10. SPONSORING / MONITORING AGENCY REPORT NUMBER ARO39062.1-MA-SD1
11. SUPPLEMENTARY NOTES The views, opinions and/or findings contained in this report are those of the author(s) and should not be construed as an official Department of the Army position, policy or decision, unless so designated by other documentation.			
12a. DISTRIBUTION / AVAILABILITY STATEMENT Approved for public release; distribution unlimited.			12 b. DISTRIBUTION CODE
13. ABSTRACT (Maximum 200 words) We have sought to either identify or create methods different from state-of-the-art for solving the BMDO problem of providing an ultrahigh resolution active sensor/radar which can identify missile from decoy. We advocate sensor/radar systems using pulses shorter than the length of the target, adaptive time-frequency analysis methods which preserve target backscattering centers and resonances, and pattern identification of target and decoy. In particular, we have created • extensions of the Gabor transform (CQOW) • adaptive methods • methods involving the instantaneous phase • mutual information methods • Zak transform methods, which can achieve preserve target backscattering and target resonance and provide the input for procedures permitting pattern identification of target and decoy. Furthermore, we have created methods using • the bootstrap • fractal dimension • Fano number • deterministic chaos methodologies, to provide precision is identification of target and decoy. Our recommendation for the next step to be taken is to implement these new methods in emulation or real-time systems.			
14. SUBJECT TERMS Wavelet filters, Gabor transform, Weber function, Paraunitary properties, Bootstrap method; Fano factor; fractal dimension; deterministic chaos.			15. NUMBER OF PAGES 130
			16. PRICE CODE
17. SECURITY CLASSIFICATION OR REPORT UNCLASSIFIED	18. SECURITY CLASSIFICATION OF THIS PAGE UNCLASSIFIED	19. SECURITY CLASSIFICATION OF ABSTRACT UNCLASSIFIED	20. LIMITATION OF ABSTRACT UL

such a method and it requires the transmitted signal in space to be less than the length of the target.

If the transmitted signal in space is less than the length of the target, the signal return from the target decomposes into its individual scattering components. That is to say, there is a unique signature from the nose, the fins, the tail, etc. Furthermore, if the signal return is not averaged but is received as a fast sampled time series preserving amplitude, phase, frequency and perhaps polarization modulations, i.e., is homodyned, as opposed to heterodyned, the speed of the currents set up on the surface of the target would have a unique signature. In other words, there is reason to expect that the surface material composition would differentiate signals returns from targets identical in size but differing in material composition. In which case, a signature would be available distinguishing a missile from a decoy, which has a different material composition. Also, the imaging time is far less than that required by SAR and ISAR and could be on the order of one pulse transmit time.

Given a radar which transmits signals shorter than the length of designated targets, which - as it performs more than just ranging and detection - might be called a sensor, the next problem to be addressed is that of return signal analysis. Because in SAR, ISAR and very short pulse radar the target consists of a number of scatterers - discontinuities, cavities, corners, etc. and each provides a different backscattering behavior, a first set of signature characteristics identifying the target is the backscattering (from a multiple scatterer). A second set of signature characteristics consists of the resonances of the target. To preserve in analysis the first set of characteristics requires precision in the time dimension; to preserve in analysis the second set of characteristics requires precision in the frequency dimension. The state of the art in analysis would be to use wavelet methods for precision in the time dimension and Fourier analysis for precision in the frequency dimension. The present work's objective is to provide (adaptive) methods which provide precision in both the time *and* frequency dimensions.

The requirement of analysis precision in *both* time and frequency is occasioned by other factors. A very short pulse interacting with a larger target elicits three types of responses: (1) the early time response; (2) the resonance response; and (3) the late time response. The first, the early time response, is due to currents being set up on the surface of the target and is target aspect-dependent. The second, the resonance response, is dependent on the length of the target and is aspect-independent in harmonic components but aspect-dependent with respect to the amplitude of those harmonic components. The third, the late time response, is due to the delayed "ring down" of the target after "painting" by the signal and its physics is similar to that of the resonance response. Clearly, target identification should be based on a mix of the three kinds of response with their differing aspect dependencies.

Another major departure of the present work from the state of the art is in the nature of the method of target identification. The method is neither level detection as in conventional radar, nor imaging as in conventional SAR and ISAR. The new method is pattern identification. Given time-frequency methods preserving both the backscattering center signatures and resonances from a multiple scattering target, the identification method would be by pattern identification in the time-frequency plane.

In summary, we offer methods different from state-of-the-art for solving the BMDO problem of providing an ultrahigh resolution sensor which can identify missile from decoy. We advocate pulses shorter than the length of the target, adaptive time-frequency analysis methods which preserve target backscattering centers and resonances, and pattern identification of target and decoy.

1.4 Deficiencies in State of the Art Addressed by BSEI Research

BMDO lacks an active high resolution sensor as well as the capability of detecting missiles from debris and decoys. A short pulse sensor is smaller in size, weight and power than conventional radars and requires a smaller antenna. Therefore a short pulse sensor can be deployed either on satellites or as a missile seeker.

The state of the art in conventional radars can only achieve high resolution in the SAR or ISAR configuration. The former requires a stationary target with a moving radar and the latter requires a moving target with a stationary radar. A short pulse system does not have such requirements to achieve high resolution. Denied the SAR and ISAR configurations, conventional radars achieve target identification by level detection. Therefore a target missile cannot be distinguished from a decoy. A short pulse system achieves a signal return which can be analyzed using time-frequency methods and target can be distinguished from decoy by pattern matching techniques.

1.5 Implementation by BMDO

The implementation of a short pulses sensor/radar together with the correct time-frequency approaches to processing is straightforward if a development program is initiated. Alternatively, simulation and modeling can take place using the VDHTB testbed.

1.6 What is new, innovative in BSEI's research results and what are the implications?

1.6.1 New methods for achieving discrimination of both frequency-dependent aspects of the target and time-dependent scattering centers.

The Adaptive Gabor Representation (AGR) was used to analyze a radar signal return in two forms: the functions were either varying Q or constant Q . We found the constant Q form is optimum. Frequency hopping signals as well as monocycle pulses were analyzed with the AGR and the *Combined* Wigner-Ville Distribution of the AGR calculated. It was shown that with all frequency components combined the frequency components of the signal can be identified, but not the pulse. However, when the *Combined* Wigner-Ville representation of the AGR is calculated using only the high frequency components of the latter, it was seen that the monocycle can be detected. Thus, these methods seems entirely appropriate for detecting the frequency-dependent and the time-dependent (transient) scattering centers of targets.

The AGR and the Combined and Single Wigner-Ville Distribution of the AGR were calculated for frequency hopping signals, pulses and radar return signals. The AGR requires finding the optimum wavelet center frequency, optimum dwell and optimum modulating envelope. The hypothesis under test was that whereas the AGR has been viewed as an optimization with respect to three variables: α_p , t_0 and f_0 , with α_p setting the envelope size independently of the other two variables, use of a constant Q Gabor wavelet would permit an efficient optimization using only one variable - α_p - with the other signal parameters functions of that one variable. It is shown that the constant Q Gabor wavelet with $f_0 \cdot t_0 = \Delta f \cdot \Delta t = 1/2$, is optimum and that only one variable is required for optimization.

1.6.2 New wavelet analysis

A new wavelet analysis was developed based on orthogonal parabolic cylinder or Weber functions of increasing level described by the expansions: $\Delta f \cdot \Delta t = f_0 \cdot t_0 = 1/2 (2n +$

1), $n=0,1,2,\dots$ (i.e., Constant Q Orthogonal Weber Function Wavelets (WFWs). Using a frequency hopping and pulse test signals, these wavelets are able to detect both resonance and pulse scattering features. Using scattergram plots between three levels of wavelets and two scale dilations, unique features of both the test signal and radar return signals can be demonstrated. This research is unique in two respects: using orthogonal wavelets of different levels and in the scatterogram cross-comparison of three levels of analysis, which can provide unique signatures for targets. In the case of the test signal of a frequency hopping signal, plus a pulse, it is seen that discernible cyclic patterns occur which may be correlated with the number of frequencies in the signal - four. In the case of the radar return test signal, it is seen that recognizable helical patterns occur, which may provide a unique signature for targets.

Using a frequency hopping and pulse test signals, WFWs permit detection of both resonance and pulse scattering features. The characteristics of these wavelets are based on IIF filter principles. It is customary to believe that a discrete time scaling (low pass) wavelet is first necessary to obtain the discrete time (high pass) wavelet. Here we show that the expansion method permits an estimate of the continuous time high pass wavelet from the summed Fourier spectra of the expansions, $n = 1, 2, \dots \infty$. Future work will examine whether repeated analysis of the original signal by higher order wavelets is equivalent to the customary method of using but one scaling function and one wavelet with signal decimation.

1.6.3 Instantaneous phase information.

Instantaneous phase information was obtained from application of wavelet analysis. A detailed thumbprint of a complex (target return) signal can be obtained which can be used as data supporting a detailed wavelet modulus description of the same signal. A result is obtained by calculating the differential phase which also provides supporting data. There are also optimum dilations for providing correlated measures.

The probability distribution function for the target return signal processed with a specific dilation of the wavelet and the mutual information for two dilations also provides supporting data to the modulus thumbprint of the signal.

The phase information and mutual information provide excellent supporting data to that providing by the wavelet modulus. In combination a more detailed analysis of target information is possible.

1.6.4 Target Differentiation.

Differentiation of two target return signals was accomplished using (1) wavelet processing and (2) fractal analysis of the results of that wavelet analysis. Log-Log plots (amplitude versus filter scale) revealed stable distributions (as opposed to asymptotically Gaussian distribution) behavior - increasing in the case of one signal, and decreasing in the case of the other. This is a fractal property. The computed fractional dimension per time bin revealed clear differences between the two signals. The Fano factors for means across filters and for each time bin were also computed. There is a clear difference in the Fano factor patterns generated permitting the differentiation of the signals. Thus, fractal analysis appears to be a promising approach to differentiating signals and will be further explored in future months.

1.6.5 Nonlinear Collective Exxcitations.

Analyses in terms of (a) higher-order symmetries; (b) differential forms; and (c) group theoretic, and formulations in electromagnetic theory of the role of the A-field in (a) nonlinear collective excitations in a 2-dimensional electron gas; and (b) solitons in new SAW devices and heterostructures in general. The method of generation of modulated

TeraHertz pulses utilizes a plasma mirror dependent on the formation of soliton transmission.

1.6.6 The Bootstrap Method.

The Bootstrap method was used for estimating the accuracy of a parameter estimator taken, in the instances addressed, as radar signal returns. We demonstrate - for the first time to our knowledge - that the technique can be applied to distinguish targets. We also apply techniques taken from fractal theory and deterministic chaos theory to show that radar returns have both a fractal nature and are not time series produced by a random mechanism, but rather by a deterministic chaotic mechanism. We are able to show that the fractal properties of the power spectra, the variance and Fano Factor distinguish between two target returns. Use of embedding dimensional analysis also reveals the deterministic chaotic, as opposed to random, nature of the radar returns.

1.7 Implications of this research

This research provides time-frequency methods for analyzing sensor/radar signal returns to achieve ultrahigh resolution and the possibility of distinguishing target from decoy. The research also indicates the advantage of deploying a short pulse sensor/radar, in which the pulse is shorter than the length of the target.

1.8 Future work

The completed work addressed a number of new research areas which require much more development time than was given in the limited time available in the present contract. These areas include: Constant Q Orthogonal Weber Function Wavelets, application of the Bootstrap method, fractal analysis methods and the Adaptive Gabor representation. The development of these areas can take place in a simulation environment.

1.9 Future needs

To conduct future work in these areas there are two requirements: (1) a source of realistic signal returns from missiles and decoys; and (2) a testbed implementation, e.g., the VDHTB. Alternative to the testbed implementation using computer analysis of the signals, the algorithms described in the present work could be implemented in ASIC or hardware designs. However, the preference would be to firstly test the algorithms in a testbed and then proceed to hardware implementation.

2.0 Summary of Results of Contract DAAG55-98-C-0044

These reported investigations of time-frequency representations of radar signals were carried out with a view to accurately detect small differences between radar returns. This objective is congruent with BMDO objectives of being able to detect target from decoy.

2.1 Representative radar data was analyzed with (1) continuous Gabor wavelets; (2) ambiguity functions; and (3) Wigner-Ville distributions, in order to determine the optimum form of analysis for the RF sensor returns.

2.2 We are able to show the superiority of the wavelet method and the usefulness of Gaussian differential wavelets in detecting local differences in the smoothness of the decay

of transitions in the signal. The capability of detecting such differences may be critical in discriminating targets from decoys. In the case of the spectrogram, we showed that the method can pick out well the onset and offset of the various modulations in the signal. However, due to the fact that the window is constant (even although the modulated frequency of the kernel is changing), the spectrogram provides a biased representation of the signal as the sampling window excludes the influence of signal components outside the unchanging windowed "box". The spectrogram is thus not an optimum representation of signals and future work will demonstrate how to amend the spectrogram method to obtain wavelet representations from a similar commencement.

2.3 New methods were developed for achieving heightened discrimination capability. The action of the Zak Transform in achieving this aim was investigated using a radar return signal exemplar with variance of the Zak summing variable k . It was shown that discrimination capability of fine structure is lost as the range of k increases. In order to investigate improvements in discrimination capability, the Zak transform was performed not on the radar exemplar but on the radar exemplar after Gabor analysis with kernels of various sizes. It was shown that there are distinctive patterns for each of the kernels used. Therefore a radar return signal can be analyzed into a 4-dimensional pattern signature when the results of the analysis patterns of multiple kernels are summed. This method holds promise for increasing fine discrimination capability.

2.4 New methods were developed for achieving discrimination of both frequency-dependent aspects of the target and time-dependent scattering centers. The Adaptive Gabor Representation (AGR) was used to analyze a radar signal return in two forms: the functions were either varying Q or constant Q . We found the constant Q form appears optimum. Frequency hopping signals as well as monocyte pulses were analyzed with the AGR and the *Combined* Wigner-Ville Distribution of the AGR calculated. It was shown that with all frequency components combined the frequency components of the signal can be identified, but not the pulse. However, when the *Combined* Wigner-Ville representation of the AGR is calculated using only the high frequency components of the latter, it was seen that the monocyte can be detected. Thus, these methods seems entirely appropriate for detecting the frequency-dependent and the time-dependent (transient) scattering centers of targets.

2.5 New methods continued to be developed for achieving discrimination of both frequency-dependent aspects of the target and time-dependent scattering centers. The Adaptive Gabor Representation (AGR) and the Combined and Single Wigner-Ville Distribution of the AGR were calculated for frequency hopping signals, pulses and radar return signals. The AGR requires finding the optimum wavelet center frequency, optimum dwell and optimum modulating envelope. The hypothesis under test was that whereas the AGR has been viewed as an optimization with respect to three variables: α_p , t_0 and f_0 , with α_p setting the envelope size independently of the other two variables, use of a constant Q Gabor wavelet would permit an efficient optimization using only one variable - α_p - with the other signal parameters functions of that one variable. It is shown that the constant Q Gabor wavelet with $f_0 \cdot t_0 = \Delta f \cdot \Delta t = 1/2$, is optimum and that only one variable is required for optimization.

2.6 Investigations were initiated of wavelets based on orthogonal parabolic cylinder or Weber functions of increasing level described by the expansions: $\Delta f \cdot \Delta t = f_0 \cdot t_0 = 1/2 (2n + 1)$, $n = 0, 1, 2, \dots$ (i.e., Constant Q Orthogonal Weber Function Wavelets (CQOWs)). Using a frequency hopping and pulse test signals, these wavelets are able to detect both resonance and pulse scattering features. Using scattergram plots between three levels of wavelets and two scale dilations, unique features of both the test signal and radar return

signals can be demonstrated. This research is unique in two respects: using orthogonal wavelets of different levels and in the scatterogram cross-comparison of three levels of analysis, which can provide unique signatures for targets. In the case of the test signal of a frequency hopping signal, plus a pulse, it is seen that discernible cyclic patterns occur which may be correlated with the number of frequencies in the signal - four. In the case of the radar return test signal, it is seen that recognizable helical patterns occur, which may provide a unique signature for targets.

2.7 Further investigation of CQOWs showed that using a frequency hopping and pulse test signals, these wavelets are able to detect both resonance and pulse scattering features. The characteristics of these wavelets are based on IIF filter principles. It is customary to believe that a discrete time scaling (low pass) wavelet is first necessary to obtain the discrete time (high pass) wavelet. Here we show that the expansion method permits an estimate of the continuous time high pass wavelet from the summed Fourier spectra of the expansions, $n = 1, 2, \dots \infty$. Future work will examine whether repeated analysis of the original signal by higher order wavelets is equivalent to the customary method of using but one scaling function and one wavelet with signal decimation.

2.8 Methods were developed addressing instantaneous phase information obtainable from application of wavelet analysis. We show that a detailed thumbprint of a complex (target return) signal can be obtained which can be used as data supporting a detailed wavelet modulus description of the same signal. We also show a result from calculating the differential phase which also provides supporting data. It is also shown that there are optimum dilations for providing correlated measures.

We also calculated the probability distribution function for the target return signal processed with a specific dilation of the wavelet and the mutual information for two dilations. This form of analysis also provides supporting data to the modulus thumbprint of the signal.

The phase information and mutual information provide excellent supporting data to that provided by the wavelet modulus. In combination a more detailed analysis of target information is possible.

2.9 Methods were developed addressing the differentiation of two target return signals using (1) wavelet processing and (2) fractal analysis of the results of that wavelet analysis. Log-Log plots (amplitude versus filter scale) revealed stable distributions (as opposed to asymptotically Gaussian distribution) behavior - increasing in the case of one signal, and decreasing in the case of the other. This is a fractal property. The computed fractional dimension per time bin revealed clear differences between the two signals. The Fano factors for means across filters and for each time bin were also computed. There is a clear difference in the Fano factor patterns generated permitting the differentiation of the signals. Thus, fractal analysis appears to be a promising approach to differentiating signals and will be further explored in future work.

2.10 Analytical methods were developed in terms of (a) higher-order symmetries; (b) differential forms; and (c) group theoretic, and formulations in electromagnetic theory of the role of the A -field in (a) nonlinear collective excitations in a 2-dimensional electron gas; and (b) solitons in new SAW devices and heterostructures in general. The method of generation of modulated TeraHertz pulses utilizes a plasma mirror dependent on the formation of soliton transmission. Therefore an analysis was commenced of such soliton transmissions using the various approaches described.

2.11 Analytical methods were developed based on the Bootstrap method for estimating the accuracy of a parameter estimator taken, in the instances addressed, as radar signal returns. Here, we show - for the first time to our knowledge - that the technique can be applied to

distinguish targets. We also apply techniques taken from fractal theory and deterministic chaos theory to show that radar returns have both a fractal nature and are not time series produced by a random mechanism, but rather by a deterministic chaotic mechanism. We are able to show that the fractal properties of the power spectra, the variance and Fano Factor distinguish between two target returns. Use of embedding dimensional analysis also reveals the deterministic chaotic, as opposed to random, nature of the radar returns.

3.0 Continuous Gabor Wavelets

The Gabor wavelet kernel is:

$$\psi = \text{Exp}[-\xi_1 t^2] \times \text{Cos}(\xi_2 t).$$

and in general:

$$\psi(t) = g(t) \text{Exp}[i\xi_2 t],$$

where $g(t)$ is a Gaussian window:

$$g(t) = \frac{1}{(\sigma^2 \pi)^{1/4}} \text{Exp}\left[-\frac{t^2}{2\sigma^2}\right],$$

with $\xi_1 = \frac{1}{2\sigma^2}$.

The continuous Gabor wavelet transform is then defined as:

$$Wf(\tau, s) = \int_{-\infty}^{+\infty} f(t) \frac{1}{\sqrt{s}} \psi * \left(\frac{t - \tau}{s} \right) dt.$$

Two examples of radar signal returns are shown in Figs. 3.1A and 3.2A. The Gabor transforms, $Wf(\tau, s)$, are shown in Figs. 3.1B-D and 3.2B-D, respectively. It can be seen that the two signal returns can be identified by 3-D pattern detection.

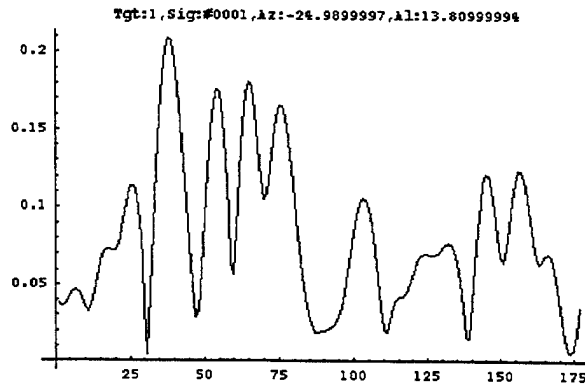


Fig. 3.1A. 1st example of radar signal return.

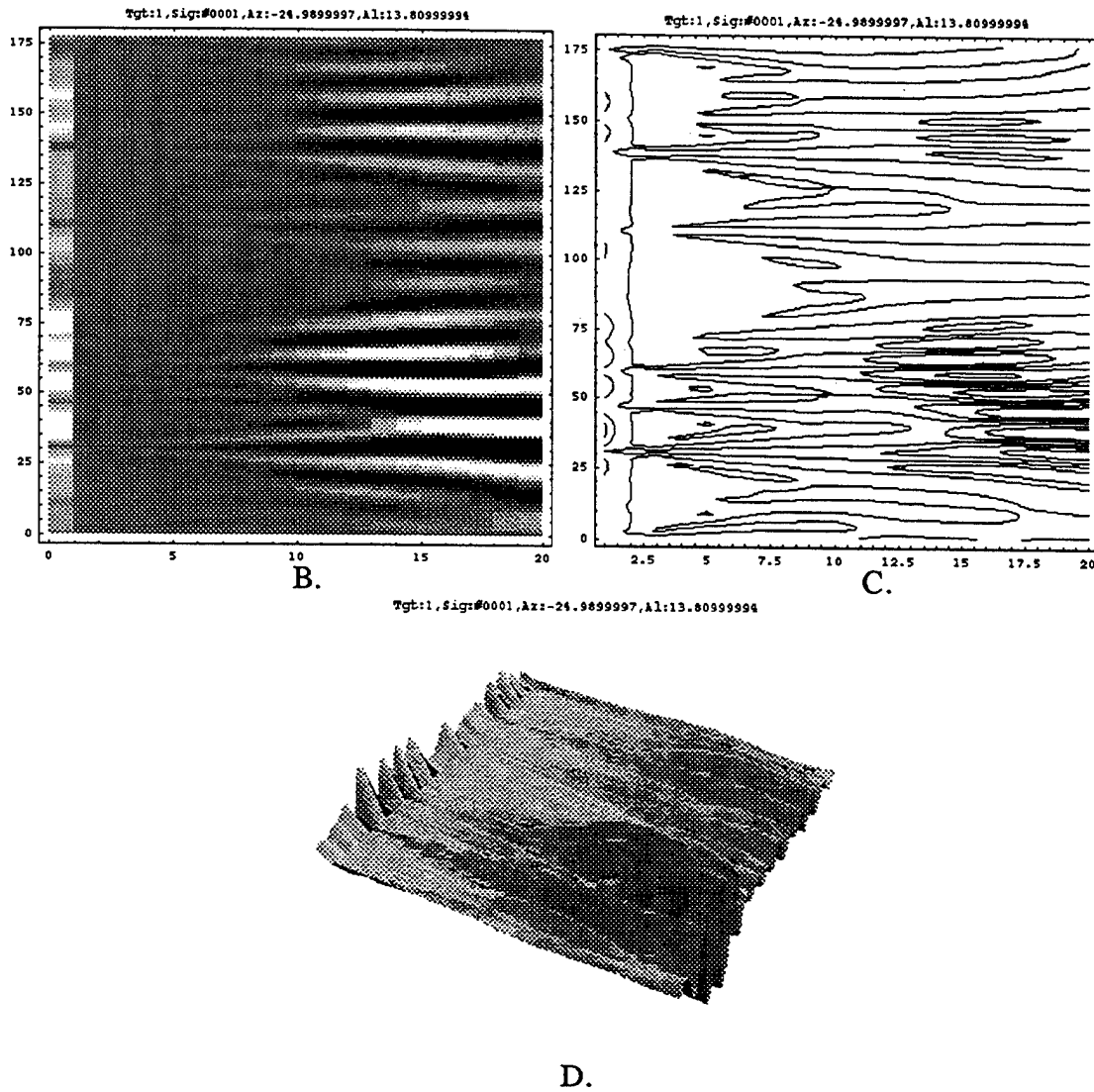


Fig. 3.1B, C &D. 1st example of radar signal return after Gabor wavelet filtering - 20 filters used.

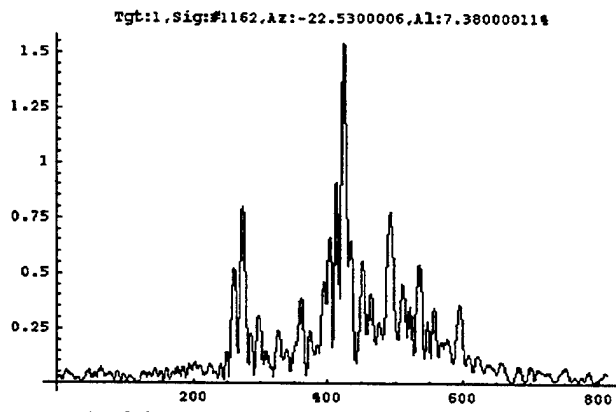
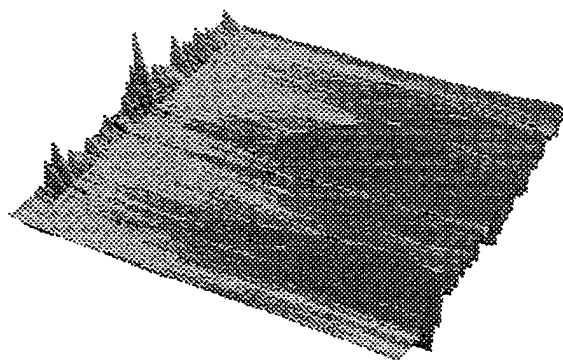
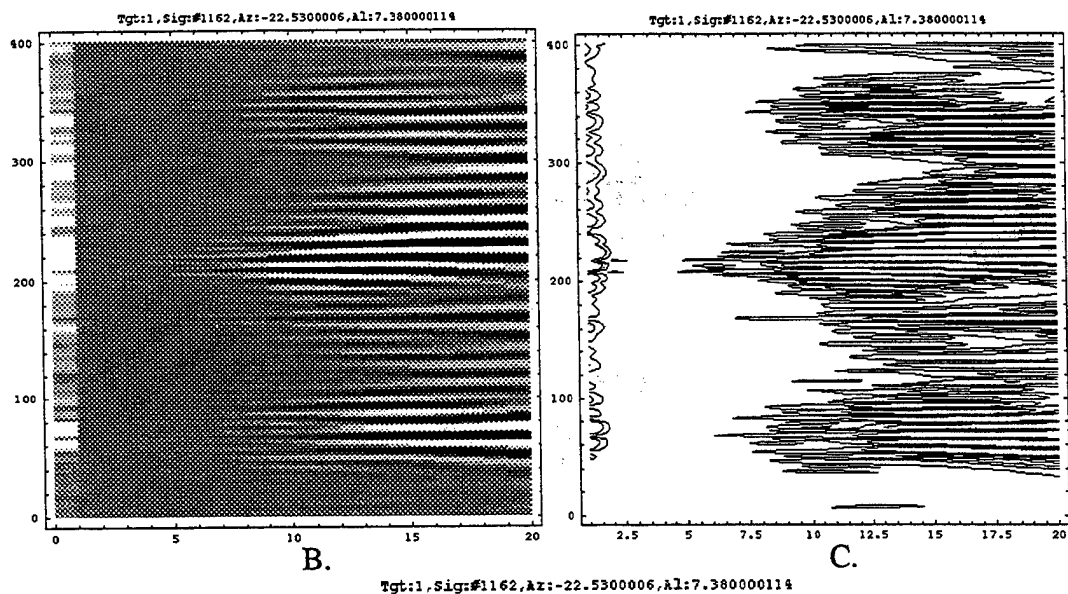


Fig. 3.2A. 2nd example of radar signal return.



D.

Fig. 3,2B, C & D. 2nd example of radar signal return after Gabor wavelet filtering.

4. Ambiguity Function.

The ambiguity function is:

$$Af(\tau, \omega) = \int_{-\infty}^{+\infty} f\left(t + \frac{\tau}{2}\right) f\left(t - \frac{\tau}{2}\right) \text{Exp}[-i\omega\tau] dt,$$

or, in the frequency domain:

$$Af(\tau, \omega) = \frac{1}{2\pi} \int_{-\infty}^{+\infty} \hat{f}\left(\nu + \frac{\omega}{2}\right) \hat{f}\left(\nu - \frac{\omega}{2}\right) \text{Exp}[i\tau\nu] d\nu,$$

and measures the spread of the signal f in time and of \hat{f} in frequency, i.e., the energy concentration. Figs. 4.1A-C represents the energy spread of the radar return example shown in Fig. 3.1A.

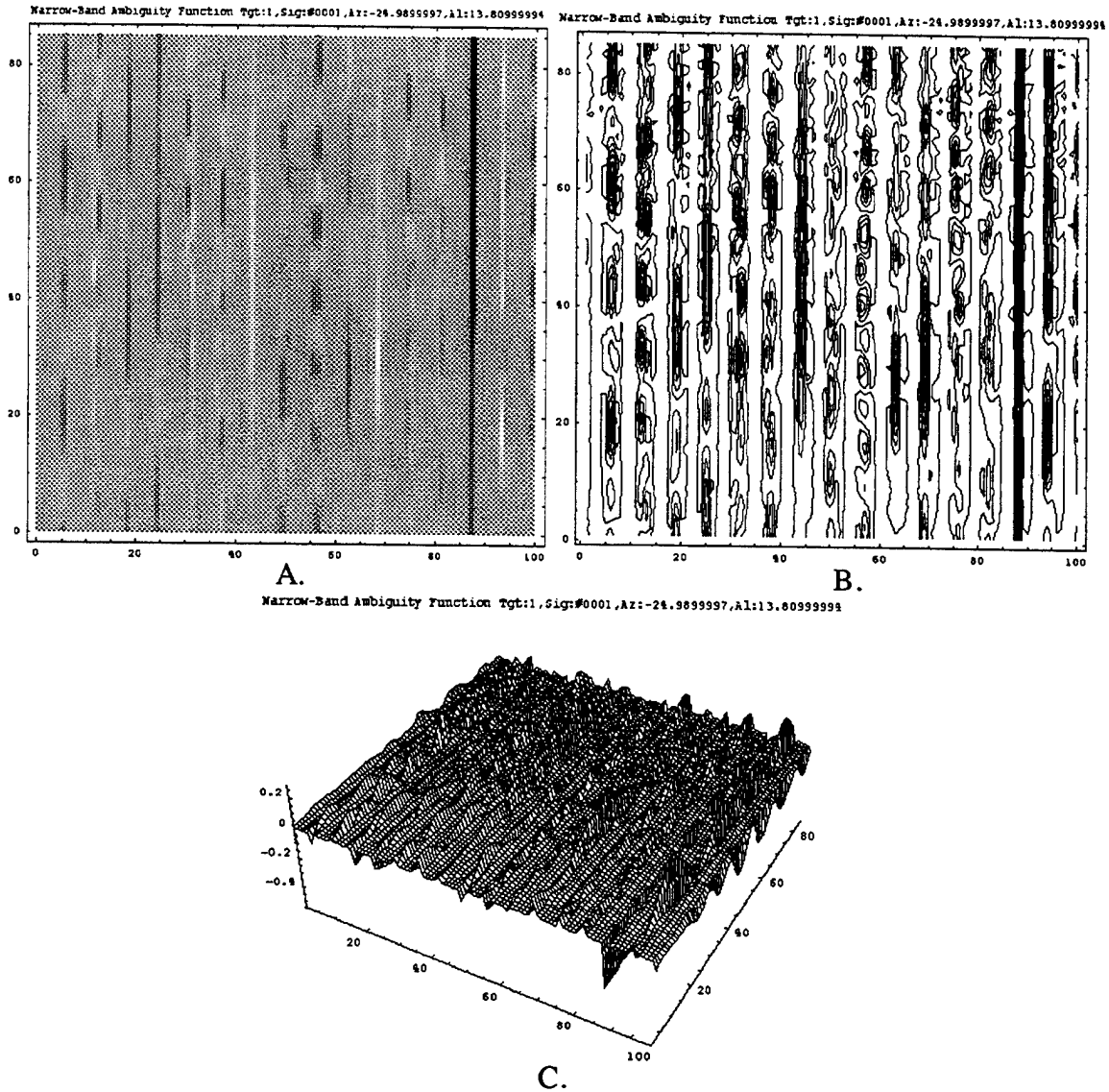


Fig. 4.1A, B & C. First example: ambiguity function.

5.0 Wigner-Ville Distribution.

The Wigner -Ville distribution is a quadratic form:

$$P_v f(t, \omega) = \int_{-\infty}^{+\infty} f\left(t + \frac{\tau}{2}\right) f^*\left(t - \frac{\tau}{2}\right) \text{Exp}[-i\omega\tau] d\tau$$

or

$$P_v f(t, \omega) = \int_{-\infty}^{+\infty} \hat{f}\left(\omega + \frac{\nu}{2}\right) \hat{f}^*\left(\omega - \frac{\nu}{2}\right) \text{Exp}[-i\nu t] d\nu$$

and defines a time-varying power spectrum for non-stationary processes. Simply stated, the Wigner-Ville transform is the cross-correlation of a signal with itself after a time and frequency shift.

The two characteristics which make the Wigner-Ville distribution nonoptimal for signal analysis purposes are that it can take on negative values and that the presence of interference terms. Fig. 5.1A. is an example of two Gabor signals. Figs. 5.1B-D show the Wigner-Ville transforms of those signals. The interference terms are clearly seen.

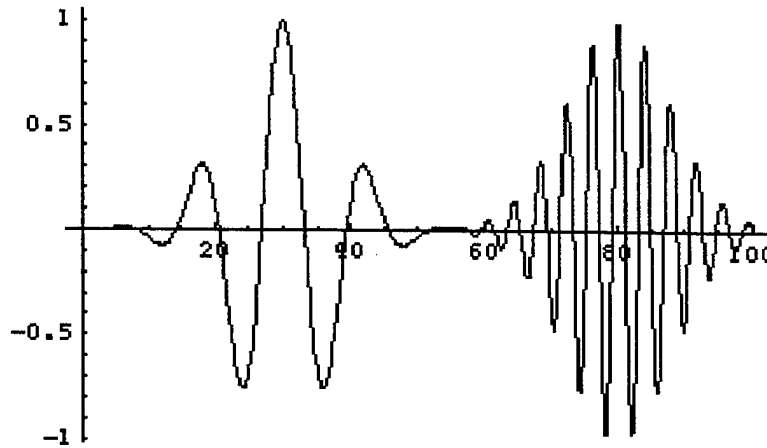


Fig. 5.1A. Two Gabor packets.

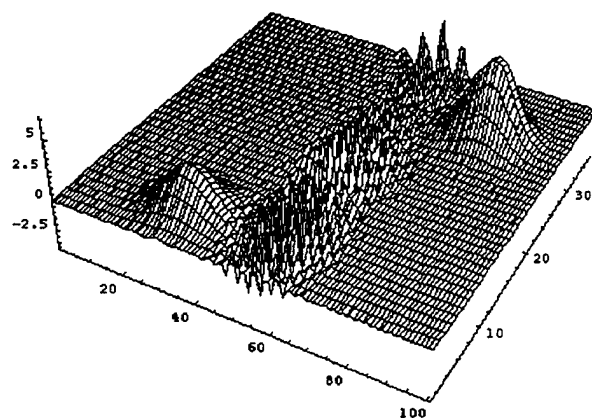
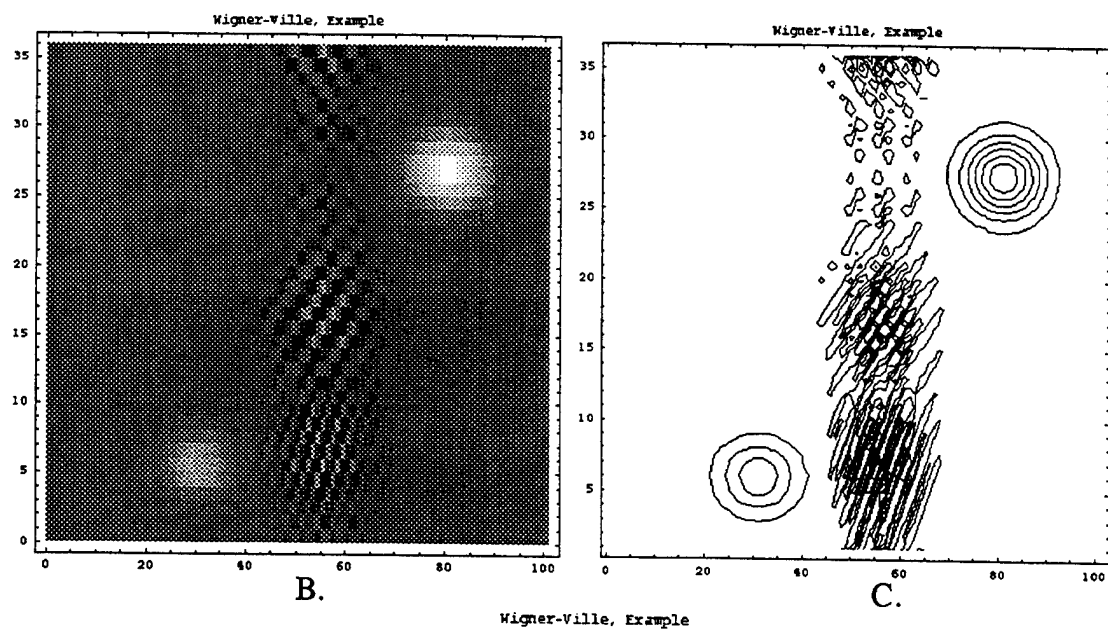
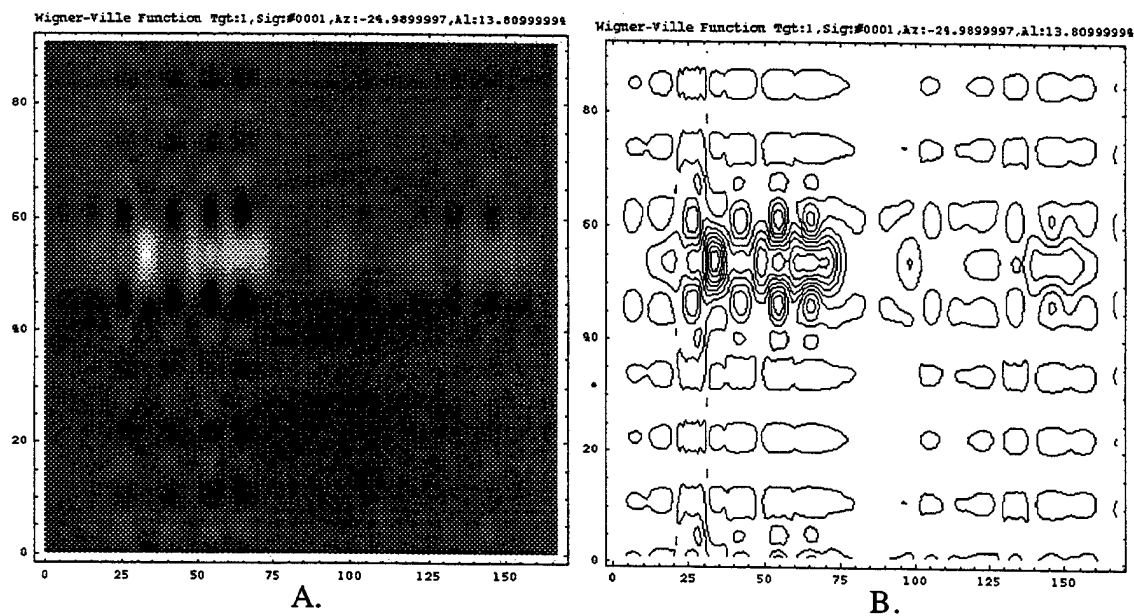


Fig. 5.1B, C & D. Wigner-Ville transform of 2 Gabor packets.

Fig. 5.2A-D are the Wigner-Ville transforms of the radar return example shown in Fig. 3.1A.



Wigner-Ville Function Tgt:1, Sig:#0001, Az:-24.9899997, Al:13.80999994

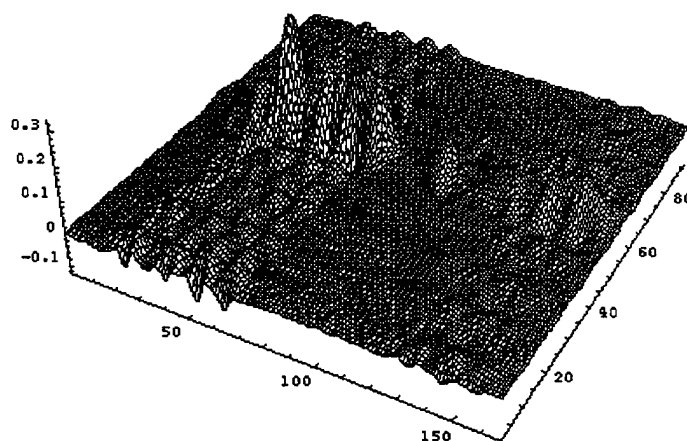


Fig. 5.2A, B & C. Wigner-Ville Transform of 1st Example.

6.0 Wavelets compared with spectrogram

6.0.1 Prologue.

The radar signal shown in the following Fig. 6.1 is wavelet transformed in the examples to follow. The frequency chirp shown in Fig. 6.2 is used as an example in the spectrogram analysis.

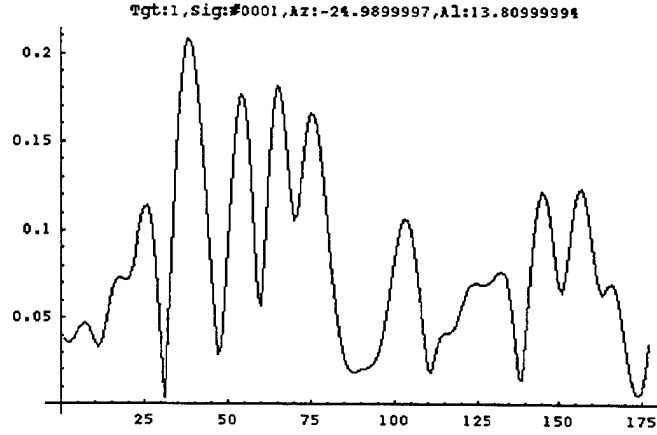


Fig. 6.1. Radar signal example.

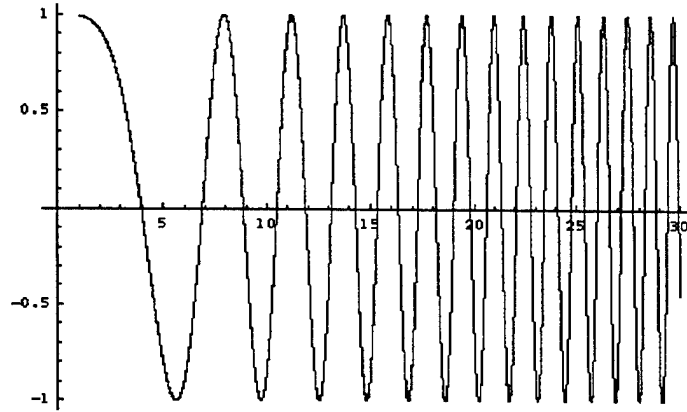


Fig. 6.2. Linear chirp $f(t) = \text{Exp}[iat^2]$.

The wavelet integral is defined:

$$Wf(u,s) = \int_{-\infty}^{+\infty} f(t) \frac{1}{\sqrt{s}} \psi * \left(\frac{t-u}{s} \right) dt.$$

Calderon and, independently, Grossman and Morlet proved that if $\psi \in L^2(\mathfrak{R})$ is a real function (that is, $L^2(\mathfrak{R})$ represent finite energy functions such that: $\int |f(t)|^2 dt < +\infty$) and this real function is such that:

$$C_{\psi} = \int_0^{+\infty} \frac{|\hat{\psi}(\omega)|^2}{\omega} d\omega < +\infty, \quad \text{Eq. 6.1.}$$

then

$$\int_{-\infty}^{+\infty} |f(t)|^2 dt = \frac{1}{C_{\psi}} \int_0^{+\infty} \int_{-\infty}^{+\infty} |Wf(u,s)|^2 du \frac{ds}{s^2}.$$

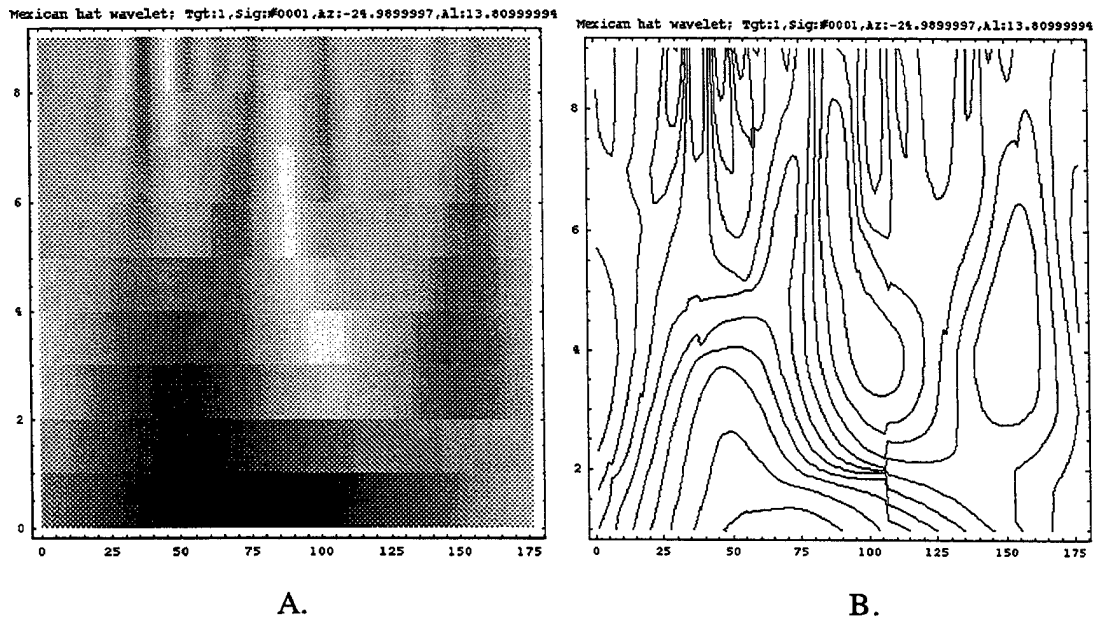
This proof demonstrates the possibility of wavelet decomposition of signals and is predicated on the conditions described by Eq. 6.1, which is called the admissibility condition. For the integral described by the admissibility condition to be finite, the wavelets must have an average of zero.

6.1 Mexican hat wavelet.

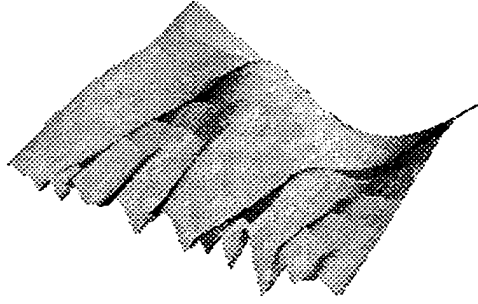
The wavelets equal to the second derivative of the Gaussian are Mexican hat wavelets. The normalized Mexican hat is:

$$\psi(t) = \frac{2}{\pi^{1/4} \sqrt{3}\sigma} \left(\frac{t^2}{\sigma^2} - 1 \right) \text{Exp} \left(-\frac{t^2}{2\sigma^2} \right).$$

Fig. 6. 3 shows an analysis of the radar return signal example (Fig. 6.1). It can be seen that use of this wavelet picks out the relevant features of the signal.



Mexican hat wavelet: Tgt:1, Sig:0001, Az:-24.9899997, Al:13.80999998



C.

Fig. 6.3. Analysis of Radar example with Mexican hat wavelet.

6.2 Local Regularity of signals and Gaussian differential wavelets.

Local signal regularity is characterized by the decay of the wavelet transform across scales. The local regularity of a signal, $f(t)$, is characterized by the Lipschitz exponents at a point. Lipschitz regularity for a function, $f(t)$, is defined: A function f is pointwise Lipschitz $\alpha \geq 0$ at v if there exists $K > 0$, and a polynomial p_v of degree $m = \lfloor \alpha \rfloor$ such that

$$\forall t \in \mathbb{R}, |f(t) - p_v(t)| \leq K|t - v|^\alpha. \quad \text{Eq. 6.2.}$$

A wavelet transform estimates the exponent α if that wavelet has $n > \alpha$ vanishing moments:

$$\int_{-\infty}^{+\infty} t^k \psi(t) dt = 0 \quad \text{for } 0 \leq k \leq n.$$

A wavelet with n vanishing moments is orthogonal to polynomials of degree $n - 1$. Since $\alpha < n$, the polynomial p_v has degree at most $n - 1$. Therefore:

$$Wp_v(u, s) = \int_{-\infty}^{+\infty} p_v(t) \frac{1}{\sqrt{s}} \psi\left(\frac{t-u}{s}\right) dt = 0$$

and since $f = p_v + \varepsilon_v$,

$$Wf(u, s) = W\varepsilon_v(u, s).$$

It also follows that a wavelet with n vanishing moments can be written as the n^{th} order derivative of a function θ . Fig. 6.4 below shows a wavelet transform of the radar signal of Fig. 6.1 calculated with $\psi = -\theta$, where θ is a Gaussian. The resulting $Wf(u, s)$ is the derivative of f averaged in the neighborhood of u with a Gaussian kernel dilated by s .

It is instructive to continue the analysis beyond the first derivative, due to the following theorem: Let $\psi = (-1)^n \theta^{(n)}$ with $\theta(t) = \lambda \text{Exp}\left[-\frac{t^2}{2\beta^2}\right]$. If $f = f_0 * g_\sigma$ and f_0 is uniformly Lipschitz α on $[v-h, v+h]$, then there exists A such that:

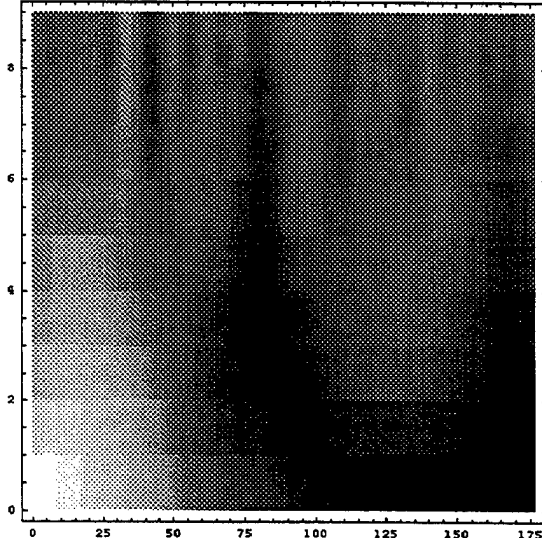
$$\forall (u,s) \in [v-h, v+h] \times \mathbb{R}^+, \quad |Wf(u,s)| \leq A s^{\alpha+1/2} \left(1 + \frac{\sigma^2}{\beta^2 s^2}\right)^{-\frac{n-\alpha}{2}},$$

where g_σ is a Gaussian variance of σ^2 :

$$g_\sigma(t) = \frac{1}{\sqrt{2\pi}\sigma} \text{Exp}\left[-\frac{t^2}{2\sigma^2}\right].$$

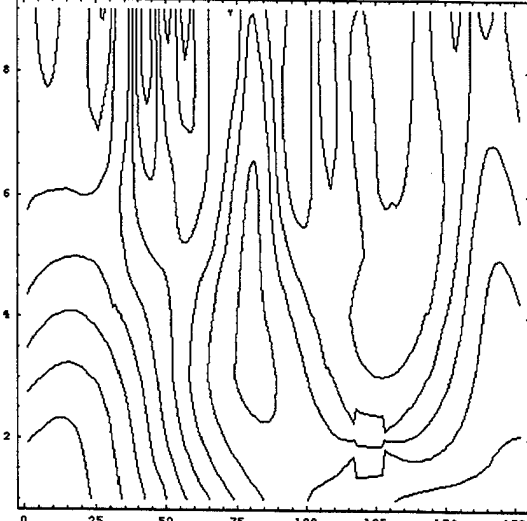
Fig. 6.5 below shows a wavelet transform of the radar signal of Fig. 6.1 calculated with $\psi = -\theta''$, where θ is a Gaussian. Essentially, the above theorem describes how the wavelet transform decay relates to the amount of diffusion of a singularity. The difference between the analyses offered by Fig. 6.4 and 6.5 reflects the differences in the smoothness of the decay of transitions in the signal. These differences reflect variations in the signal which can be infinitely continuously differentiable.

Gaussian Differential; Tgt:1, Sig:#0001, Az:-24.9899997, Al:13.80999994



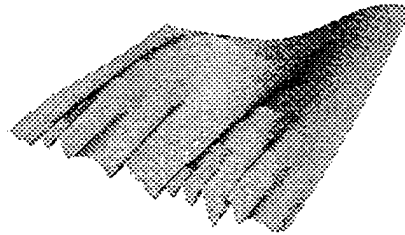
A.

Gaussian Differential; Tgt:1, Sig:#0001, Az:-24.9899997, Al:13.80999994



B.

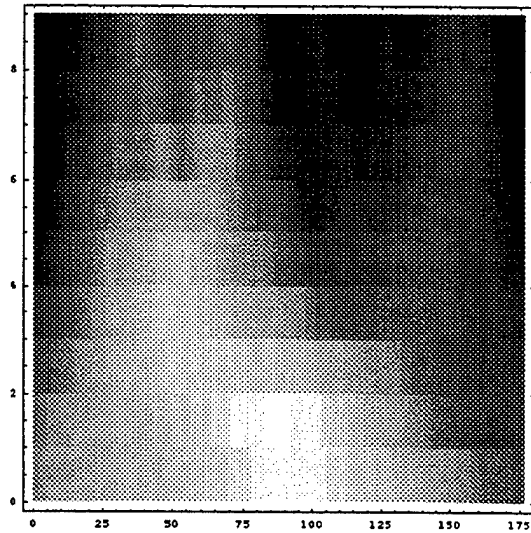
Gaussian Differential: Tgt:1, Sig:0001, Azi:24.9899997, Al:13.80999994



C.

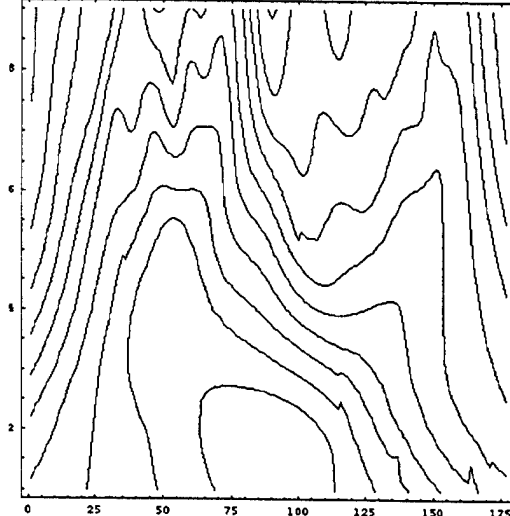
Fig. 6.4. Analysis of Radar example with Gaussian differential wavelet $\psi = -\theta$.

Gaussian 2nd Differential: Tgt:1, Sig:0001, Azi:24.9899997, Al:13.80999994



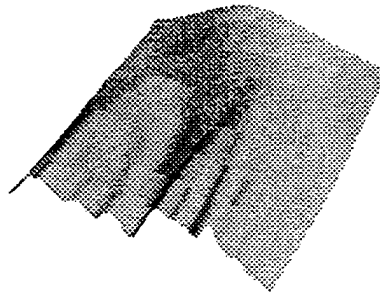
A.

Gaussian 2nd Differential: Tgt:1, Sig:0001, Azi:24.9899997, Al:13.80999994



B.

Gaussian 2nd Differential: Tgt:1, Sig:0001, Azi:24.9899997, Al:13.80999994



C.

Fig. 6.5. Analysis of Radar example with Gaussian 2nd differential wavelet $\psi = -\theta''$.

6.3 Spectrogram

The windowed Fourier transform requires a real and symmetric window $g(t) = g(-t)$, which is translated by u and modulated at the frequency ξ :

$$g_{u,\xi}(t) = \text{Exp}[i\xi t]g(t-u).$$

It can be normalized $\|g\| = 1$, so that $\|g_{u,\xi}\| = 1$ for any $(u, \xi) \in \mathfrak{R}^2$. The resulting windowed Fourier transform $f \in L^2(\mathfrak{R})$ is:

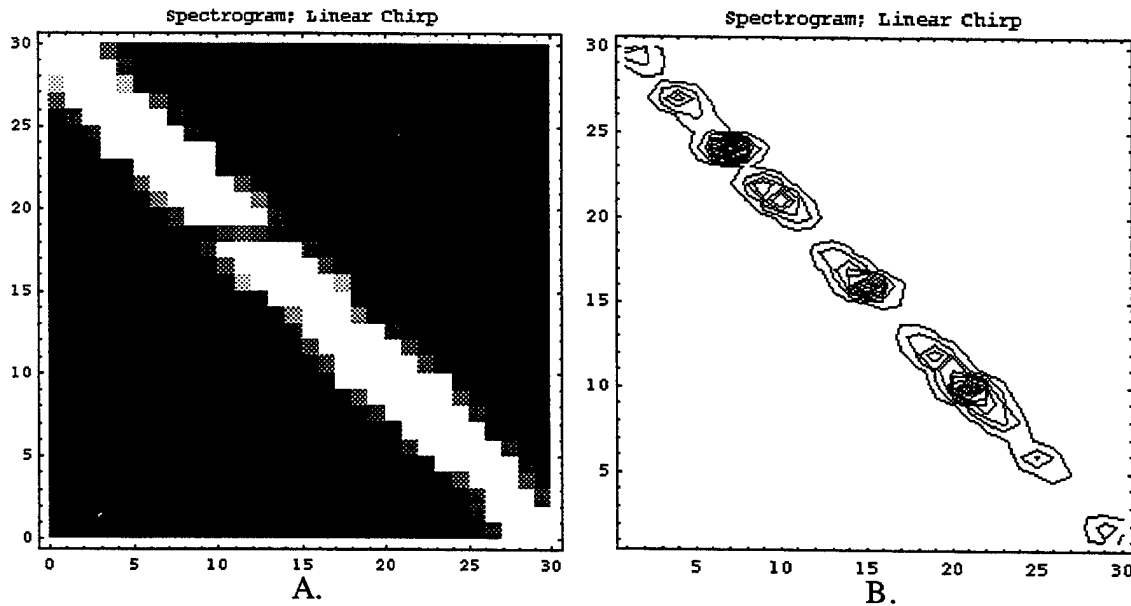
$$Sf(u, \xi) = \langle f, g_{u,\xi} \rangle = \int_{-\infty}^{+\infty} f(t)g(t-u)\text{Exp}[-i\xi t]dt,$$

also known as the *short time Fourier Transform*.

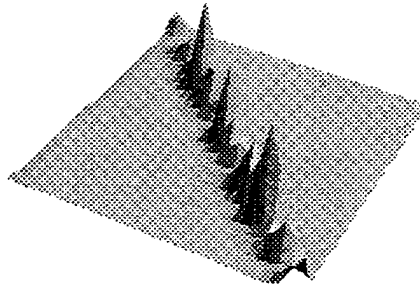
An energy density, called a *spectrogram*, P_s , can be defined:

$$P_s f(u, \xi) = |Sf(u, \xi)|^2 = \left| \int_{-\infty}^{+\infty} f(t)g(t-u)\text{Exp}[-i\xi t]dt \right|^2$$

Fig. 6.6 is the spectrogram of the linear chirp shown in Fig 6.2. Fig. 6.7 is the spectrogram of the radar signal example of Fig. 6.1. It may be seen that the spectrogram can pick out well the onset and offset of the various modulations in the signal. However, due to the fact that the window is constant (even although the modulated frequency of the kernel is changing), the spectrogram provides a biased representation of the signal as the sampling window excludes the influence of signal components outside the unchanging windowed "box". The spectrogram is thus not an optimum representation of signals and future work will demonstrate how to amend these methods to obtain wavelet representations from a similar commencement.

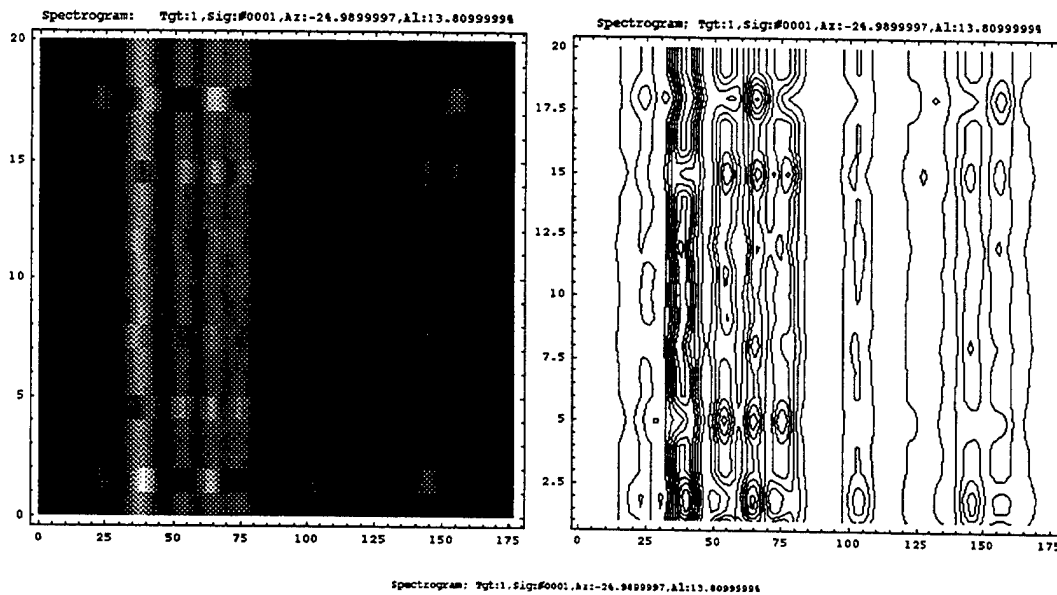


Spectrogram: Linear Chirp



C.

Fig. 6.6. Spectrogram or energy density of a linear chirp.



Spectrogram: Tgt:1, Sig:#0001, Az:-24.9899997, Al:13.80999998

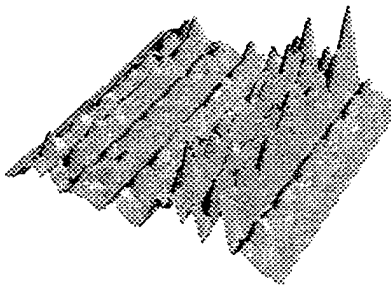


Fig. 6.7. Spectrogram or energy density of radar signal example.

7.0 Zak Transform.

The action of the Zak Transform was investigated using a radar return signal exemplar with variance of the Zak summing variable k . It was shown that discrimination capability of fine structure is lost as the range of k increases. In order to investigate improvements in discrimination capability, the Zak transform was performed not on the

radar exemplar but on the radar exemplar after Gabor analysis with kernels of various sizes. It was shown that there are distinctive patterns for each of the kernels used. Therefore a radar return signal can be analyzed into a 4-dimensional pattern signature when the results of the analysis patterns of multiple kernels are summed. This method holds promise for increasing fine discrimination capability.

7.1 Zak Transform Analysis

The Zak transform¹ of a function $f \in L^2(\mathfrak{R})$ is:

$$Zf(t, \omega) = F(t, \omega) = \sum_{k \in \mathbb{Z}} f(t+k) \text{Exp}[2\pi i k \omega], \quad (t, \omega) \in \mathfrak{R} \times \hat{\mathfrak{R}}$$

and satisfies the quasiperiodicity relations:

$$Zf(t+1, \omega) = \text{Exp}[-2\pi i \omega] Zf(t, \omega) \quad \text{and} \quad Zf(t, \omega+1) = Zf(t, \omega).$$

Therefore the values of the Zak transform are represented on the cube:

$$Q = [0, 1) \times [0, 1),$$

and the transform is a unitary mapping of $L^2(\mathfrak{R})$ onto $L^2(Q)$, where:

$$L^2(Q) = \left\{ F : \|F\|_2 = \left(\iint_Q |F(t, \omega)|^2 dt d\omega \right)^{1/2} < \infty \right\}.$$

The action of the Zak transform on a Gabor system $\{g_{m,n}\}$ constructed with $a = b = 1$ is:

$$Z(g_{m,n})(t, \omega) = \text{Exp}[2\pi i m t] \text{Exp}[2\pi i n \omega] Zg(t, \omega),$$

but $Zg(t, \omega) = 1$ for $(t, \omega) \in Q$. Therefore the Zak transform maps the orthonormal basis $\{g_{m,n}\}$ for $L^2(\mathfrak{R})$ onto the orthonormal basis $\{\text{Exp}[2\pi i m t] \text{Exp}[2\pi i n \omega]\}$ for $L^2(Q)$.

7.2 Relation of Zak Transform to Gabor Transform

The signal, $f(t)$, is represented in a Gabor expansion as:

¹ Daubechies, I., Grossman, A. & Meyer, Y. Painless nonorthogonal expansions. *J. Math. Phys.*, 27, 1271-1283, 1986;

Daubechies, I., The wavelet transform, time-frequency localization and signal analysis. *IEEE Trans. Info. Theory*, 36, 961-1005, 1990;

Heil, C. & Walnut, D., Continuous and discrete wavelet transforms. *SIAM Review*, 31, 628-666, 1989;

Janssen, A.J.E.M., Bargmann transform, Zak transform, and coherent states. *J. Math. Phys.*, 23, 720-731, 1982;

Janssen, A.J.E.M., The Zak transform: A signal transform for sampled time-continuous signals. *Philips J. Res.*, 43, 23-69, 1988;

Zak, J., Lattice operators in crystals for Bravais and reciprocal vectors. *Phys. Rev. B*, 12, 3023-3026, 1975.

$$f(t) = \sum_m \sum_k a_{mk} g(t - mT) \text{Exp}[i2\pi kUt],$$

where the variable m is used in connection with a time shift, the variable k in connection with a frequency shift, and $g(t)$ is the envelope of the elementary signal - and conceived in this case as the *synthesis window*². Thus the Gabor expansion is the representation of a signal as the superposition of elementary packet signals, and the Gabor coefficients a_{mk} represent the complex amplitude of a packet at time position mT and frequency kU .

With an *analysis window*, $\gamma(t)$, corresponding to the synthesis window, $g(t)$, the Gabor coefficients, a_{mk} , are determined by means of the Gabor transform:

$$a_{mk} = \int f(t) \gamma^*(t - mT) \text{Exp}[-i2\pi kUt] dt.$$

Alternatively, the Gabor transform can be considered as a sampled version of the windowed Fourier transform $W_f(t, u)$ of the signal $f(t)$:

$$W_f(t, u) = \int f(t') \gamma^*(t' - t) \text{Exp}[-i2\pi ut'] dt',$$

on the rectangular lattice ($t = mT$, $u = kU$): $a_{mk} = W_f(mT, kU)$.

There are three sampling cases of note:

(1) *Critical Sampling* - $UT = 1$ - for which there exists a unique relationship between the synthesis window, $g(t)$, and the analysis window, $\gamma(t)$, and a synthesis window can be uniquely determined from a given analysis window. In the case of critical sampling, the Gabor signal expansion is related to the degrees of freedom of the signal. If a signal $f(t)$ is limited to the time interval $|t| < 0.5a$ and its Fourier transform to the frequency interval $|u| < 0.5b$, the number of degrees of freedom equals the number of Gabor coefficients in the time-frequency area ab , which is equal to the time-bandwidth product ab . In the case of critical sampling, the representation is not always stable. This instability is expressed formally by the Balian Low Theorem³. The stability problem can be overcome with multiwindows. A Gabor system is not only a *frame* (see below), but is also an *exact frame* (see below) if $UT = 1$.

(2) *Oversampling* - $UT < 1$ - for which such a unique relationship does not exist and there is no unique relationship between the synthesis window and the analysis window. A Gabor system is a frame, but not an exact frame when $UT < 1$.

(3) *Undersampling* - $UT > 1$ - for which the sequence of representation functions is incomplete and therefore does not constitute a frame³. A Gabor system is incomplete and not a frame when $UT > 1$.

The Fourier transform of the expansion coefficients is:

$$\hat{a}(\xi, \eta) = (Fa)(\xi, \eta) = \sum_m \sum_k a_{mk} \text{Exp}[-i2\pi(m\eta - k\xi)],$$

² Bastiaans, M.J., Gabor's expansion of a signal into Gaussian elementary signals. *Proc. IEEE*, 68, 538-539, 1980.

³ Daubechies, I., The wavelet transform, time-frequency localization and signal analysis. *IEEE Trans. Info. Theory*, 36, 961-1005, 1990.

and it can be shown that in the case of integer oversampling, i.e., $1/U = pT$, that⁴:

$$\hat{a}(\xi, \eta) = pT \sum_k f(\xi pT + kpT) \text{Exp}[-i2\pi k(pT)(\eta pU)] \\ \times \left[\sum_m \gamma(\xi pT + [kp - m]T) \text{Exp}[-i2\pi(kp - m)T(\eta pU)] \right]^*$$

Defining the Zak transform as:

$$Z_f(t, u; \Delta) = \sum_m f(t + m\Delta) \text{Exp}[-i2\pi m\Delta u],$$

then the previous equation can be expressed using the Zak transform twice, with $t = \xi pT$, $u = \eta pU$, $\Delta = pT$ for the $f(t)$ expression and $t = \xi pT$, $u = \eta pU$, $\Delta = T$ for the $\gamma(t)$ expression. In terms of this Zak transform, the Fourier transform on the expansion coefficients is:

$$\hat{a}(\xi, \eta) = pTZ_f(\xi pT, \eta pU; pT)Z_\gamma^*(\xi pT, \eta pU; T).$$

7.3 Balian-Low Theorem

We use the following definitions:

$\|f\|_2 = \left(\int |f(t)|^2 dt \right)^{1/2}$ for the L^2 -norm of a complex-valued function f , or the energy of f , L^2 being the space of all functions with finite energy.

$\langle f, g \rangle = \int f(t)g^*(t)dt$ is an inner product on $L^2(\mathfrak{R})$.

A sequence $\{f_k\}$ of functions in $L^2(\mathfrak{R})$ is orthonormal if:

$$\langle f_k, f_l \rangle = \delta_{k,l} = \begin{cases} 1, & \text{if } k = l \\ 0, & \text{if } k \neq l \end{cases}$$

A sequence $\{f_k\}$ is a basis for $L^2(\mathfrak{R})$ if

$\forall f \in L^2(\mathfrak{R})$, \exists unique scalars $c_k(f)$ such that $f = \sum_k c_k(f)f_k$, where the basis elements are: $c_k(f) = \langle f, f_k \rangle$. For an orthonormal basis:

$$\forall f \in L^2(\mathfrak{R}), \quad f = \sum_k \langle f, f_k \rangle f_k$$

Plancherel's formula gives that the energy of f is related to the energy of the coefficients:

⁴ Bastiaans, M.J., Gabor's signal expansion in optics. pp. 427-451 in Feichinger, H.G. & Strohmer, T., (Ed.s) Gabor Analysis and Algorithms, Birkhäuser, Boston, 1998.

$$\forall f \in L^2(\mathfrak{R}), \quad \|f\|_2^2 = \sum_k |\langle f, f_k \rangle|^2$$

A sequence $\{f_k\}$ is a *frame* if there exists $A, B > 0$ (the frame bounds) so that:

$$\forall f \in L^2(\mathfrak{R}), \quad A\|f\|_2^2 \leq \sum_k |\langle f, f_k \rangle|^2 \leq B\|f\|_2^2.$$

Therefore for a frame the energy $\|f\|_2^2$ of f is equivalent or related to the coefficient energy $\sum_k |\langle f, f_k \rangle|^2$. If $A = B$, then the frame is *tight*.

For any frame $\{f_k\}$ there is a dual frame $\{\tilde{f}_k\}$ so that:

$$\forall f \in L^2(\mathfrak{R}), \quad f = \sum_k \langle f, \tilde{f}_k \rangle f_k = \sum_k \langle f, f_k \rangle \tilde{f}_k.$$

If the frame is a basis then $c_k = \langle f, \tilde{f}_k \rangle$ minimizes the energy $\sum_k |c_k|^2$.

A frame can be, but need not be, a basis. If a frame is a basis, then it is *exact*. A frame $\{f_k\}$ is exact if there is no single element f_i which is deleted. A frame is a basis, if and only if, it is exact. Therefore an exact frame satisfies both the frame bound formula, above, as well as *uniquely* representing a function f in terms of frame elements, f_k , or dual frame elements, \tilde{f}_k .

A Gabor system $\{g_{mb,na}\}$ is defined by:

$$g_{mb,na}(t) = \text{Exp}[2\pi imbt]g(t - na).$$

With these definitions, the *Balian Low Theorem (BLT)* is:

Let $\{g_{mb,na} = \text{Exp}[2\pi imbt]g(t - na)\}_{m,n \in \mathbb{Z}}$ with $a, b > 0$ and $ab = 1$ (i.e., it is an exact frame).

As this Gabor system is an exact frame for $L^2(\mathfrak{R})$, then

$$\left(\int_{-\infty}^{+\infty} |tg(t)|^2 dt \right) \left(\int_{-\infty}^{+\infty} |\gamma \hat{g}(\gamma)|^2 d\gamma \right) = +\infty$$

or

$$\|tg(t)\|_2 \|\gamma \hat{g}(\gamma)\|_2 = +\infty$$

Benedetto et al⁵ point out that the BLT maximizes the classical uncertainty principle, which is:

Let $(t_0, \gamma_0) \in \mathfrak{R} \times \hat{\mathfrak{R}}$, then

⁵ Benedetto, J.J., Heil, C. & Walnut, D.F., Gabor systems and the Balian-Low theorem. pp. 85-122 in Feichtinger, H.G. and Strohmer, T. (Ed.s) *Gabor Analysis and Algorithms: Theory and Applications*, Birkhäuser, Boston, 1998.

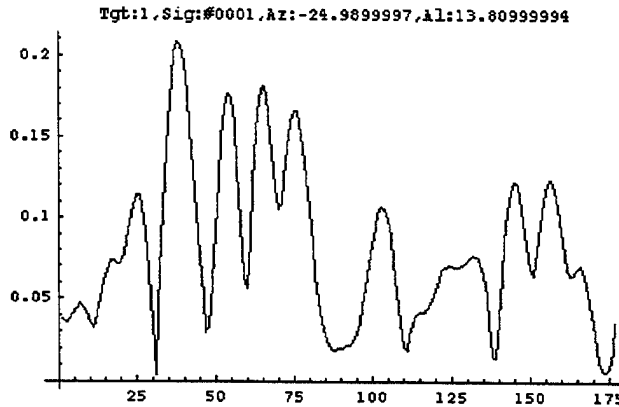
$$\forall f \in L^2(\mathcal{R}), \quad \|f\|_2^2 \leq 4\pi \|(t-t_0)f(t)\|_2 \|(\gamma-\gamma_0)\hat{f}(\gamma)\|_2$$

The crucial observation⁵ is that if a Gabor system $\{g_{mb,na}\}$ forms an exact frame, the right side of inequality is infinite when f is replaced by g . Essentially, the BLT states that an exact frame is a filter set of sampling windows with an infinite time-bandwidth product. Conversely, the uncertainty product states that there is a minimum time-bandwidth product for sampling windows. Therefore the exact frame Gabor system can be used to sample signals of any size time-bandwidth product, but there is a minimum time-bandwidth product into which any maximum time-bandwidth product can be analyzed. The condition $ab = 1$ can thus be interpreted as a Nyquist criterion.

7.4 Exemplars

The radar return signal exemplar is shown in Fig. 7.1 (top), together with Gabor analyzing functions, g_{mn} , for $n = 1, 2$ and 5. Figs 7.2, 7.3, 7.4 and 7.5 show the pattern analysis of the radar exemplar for the Zak transform variable $k = 1$ to 5, 1 to 10, 1 to 15 and 1 to 177. It can be seen that discrimination capability of fine structure is lost as the range of k increases. Thus, there is a loss of discriminated fine structure in the progression from Fig. 7.2 through to Fig. 7.5.

In order to investigate improving discrimination capability, the Zak transform was performed not on the radar exemplar but on the radar exemplar after Gabor analysis with kernels of various sizes. Figs 7.6, 7.7 and 7.8 show the results. Fig. 7.6 is the Zak transform of the radar exemplar after filtering with the smallest Gabor analyzing kernel - A of Fig. 7.1; Fig. 7.7 uses the next largest - B of Fig. 7.2; and Fig. 7.8 uses the largest - C of Fig. 7.1. It can be seen that there are distinctive patterns for each of the kernels. Therefore a radar return signal - such as the exemplar - can be analyzed into a 4-dimensional pattern signature when the results of the analysis patterns of multiple kernels are summed.



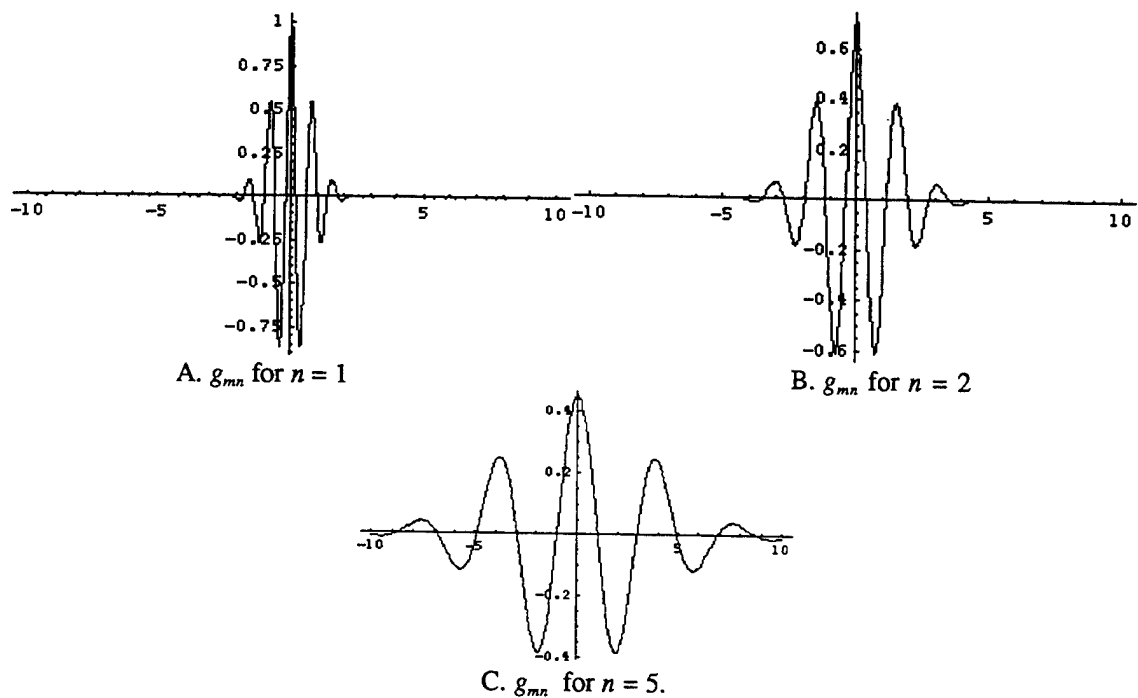
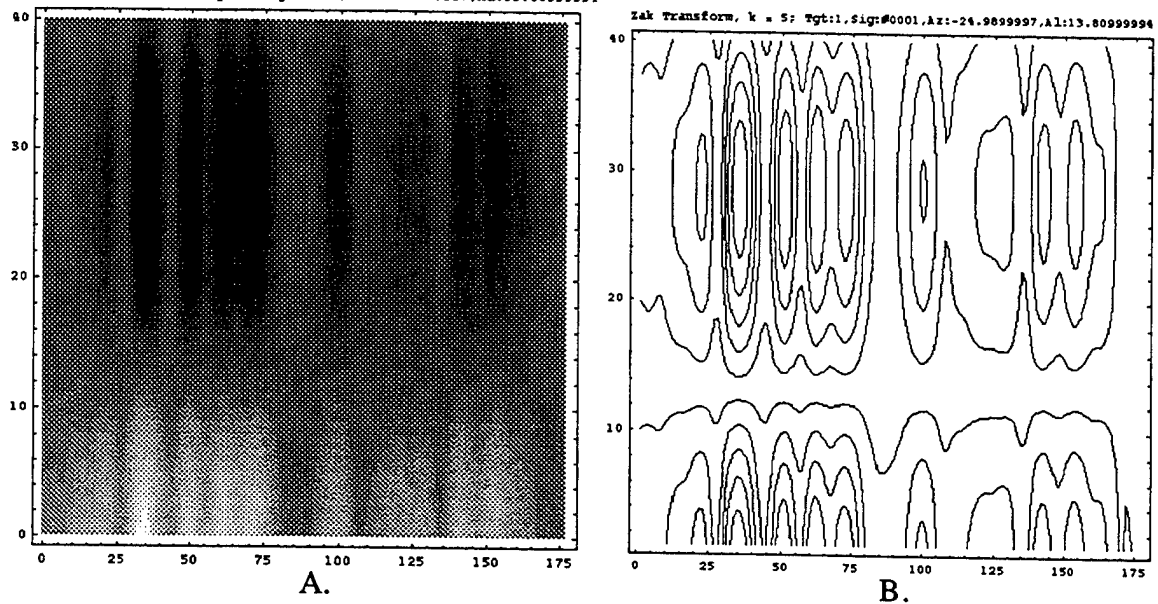
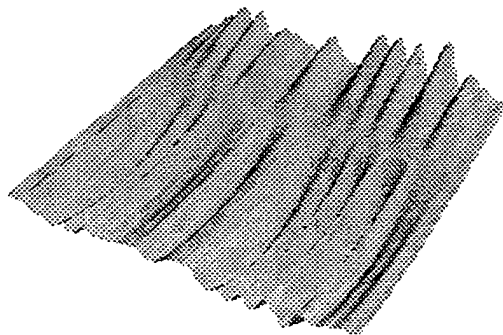


Fig. 7.1. (Top) Exemplar of a radar signal used in the analysis. (Bottom) g_{mn} for various n .

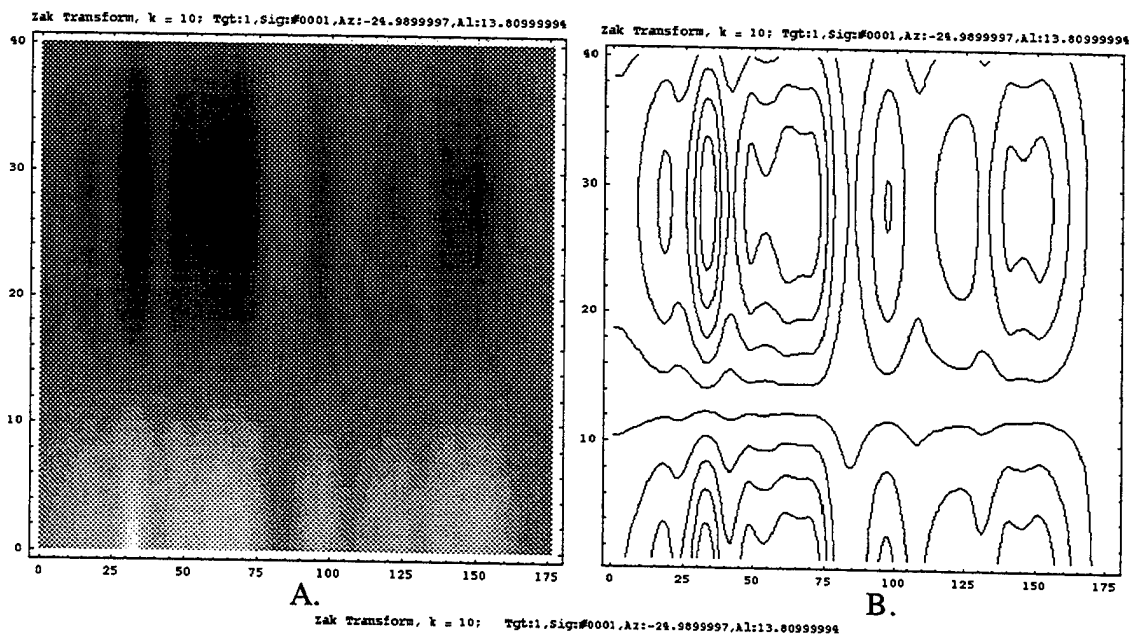


Zak Transform, $k = 5$; Tgt:1, Sig:#0001, Az:-24.9899997, Al:13.80999994



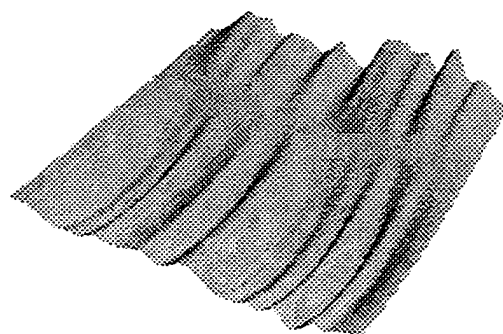
C.

Fig. 6.2. Zak transform of radar signal exemplar, for $k = 1$ to 5.



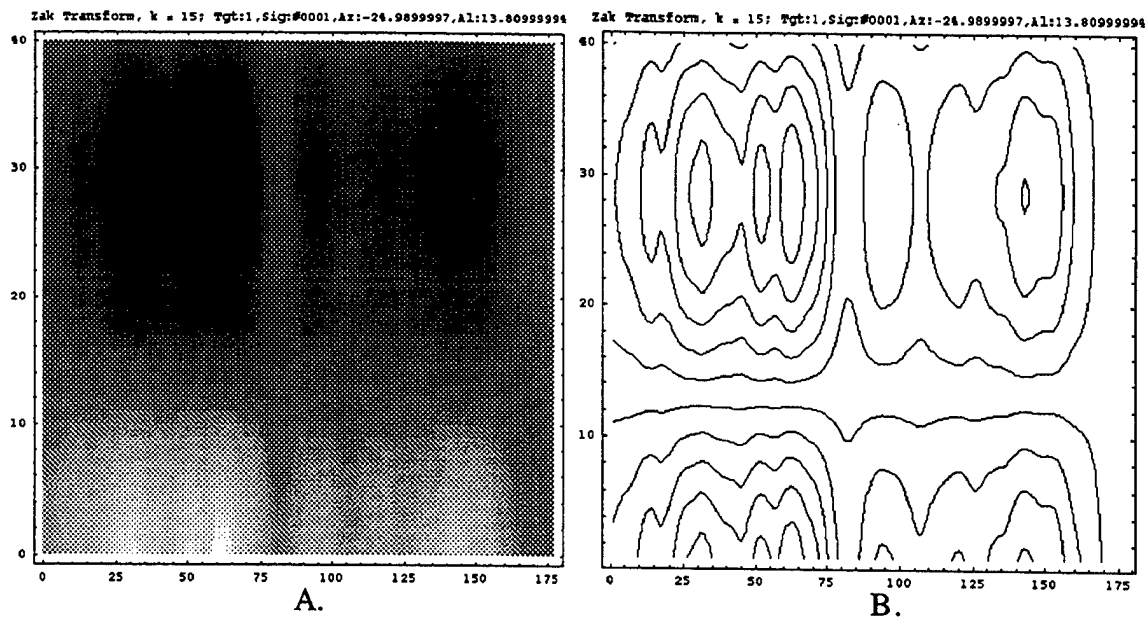
A.

B.

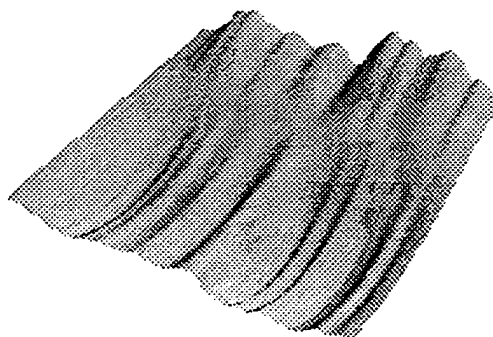


C.

Fig. 7.3. Zak Transform for $k = 1$ to 10.

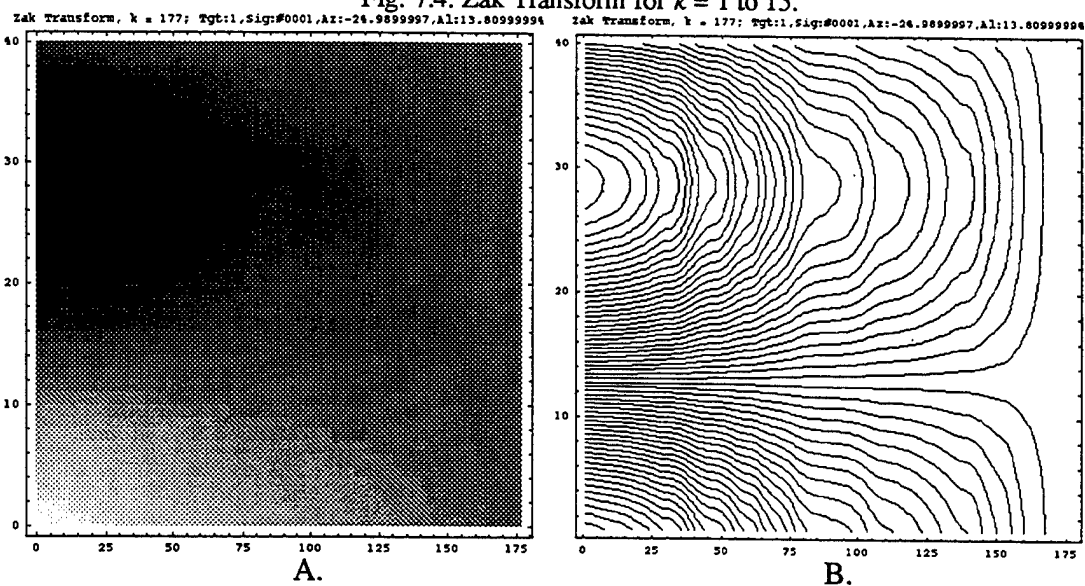


Zak Transform, $k = 15$; Tgt:1, Sig:#0001, Az:-24.9899997, Al:13.80999994

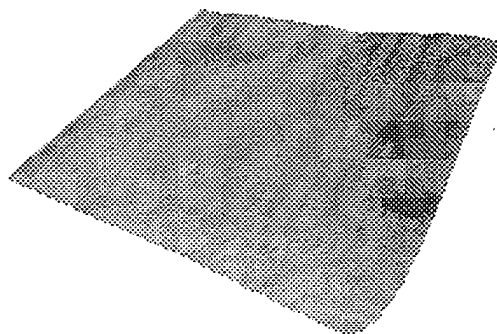


C.

Fig. 7.4. Zak Transform for $k = 1$ to 15.



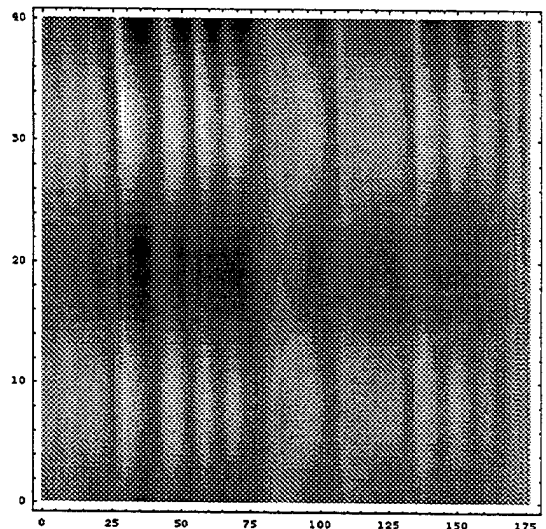
Zak Transform, $k = 177$; Tgt:1, Sig:#0001, Az:-24.9899997, Al:13.80999994



C.

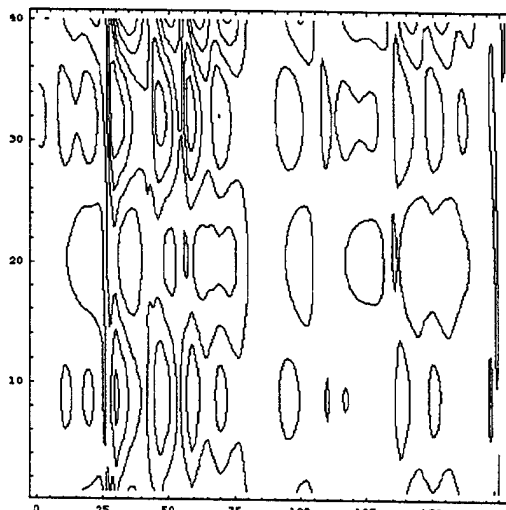
Fig. 7.5. Zak Transform for $k = 1$ to 177.

Zak Transform of $g(m,n)$, $n = 1$, $k = 5$; Tgt:1, Sig:#0001, Az:-24.9899997, Al:13.80999994



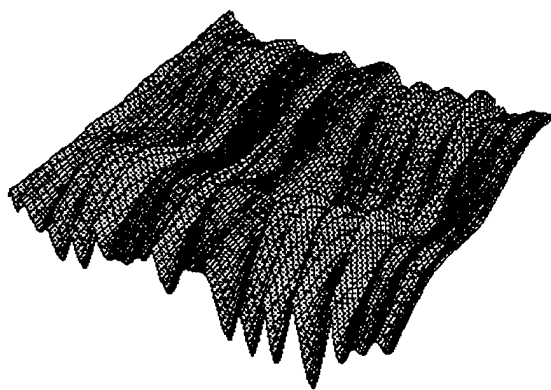
A.

Zak Transform of $g(m,n)$, $n = 1$, $k = 177$; Tgt:1, Sig:#0001, Az:-24.9899997, Al:13.80999994

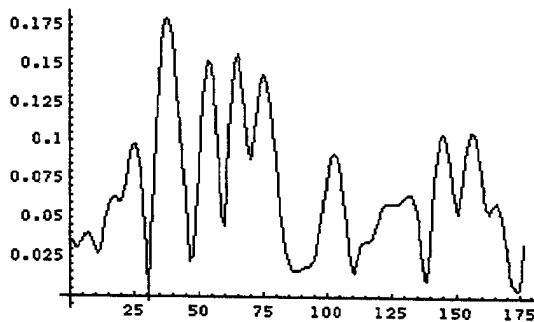


B.

Zak Transform of $g(m,n)$, $n = 1$, $k = 177$; Tgt:1, Sig:#0001, Az:-24.9899997, Al:13.80999994



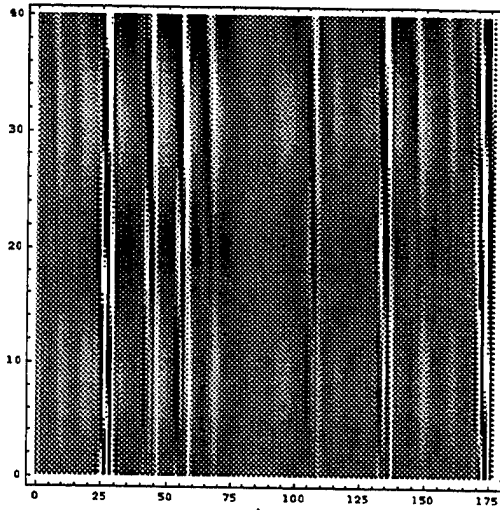
C.



D.

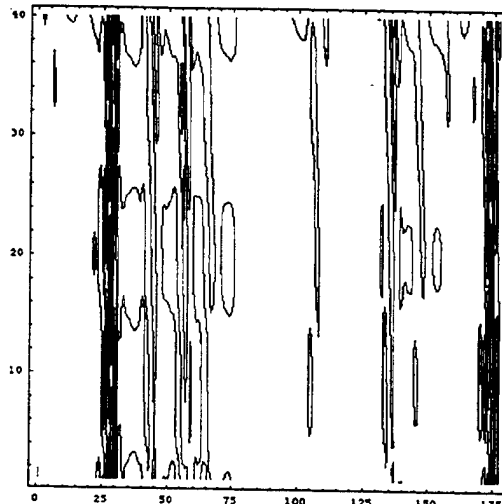
Fig. 7.6. Zak Transform of $g(m,n)$, $n = 1$ (Bottom right), $k = 177$.

Zak Transform of $g(m,n)$, $n = 2$, $k = 5$; Tgt:1, Sig:0001, Azi:-24.9899997,
Al:13.80999994



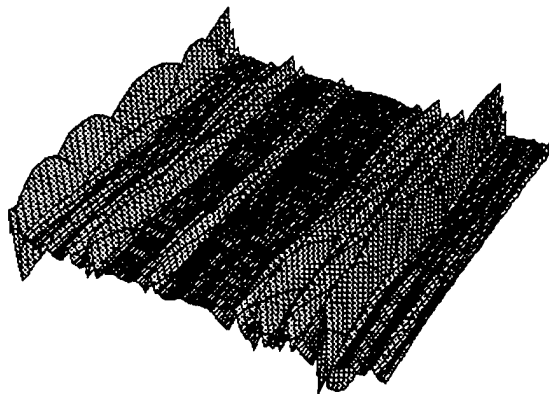
A.

Zak Transform of $g(m,n)$, $n = 2$, $k = 177$; Tgt:1, Sig:0001, Azi:-24.9899997,
Al:13.80999994

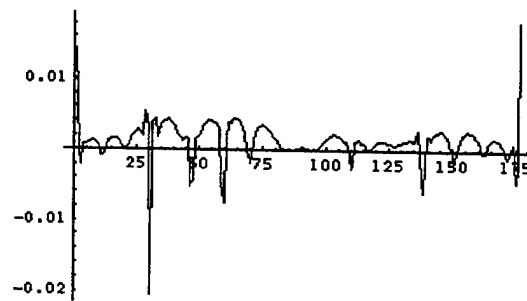


B.

Zak Transform of $g(m,n)$, $n = 2$, $k = 177$; Tgt:1, Sig:0001, Azi:-24.9899997,
Al:13.80999994



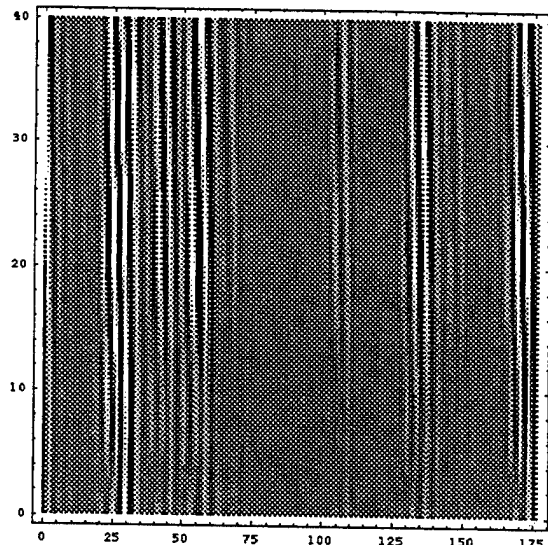
C.



D.

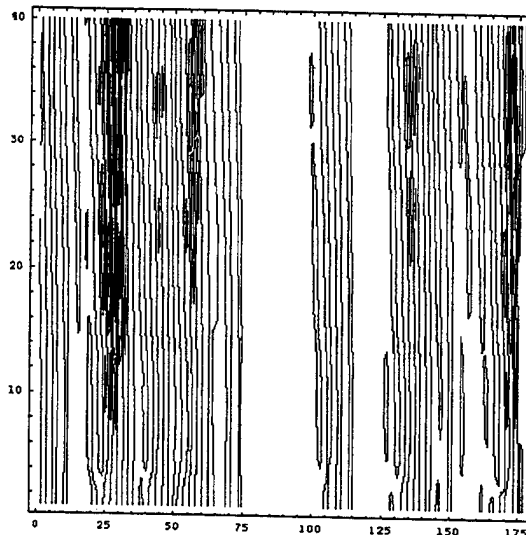
Fig. 7.7. Zak Transform of $g(m,n)$, $n = 2$ (Bottom right), $k = 5$.

Zak Transform of $g(m,n)$, $n = 5$, $k = 5$; Tgt:1, Sig:#0001, Azi:-24.9899997,
Al:13.80999994



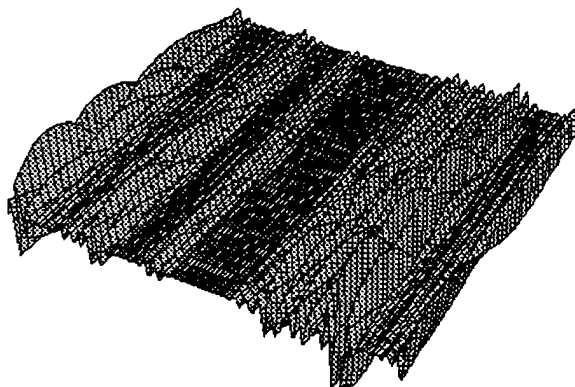
A.

Zak Transform of $g(m,n)$, $n = 5$, $k = 177$; Tgt:1, Sig:#0001, Azi:-24.9899997,
Al:13.80999994

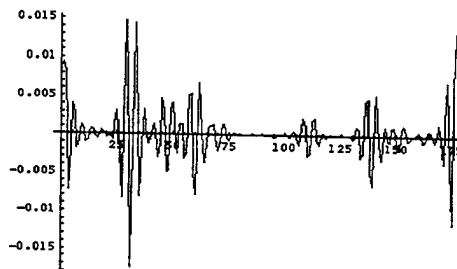


B.

Zak Transform of $g(m,n)$, $n = 5$, $k = 177$; Tgt:1, Sig:#0001, Azi:-24.9899997,
Al:13.80999994



C.



D.

Fig. 7.8. Zak Transform of $g(m,n)$, $n = 5$ (bottom right), $k = 177$.

8.0 Adaptive Methods

We addressed new methods for achieving discrimination of both frequency-dependent aspects of the target and time-dependent scattering centers. The Adaptive Gabor Representation (AGR) was used to analyze a radar signal return in two forms: the functions were either varying Q or constant Q . We found the constant Q form appears optimum. Frequency hopping signals as well as monocycle pulses were analyzed with the AGR and the *Combined* Wigner-Ville Distribution of the AGR calculated. It was shown that with all frequency components combined the frequency components of the signal can be identified, but not the pulse. However, when the *Combined* Wigner-Ville representation of the AGR is calculated using only the high frequency components of the latter, it was seen that the monocycle can be detected. Thus, these methods seems entirely appropriate for detecting the frequency-dependent and the time-dependent (transient) scattering centers of targets.

8.1 Adaptive Gabor Representation (AGR)⁶

The adaptive signal expansion is defined:

$$s(t) = \sum_p B_p h_p(t),$$

with the coefficients defined by:

$$B_p = \langle s, h_p \rangle.$$

The aim is to find $h_0(t)$ which is most similar to $s_0(t)$, i.e.,

$$|B_p|^2 = \max_{h_p} |\langle s_p(t) h_p(t) \rangle|^2. \quad \text{Step 1.}$$

Residuals are defined by:

$$s_{p+1}(t) = s_p(t) - B_p h_p(t). \quad \text{Step 2.}$$

If the functions, $h_p(t)$, have unit energy:

$$\|h_p(t)\|^2 = 1,$$

then the residual energy is:

$$s\|s_{p+1}(t)\|^2 = \|s_p(t)\|^2 - |B_p|^2.$$

⁶ Qian, S., Chen, D. & Chen, K., Signal approximation via data-adaptive normalized Gaussian functions and its applications for speech processing. *Proc. ICASSP-92*, San Francisco, CA March 23-26, 1992, pp. 141-144.

Qian, S. & Chen, D., Signal representation using adaptive normalized Gaussian functions. *Signal Processing*, 36, No 1, 1-11, March, 1994.

Mallat, S. & Zhang, Z., Matching pursuit with time-frequency dictionaries. *IEEE Trans. Signal Processing* 41, 3397-3415, 1993.

Step 1 is repeated to find $h_1(t)$ as a match to $s_1(t)$, then Step 2 is repeated and so on, as the residual signal converges to zero. It should be noted that, unlike the regular Gabor expansion, as well as wavelets, the set $\{h_p(t)\}$ will never be complete in L_2 , even if the residual converges to zero, because each set of adaptive elementary functions is unique to a particular signal.

As

$$\|s(t)\|^2 = \sum_{p=0}^{\infty} |B_p|^2$$

and as

$$\frac{1}{2\pi} \iint WVD_{h_p}(t, \omega) dt d\omega = \|h_p(t)\|^2 = 1,$$

the Adaptive Spectrogram (AS) can be defined as:

$$AS(t, \omega) = \sum_p |B_p|^2 WVD_{h_p}(t, \omega),$$

where it should be noted that the summation is over rows.

The AS not only does not contain the cross-term interference of the Wigner-Ville distribution, it also satisfies the energy relation:

$$\|s(t)\|^2 = \frac{1}{2\pi} \iint AS(t, \omega) dt d\omega.$$

The choice of $h_p(t)$ is completely arbitrary. Following convention⁷, we choose the Gabor-type functions:

$$h_p(t) = \left(\frac{\alpha_p}{\pi}\right)^{1/4} \exp\left[-\frac{\alpha_p}{2}(t-t_{0_p})^2\right] \exp[if_{0_p}t],$$

where

$$\Delta t = \sqrt{\frac{1}{2} \cdot \frac{1}{\alpha_p}}; \quad \Delta f = \sqrt{\frac{1}{2} \cdot \frac{\alpha_p}{1}},$$

so that:

$$\Delta f \cdot \Delta t = \frac{1}{2}.$$

⁷ Qian, S. & Chen, D., *Joint Time-Frequency Analysis*, Prentice-Hall, New York, 1996.

The Adaptive Gabor Representation (AGR) is then:

$$s(t) = \sum_p B_p h_p(t) = \sum_p B_p \left(\frac{\alpha_p}{\pi} \right)^{1/4} \exp \left[-\frac{\alpha_p}{2} (t - t_{o_p})^2 \right] \exp [i f_{o_p} t]$$

An important property of the AGR is that, unlike the Gabor expansion, for which the analysis and synthesis functions are not identical, the AGR has the same analysis and synthesis functions. The adaptive coefficients, B_p , are computed as follows:

$$B_p = \int s_p(t) h_p^*(t) dt = \left(\frac{\alpha_p}{\pi} \right)^{1/4} \int s_p(t) \exp \left[-\frac{\alpha_p}{2} (t - t_{o_p})^2 \right] \exp [-i f_{o_p} t] dt$$

The AS can then be defined as:

$$AS(t, \omega) = 2 \sum_p |B_p|^2 \exp \left[-\left\{ \alpha_p (t - t_{o_p})^2 + \frac{1}{\alpha_p} (\omega - \omega_{o_p})^2 \right\} \right],$$

where again it should be noted that this is the summation of the Wigner-Ville distribution over rows.

8.3 Wigner-Ville of the AGR.

The Wigner-Ville joint time-frequency density function of the adaptive Gabor functions is:

$$WVD_{h_p}(t, \omega) = 2 \exp \left[-\left\{ \alpha_p (t - t_0)^2 + \frac{(\omega - \omega_0)^2}{\alpha_p} \right\} \right].$$

Testing the above definitions, the AGR was calculated of the representative radar return signal shown in Fig. 8.1. Two protocols were tried (Figs 8.2 and 8.3). In the first (Fig. 8.2) the AGR was calculated using 5 frequencies, 5 modulating envelope widths, i.e., it is not a wavelet representation. The center frequency is set, then 5 modulating envelopes are applied in order to ascertain the maximum. In the second (Fig. 8.3) the AGR was calculated using a wavelet representation in which changing the center frequency changes the bandwidth, both temporal and frequency. Then the succeeding analysis is based on the residual. There is indication that the Gabor wavelet (Fig. 8.3) appears to be the optimum.

The frequency hopping signal (Fig. 8.4) was analyzed using the AGR. Fig. 8.5 shows that the AGR can pick out the individual signal frequency components. Figs 8.6 and 8.7 shows the full AGR with bandwidths 2 x and 6 x the Gabor wavelet bandwidth. At 6 x (Fig. 8.7) there is less precise timing identification.

Next, a frequency hopping signal with a high frequency monocycle was analyzed (Fig. 8.8). The AGR is shown in Fig. 8.9 and it can be seen that both the frequency and the pulse components can be identified. The *Combined* Wigner-Ville of the AGR of Fig 8.9 is shown in Fig. 8.10. It can be seen that the frequency components of the Fig. 8.8 signal can be identified, but not the pulse. However, when the *Combined* Wigner-Ville

representation of the AGR is calculated using only the high frequency components of the latter, it is seen that the monocycle can be detected.

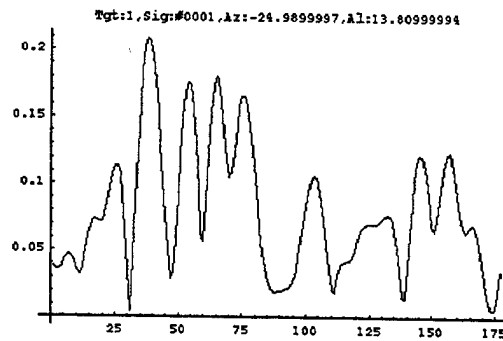


Fig. 8.1. Representative radar return signal.

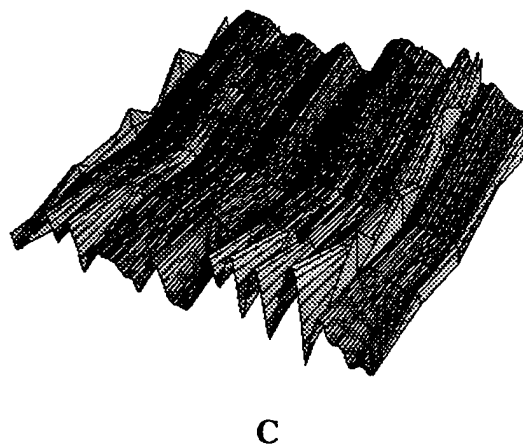
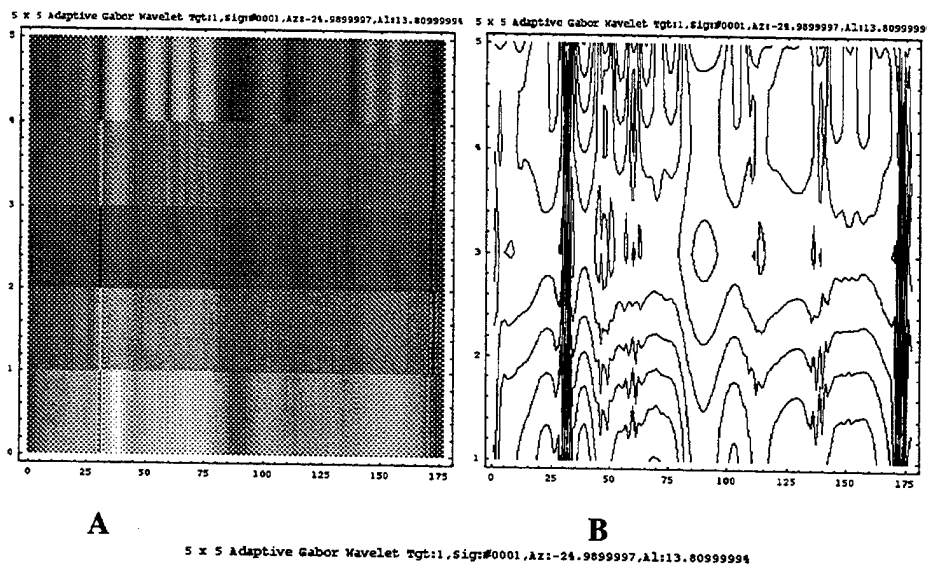
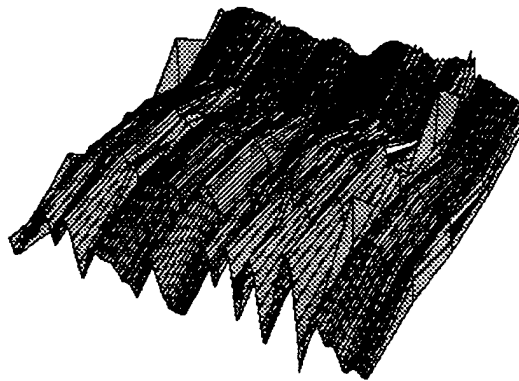
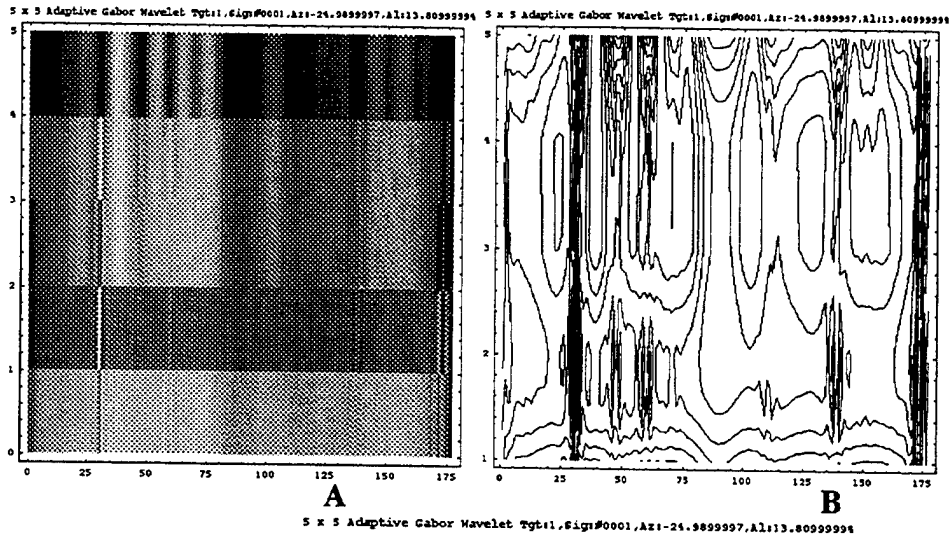


Fig. 8.2. Adaptive Gabor Representation (AGR) of the representative radar signal of Fig. 8.1. - 5 frequencies, 5 modulating envelope widths. This is not a wavelet representation. The center frequency is set, then 5 modulating envelopes are applied in order to ascertain the maximum.



C

Fig. 8.3. Adaptive Gabor Representation (AGR) of the representative radar return signal of Fig. 8.1. This is a wavelet representation in which changing the center frequency changes the bandwidth both temporal and frequency. Then the succeeding analysis is based on the residual. As there seems little difference between this method and the preceding, the Gabor wavelet appears to be the optimum.

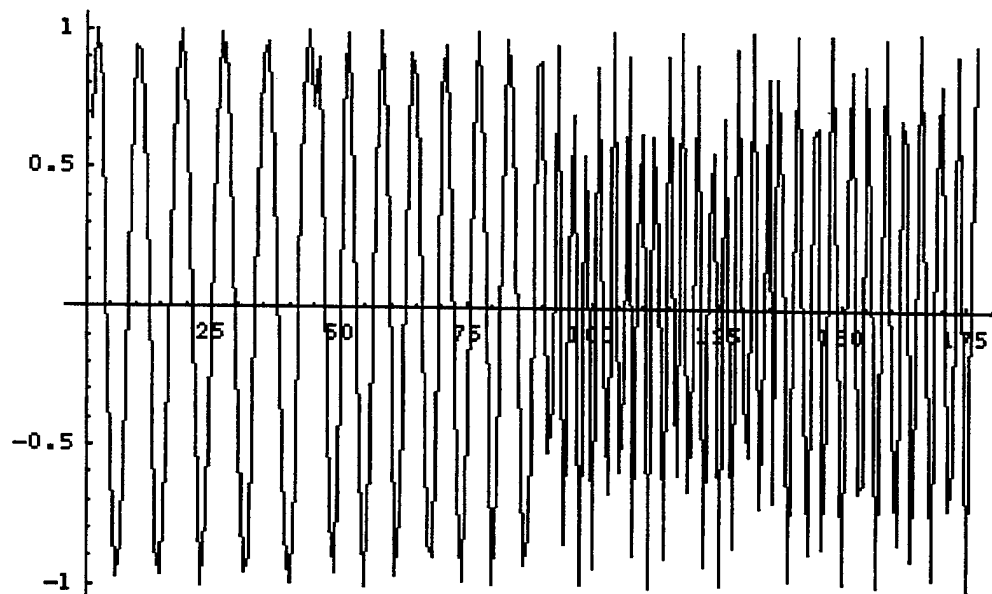


Fig. 8.4. Representative frequency hopping signal.

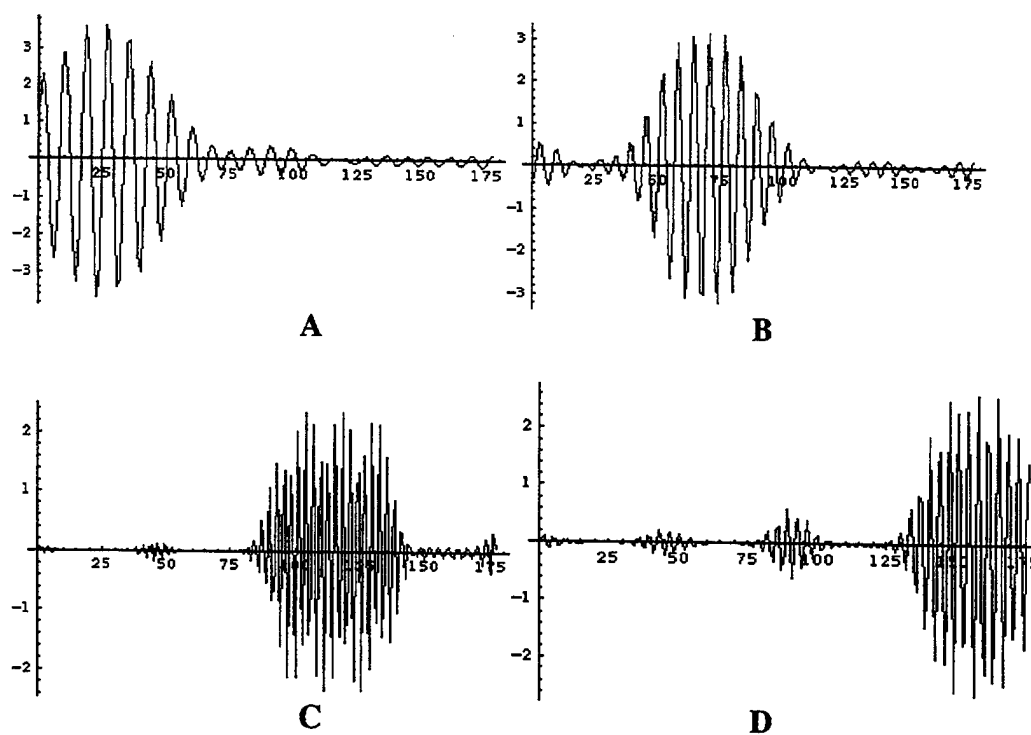


Fig. 8.5. Individual frequency components of frequency hopping signal identified with Adaptive Gabor Functions (2 x envelope).

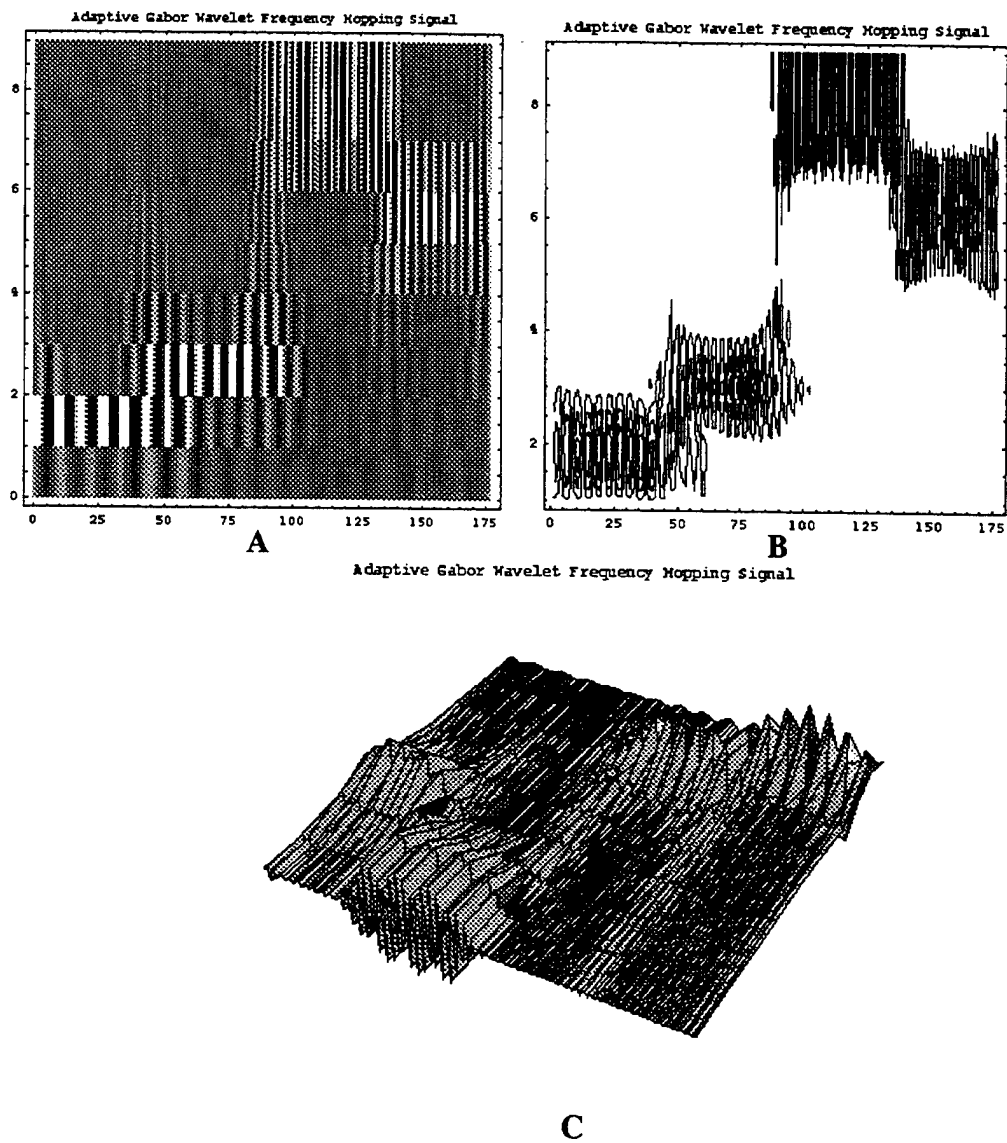


Fig. 8.6. Adaptive Gabor Representation of the frequency hopping signal with 6 x the bandwidth of the Gabor wavelet..

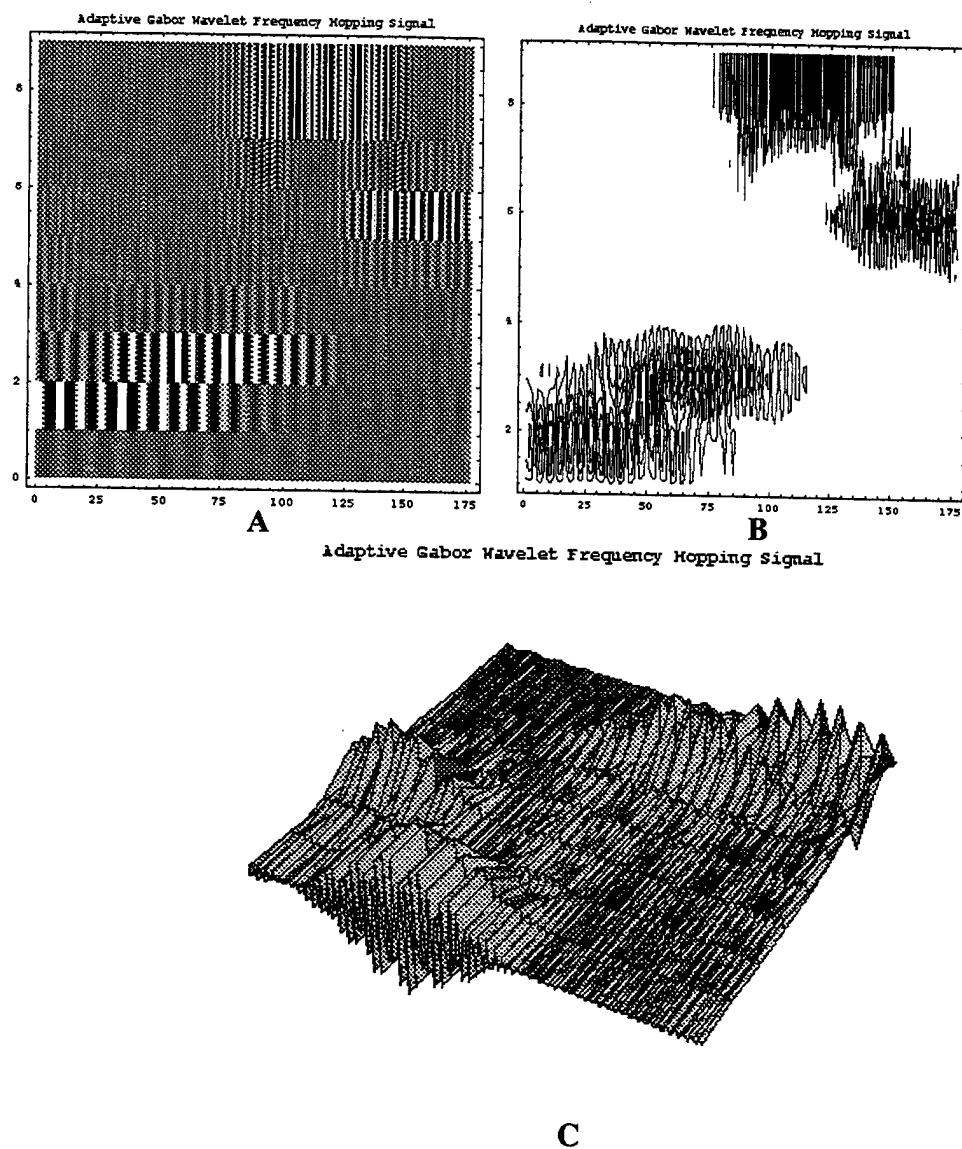


Fig. 8.7. Same as in Fig. 8.6 but with 6 x the bandwidth of the Gabor wavelet.

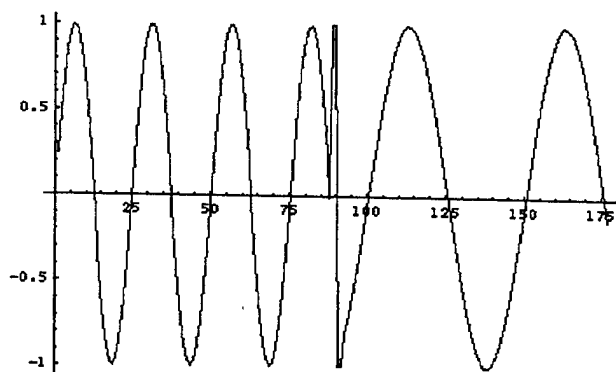


Fig. 8.8. Representative frequency hopping signal with a high frequency monocycle.

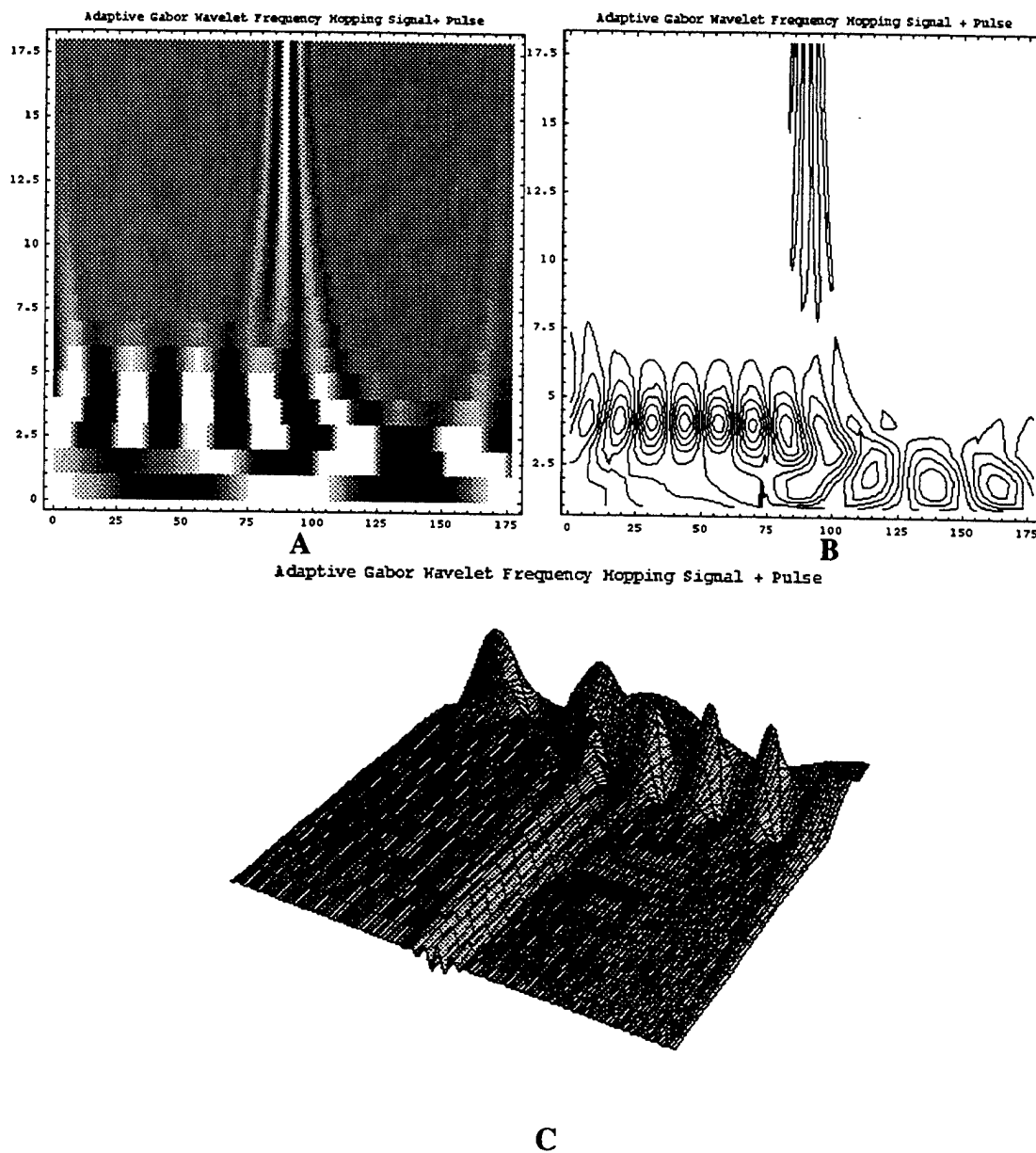


Fig. 8.9 Adaptive Gabor Representation of the frequency hopping signal with monocycle. Both the frequency and the pulse components of Fig. 8.8 can be identified.

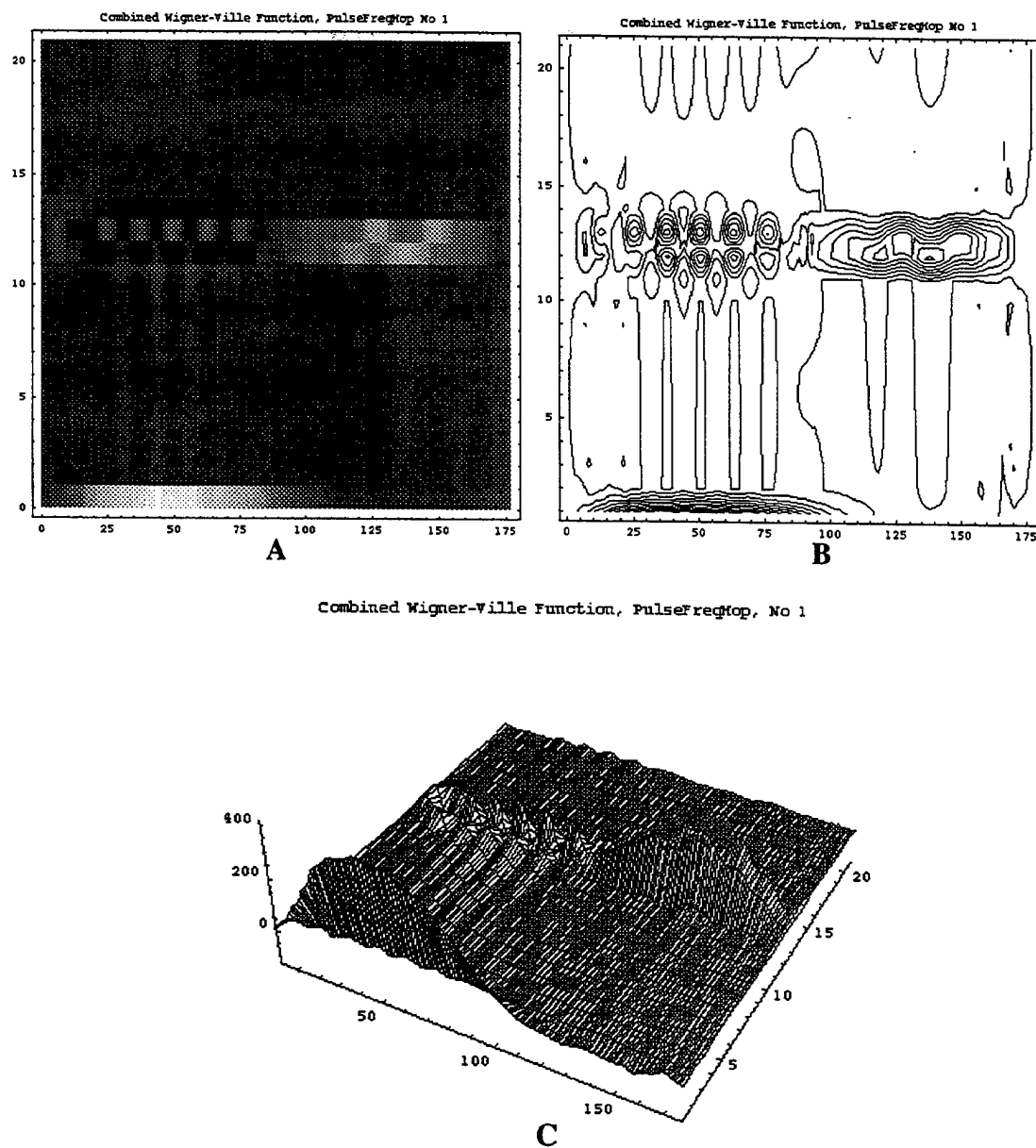
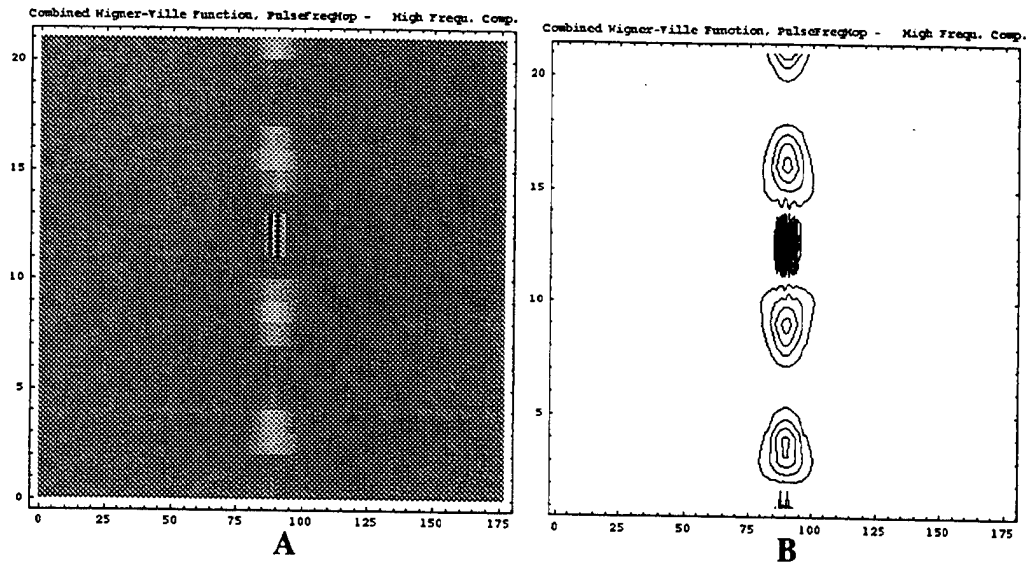


Fig. 8.10 The *combined* Wigner-Ville of the AGR of the frequency hop signal with monocycle. It can be seen that the frequency components of the Fig. 8.8 signal can be identified, but not the pulse.



Combined Wigner-Ville Function, PulseFreqTop - High Freq. Comp.

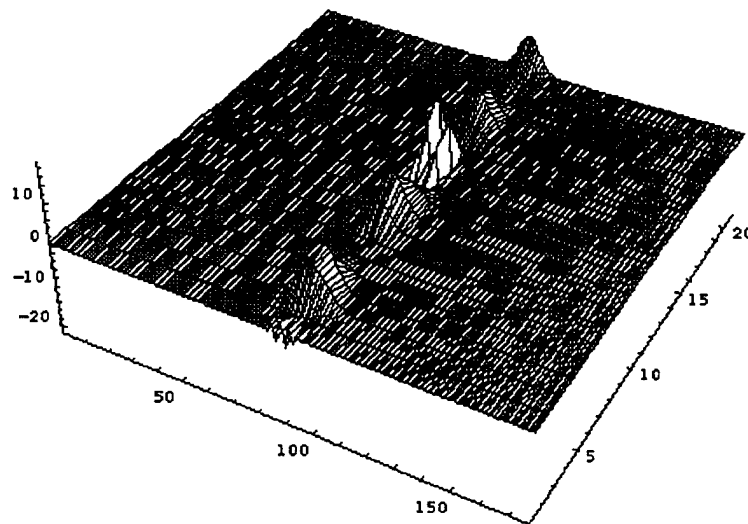


Fig. 8.11 The *Combined Wigner-Ville* representation of the Adaptive Gabor representation of the frequency hopping plus monocycle signal, using the high frequency components of the latter. It is seen that the monocycle pulse can be detected.

9.0 The Constant Q Gabor Wavelet

The Adaptive Gabor Representation (AGR) and the Combined and Single Wigner-Ville Distribution of the AGR were calculated for frequency hopping signals, pulses and radar return signals. The AGR requires finding the optimum wavelet center frequency, optimum dwell and optimum modulating envelope. The hypothesis under test was that whereas the AGR has been viewed as an optimization with respect to three variables: α_p , t_0 and f_0 , with α_p setting the envelope size independently of the other two variables, use of a constant Q Gabor wavelet would permit an efficient optimization using only one variable - α_p - with the other signal parameters functions of that one variable. It is shown that the constant Q

Gabor wavelet with $f_0 \cdot t_0 = \Delta f \cdot \Delta t = 1/2$, is optimum and that only one variable is required for optimization.

9.0.1 Adaptive Gabor Representation (AGR)⁸

The adaptive signal expansion is defined:

$$s(t) = \sum_p B_p h_p(t),$$

with the coefficients defined by:

$$B_p = \langle s, h_p \rangle.$$

The aim is to find $h_0(t)$ which is most similar to $s_0(t)$, i.e.,

$$|B_p|^2 = \max_{h_p} |\langle s_p(t) h_p(t) \rangle|^2. \quad \text{Step 1.}$$

Residuals are defined by:

$$s_{p+1}(t) = s_p(t) - B_p h_p(t). \quad \text{Step 2.}$$

If the functions, $h_p(t)$, have unit energy:

$$\|h_p(t)\|^2 = 1,$$

then the residual energy is:

$$\|s_{p+1}(t)\|^2 = \|s_p(t)\|^2 - |B_p|^2.$$

Step 1 is repeated to find $h_1(t)$ as a match to $s_1(t)$, then Step 2 is repeated and so on, as the residual signal converges to zero. It should be noted that, unlike the regular Gabor expansion, as well as wavelets, the set $\{h_p(t)\}$ will never be complete in L_2 , even if the residual converges to zero, because each set of adaptive elementary functions is unique to a particular signal.

As

⁸ Qian, S., Chen, D. & Chen, K., Signal approximation via data-adaptive normalized Gaussian functions and its applications for speech processing. *Proc. ICASSP-92*, San Francisco, CA March 23-26, 1992, pp. 141-144.

Qian, S. & Chen, D., Signal representation using adaptive normalized Gaussian functions. *Signal Processing*, 36, No 1, 1-11, March, 1994.

Mallat, S. & Zhang, Z., Matching pursuit with time-frequency dictionaries. *IEEE Trans. Signal Processing* 41, 3397-3415, 1993.

$$\|s(t)\|^2 = \sum_{p=0}^{\infty} |B_p|^2$$

and as

$$\frac{1}{2\pi} \iint WVD_{h_p}(t, \omega) dt d\omega = \|h_p(t)\|^2 = 1,$$

the Adaptive Spectrogram (AS) can be defined as:

$$AS(t, \omega) = \sum_p |B_p|^2 WVD_{h_p}(t, \omega),$$

where it should be noted that the summation is over rows.

The AS not only does not contain the cross-term interference of the Wigner-Ville distribution, it also satisfies the energy relation:

$$\|s(t)\|^2 = \frac{1}{2\pi} \iint AS(t, \omega) dt d\omega.$$

The choice of $h_p(t)$ is completely arbitrary. Following convention⁹, we choose the Gabor-type functions:

$$h_p(t) = \left(\frac{\alpha_p}{\pi}\right)^{1/4} \exp\left[-\frac{\alpha_p}{2}(t-t_{0_p})^2\right] \exp[if_{0_p}t],$$

where

$$\Delta t = \sqrt{\frac{1}{2} \cdot \frac{1}{\alpha_p}}; \quad \Delta f = \sqrt{\frac{1}{2} \cdot \frac{\alpha_p}{1}},$$

so that:

$$\Delta f \cdot \Delta t = \frac{1}{2}.$$

The Adaptive Gabor Representation (AGR) is then:

$$s(t) = \sum_p B_p h_p(t) = \sum_p B_p \left(\frac{\alpha_p}{\pi}\right)^{1/4} \exp\left[-\frac{\alpha_p}{2}(t-t_{0_p})^2\right] \exp[if_{0_p}t]$$

An important property of the AGR is that, unlike the Gabor expansion, for which the analysis and synthesis functions are not identical, the AGR has the same analysis and synthesis functions. The adaptive coefficients, B_p , are computed as follows:

⁹ Qian, S. & Chen, D., *Joint Time-Frequency Analysis*, Prentice-Hall, New York, 1996.

$$B_p = \int s_p(t) h_p^*(t) dt = \left(\frac{\alpha_p}{\pi} \right)^{1/4} \int s_p(t) \exp \left[-\frac{\alpha_p}{2} (t - t_{0_p})^2 \right] \exp \left[-i f_{0_p} t \right] dt$$

The AS can then be defined as:

$$AS(t, \omega) = 2 \sum_p |B_p|^2 \exp \left[-\left\{ \alpha_p (t - t_{0_p})^2 + \frac{1}{\alpha_p} (\omega - \omega_{0_p})^2 \right\} \right],$$

where again it should be noted that this is the summation of the Wigner-Ville distribution over rows.

9.0.2 Wigner-Ville of the AGR.

The Wigner-Ville joint time-frequency density function of the adaptive Gabor functions is:

$$WVD_{h_p}(t, \omega) = 2 \exp \left[-\left\{ \alpha_p (t - t_0)^2 + \frac{(\omega - \omega_0)^2}{\alpha_p} \right\} \right].$$

9.0.3 The Constant Q Gabor Wavelet.

In previous expositions of the AGR, the four signal variables of center frequency, f_0 , midperiod, t_0 , frequency bandwidth Δf and time bandwidth, Δt , are separately defined. For example,

$$\Delta f = \sqrt{\frac{1}{2} \left(\frac{\alpha_p}{1} \right)},$$

$$\Delta t = \sqrt{\frac{1}{2} \left(\frac{1}{\alpha_p} \right)},$$

with

$$f_0 = \text{mid } \Delta f,$$

$$t_0 = \text{mid } \Delta t.$$

Obviously, this does not provide a constant Q wavelet.

However, a constant Q Gabor wavelet is achieved from the following definitions¹⁰:

¹⁰ Barrett, T.W., Structural information theory. *J. Acoust. Soc. Am.*, 54, 1092-1098, 1973.

$$f_0 = \sqrt{8\alpha_p},$$

$$t_0 = \sqrt{\frac{1}{32} \frac{1}{\alpha_p}},$$

$$\Delta f = \sqrt{\frac{1}{2} \frac{\alpha_p}{1}},$$

$$\Delta t = \sqrt{\frac{1}{2} \frac{1}{\alpha_p}}.$$

The constant Q Gabor wavelet thus conforms to the following condition:

$$f_0 \cdot t_0 = \Delta f \cdot \Delta t = \frac{1}{2},$$

and the more general condition is¹¹:

$$f_0 \cdot t_0 = \Delta f \cdot \Delta t = \frac{1}{2}(2n+1) \quad n = 0, 1, 2, \dots$$

9.1 Numerical Tests.

The hypothesis under test was that whereas the AGR has been viewed as an optimization with respect to three variables: α_p , t_0 and f_0 , with α_p setting the envelope size independently of the other two variables, use of a constant Q Gabor wavelet would permit an efficient optimization using only one variable - α_p - with the other signal parameters functions of that one variable.

Using the frequency hopping signal plus a pulse shown in Fig. 9.1, a non-constant Q analysis was calculated with $4f_0$ s and 1 original signal plus 4 residuals - Fig. 9.2. The Combined Wigner-Ville distribution picks out the frequency components of the signal -

-
- ¹¹ Barrett, T.W., On vibrating strings and information theory. *J. Sound & Vibration*, 20, 407-412, 1972a.
 _____, Conservation of information. *Acustica*, 27, 44-47, 1972b.
 _____, The definition precedence of signal parameters: sequential versus simultaneous information. *Acustica*, 27, 90-93, 1972c.
 _____, The conceptual basis of two information theories - a reply to some criticisms. *J. Sound & Vibration*, 25, 638-642, 1972d.
 _____, Analytical information theory. *Acustica*, 29, 65-67, 1973.
 _____, Nonlinear analysis and structural information theory: a comparison of mathematical and physical derivations. *Acustica*, 33, 149-165, 1975.
 _____, On linearizing nonlinear systems. *J. Sound & Vibration*, 39, 265-268, 1975.
 _____, Linearity in secular systems: four parameter superposition. *J. Sound & Vibration*, 41, 259-261, 1975.
 _____, Information measurement I. On Maximum entropy conditions applied to elementary signals. *Acustica*, 35, 80-85, 1975.
 _____, Information measurement II. On minimum conditions of energy order applied to elementary signals. *Acustica*, 36, 282-286, 1975.
 _____, Structural information theory of sound. *Acustica*, 36, 271-281, 1976.

Fig. 9.3; and the individual Wigner-Ville distributions pick out the individual signal frequency components - Figs 9.4-9.7.

Calculating the AGR of the frequency components of the signal but with increasing modulating envelope, Fig. 9.8, revealed that the constant Q Gabor wavelet provided more detail than did longer envelopes and did not overlap the temporal length of the frequency components in the signal. This result established that a constant Q Gabor wavelets are optimum filters.

Using high frequency Gabor wavelets, the pulse was extracted from the signal shown in Fig. 9.1 - Fig. 9.9; and using the Combined Wigner-Ville distribution represented in Fig. 9.10.

Similar calculations were then performed on the representative radar return signal - Fig. 9.11. The AGR was calculated - Fig. 9.12 - and the Combined Wigner-Ville distribution is shown in Figs. 9.13(I) and 9.13(II) at two levels of magnification. Fig. 9.14 shows the Combined WV for the high frequency components of the signal and Figs. 9.15 - 9.18 show the WV for decreasing frequency components of the signal.

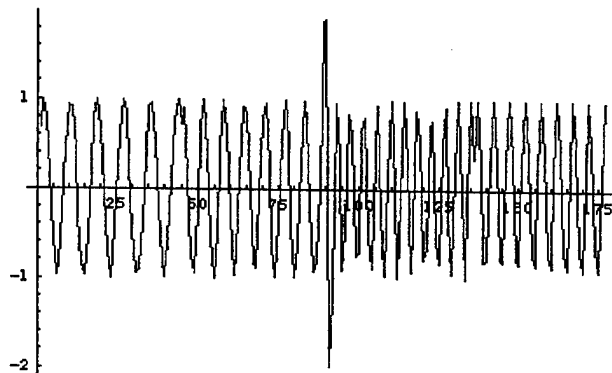
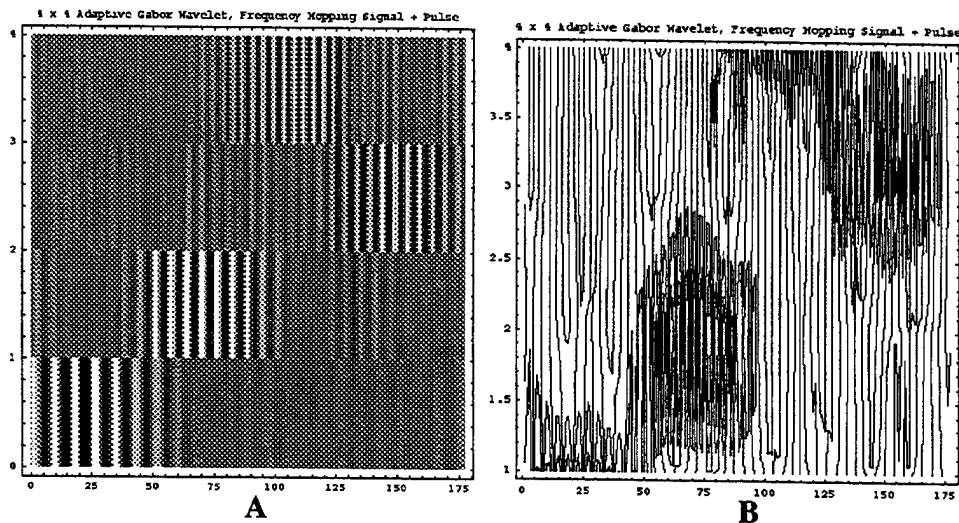
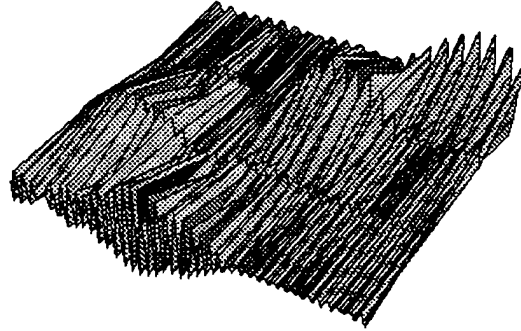


Fig. 9.1. Frequency Hopping Signal with Pulse.



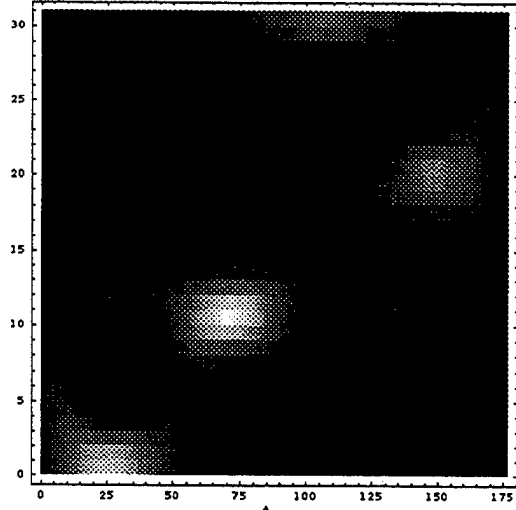
4 x 4 Adaptive Gabor Wavelet, Frequency Hopping signal + Pulse



C

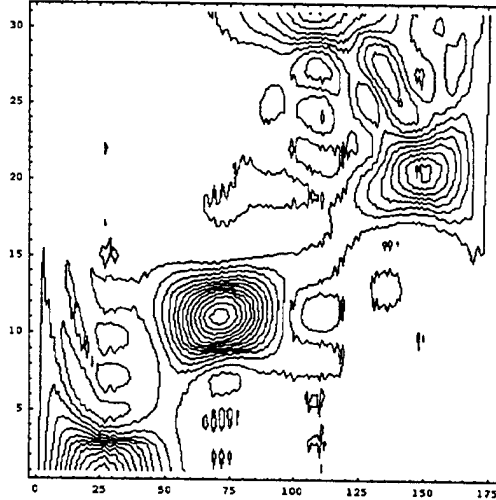
Fig. 9.2. Adaptive Gabor-Wavelet Transform of frequency hopping signal with pulse signal of Fig. 9.1. 4 f_0 s were used and 1 original signal plus 4 residuals.

Combined Wigner-Ville Function, 4 x 4 Adaptive Gabor Wavelet, Frequency Hopping signal + Pulse



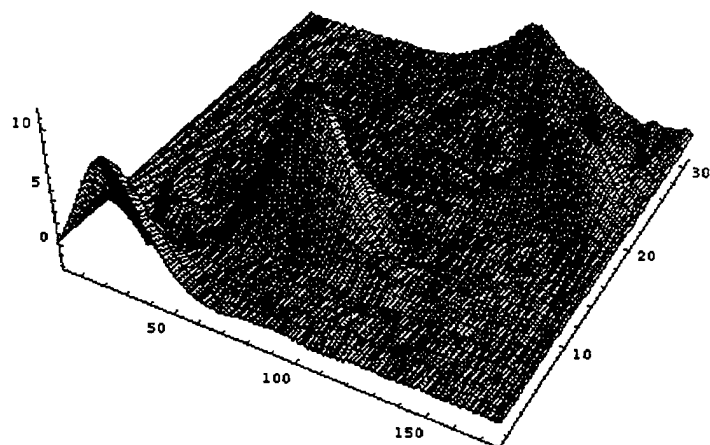
A

Combined Wigner-Ville Function, 5 x 6 Adaptive Gabor Wavelet, Frequency Hopping signal + Pulse



B

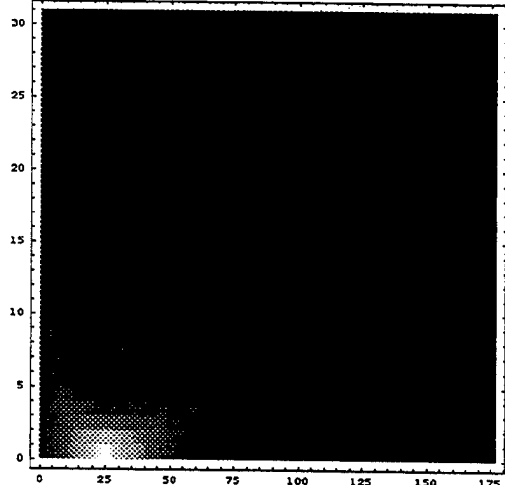
Combined Wigner-Ville Function, 5 x 6 Adaptive Gabor Wavelet, Frequency
Hopping Signal + Pulse



C

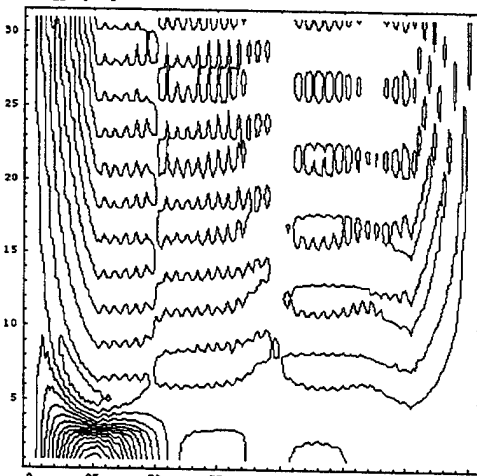
Fig. 9.3. Combined Wigner-Ville Distribution Transform of the 4 x 4 Adaptive Gabor-Wavelet Transform of Fig. 9.2.

#1 Wigner-Ville Function, 4 x 4 Adaptive Gabor Wavelet, Frequency
Hopping Signal + Pulse



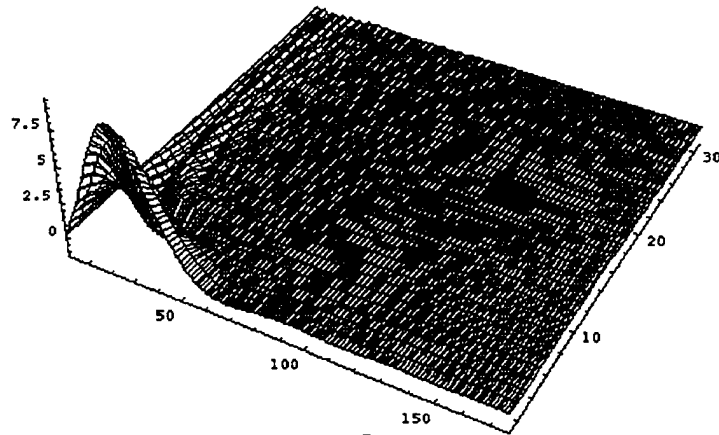
A

#1 Wigner-Ville Function, 4 x 4 Adaptive Gabor Wavelet, Frequency
Hopping Signal + Pulse



B

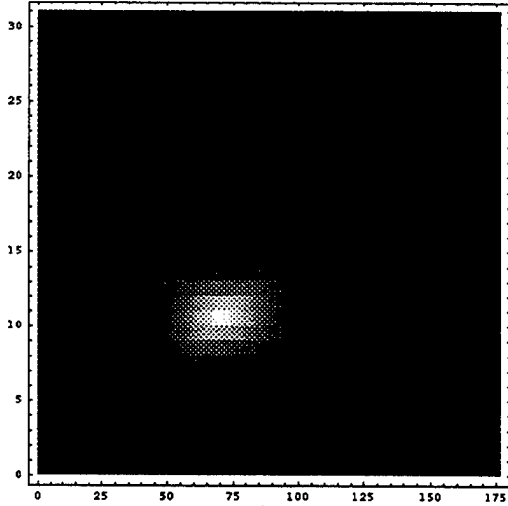
#1 Wigner-Ville Function, 4 x 4 Adaptive Gabor Wavelet, Frequency
Hopping Signal + Pulse



C

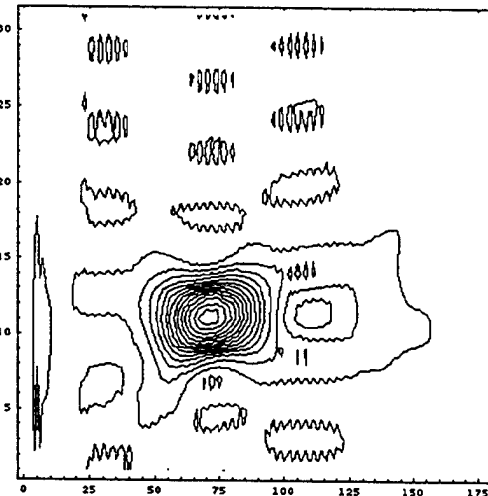
Fig. 9.4. Single Wigner-Ville Distribution Transform of the 1st part of the 4 x 4 Adaptive Gabor-Wavelet Transform of Fig. 9.2.

#2 Wigner-Ville Function, 4 x 4 Adaptive Gabor Wavelet, Frequency
Hopping Signal + Pulse



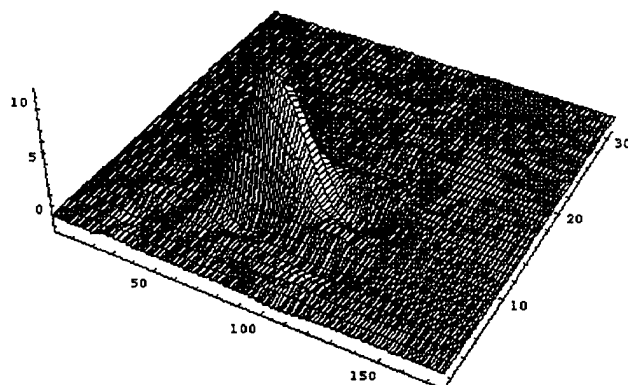
A

#2 Wigner-Ville Function, 4 x 4 Adaptive Gabor Wavelet, Frequency
Hopping Signal + Pulse



B

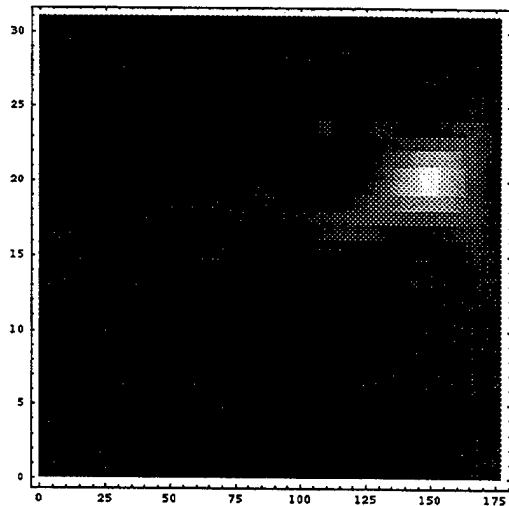
#2 Wigner-Ville Function, 4 x 4 Adaptive Gabor Wavelet, Frequency
Hopping Signal + Pulse



C

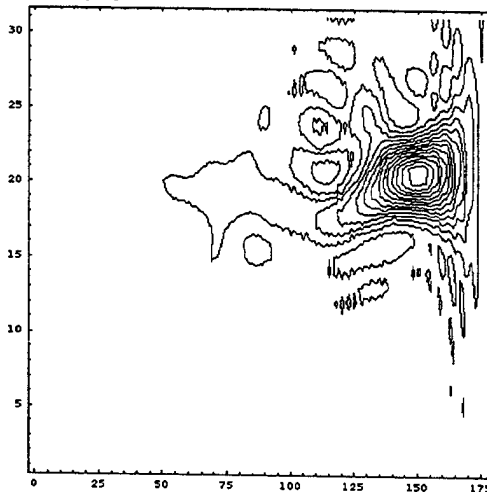
Fig. 9.5. Single Wigner-Ville Distribution Transform of the 2nd part of the 4 x 4 Adaptive Gabor-Wavelet Transform of Fig. 9.2.

#3 Wigner-Ville Function, 4 x 4 Adaptive Gabor Wavelet, Frequency
Hopping Signal + Pulse



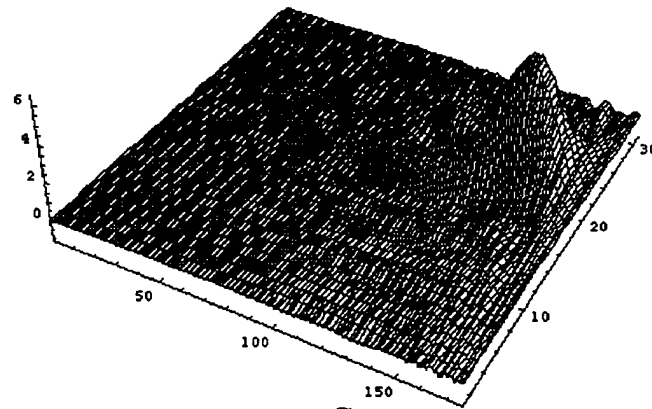
A

#3 Wigner-Ville Function, 4 x 4 Adaptive Gabor Wavelet, Frequency
Hopping Signal + Pulse



B

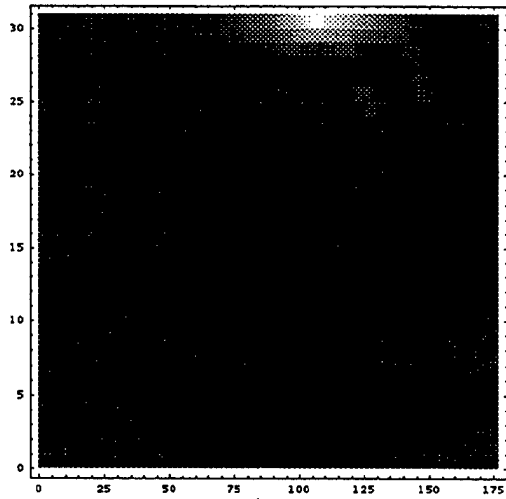
#3 Wigner-Ville Function, 4 x 4 Adaptive Gabor Wavelet, Frequency
Hopping Signal + Pulse



C

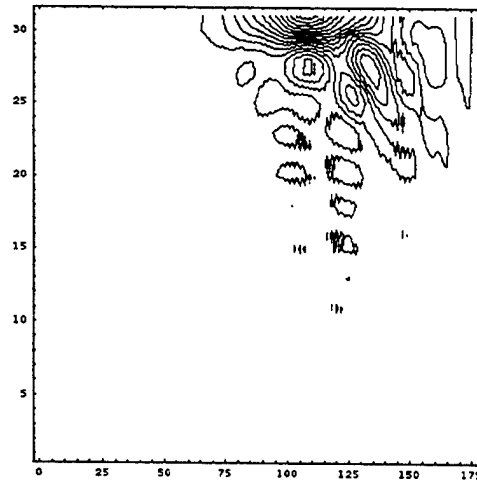
Fig. 9.6. Single Wigner-Ville Distribution Transform of the 3rd part of the 4 x 4 Adaptive Gabor-Wavelet Transform of Fig. 9.2.

#4 Wigner-Ville Function, 4 x 4 Adaptive Gabor Wavelet, Frequency
Hopping Signal + Pulse



A

#4 Wigner-Ville Function, 4 x 4 Adaptive Gabor Wavelet, Frequency
Hopping Signal + Pulse



B

#1 Wigner-Ville Function, 4 x 4 Adaptive Gabor Wavelet, Frequency Hopping Signal + Pulse

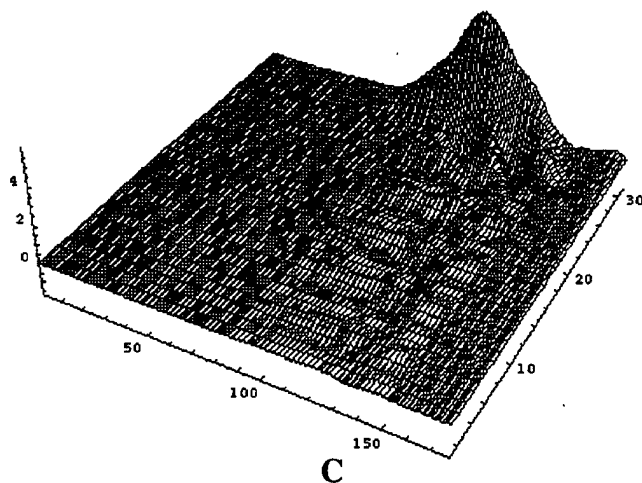
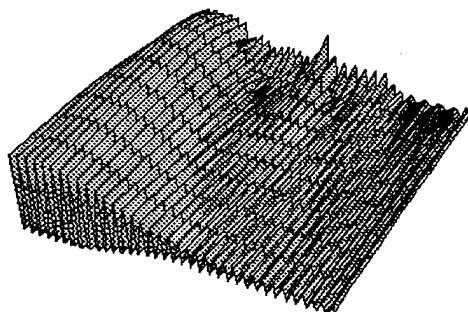


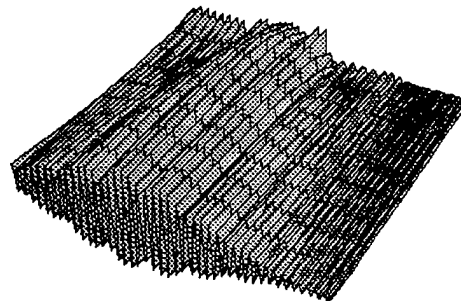
Fig. 9.7. Single Wigner-Ville Distribution Transform of the 3rd part of the 4 x 4 Adaptive Gabor-Wavelet Transform of Fig. 9.2.

5 Adaptive Gabor Wavelet, $f = 1.25$, envelope 1-10, Frequency Hopping Signal + Pulse ; 5 Adaptive Gabor Wavelet, $f = 1.50$, envelope 1-10, Frequency Hopping Signal + Pulse



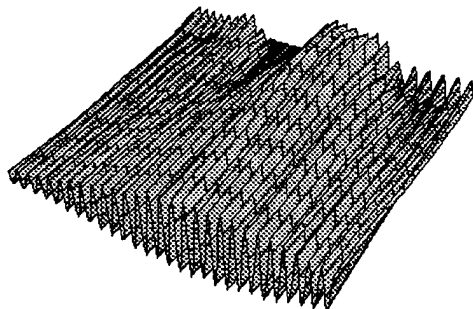
A

5 x 5 Adaptive Gabor Wavelet, $f = 1.00$, envelope 1-10, Frequency Hopping Signal + Pulse

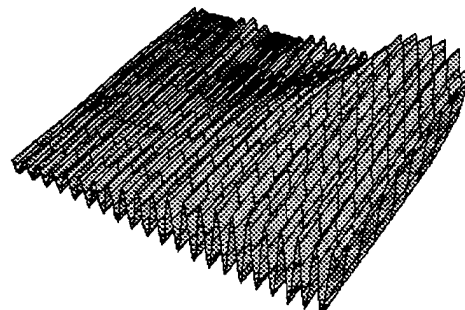


B

5 x 5 Adaptive Gabor Wavelet, $f = 0.75$, envelope 1-10, Frequency Hopping Signal + Pulse



C



D

Fig. 9.8. Adaptive Gabor Wavelet Transform of parts of signal of Fig. 9.1, with increasing modulating envelope.

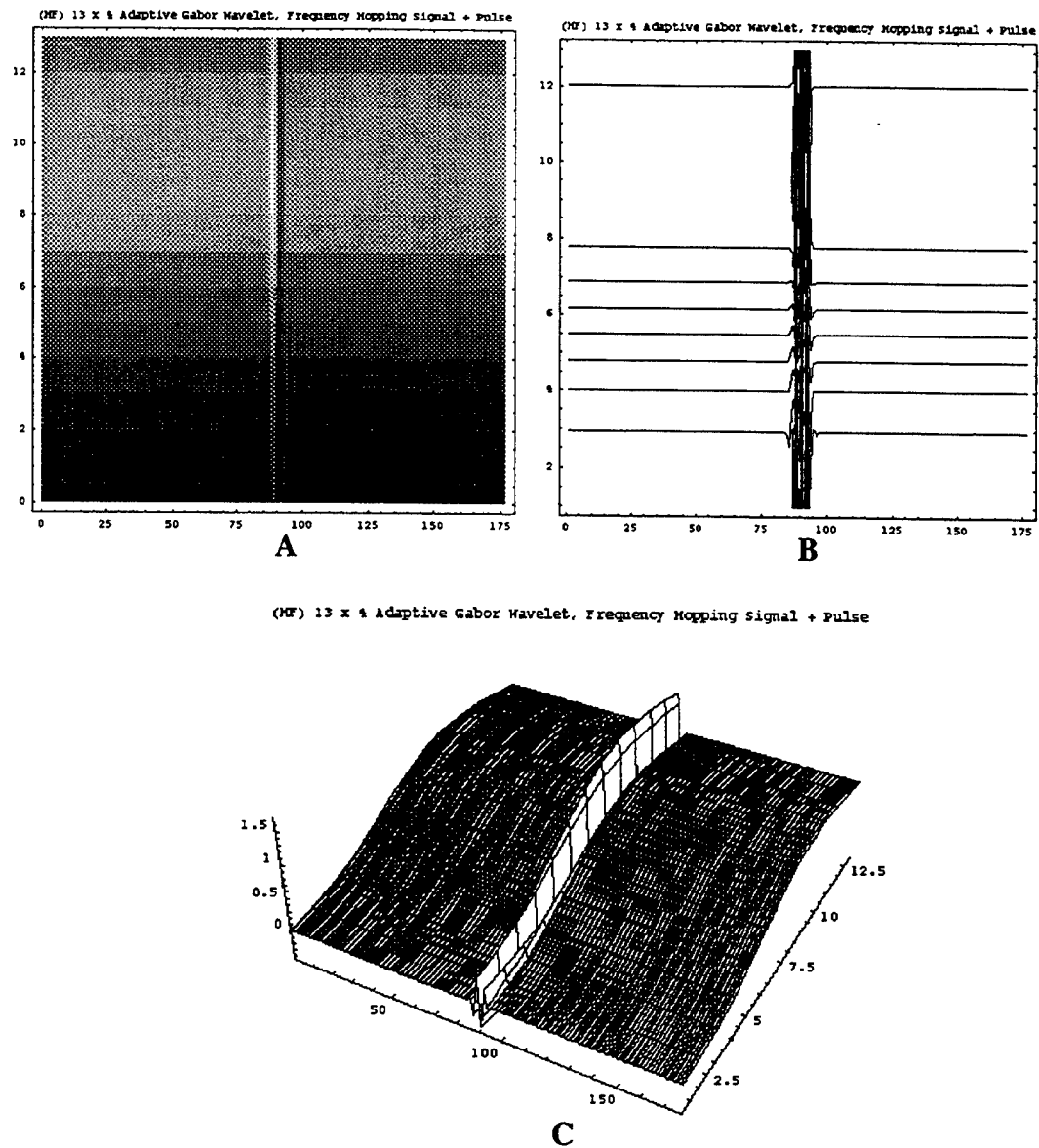
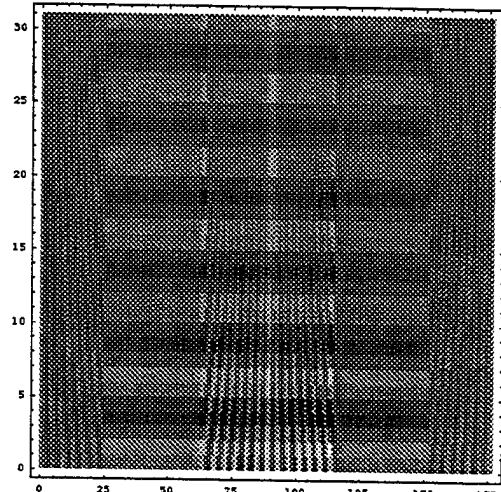


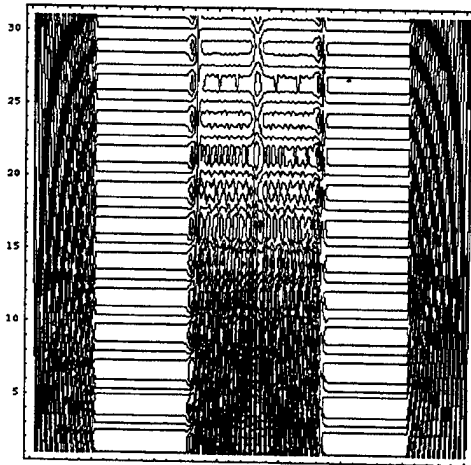
Fig. 9.9. Adaptive Gabor Wavelet transform using high frequency components of the signal of Fig. 9.1.

Combined Wigner-Ville Function, 13 x 4 Adaptive Gabor Wavelet, Frequency
Hopping Signal + Pulse



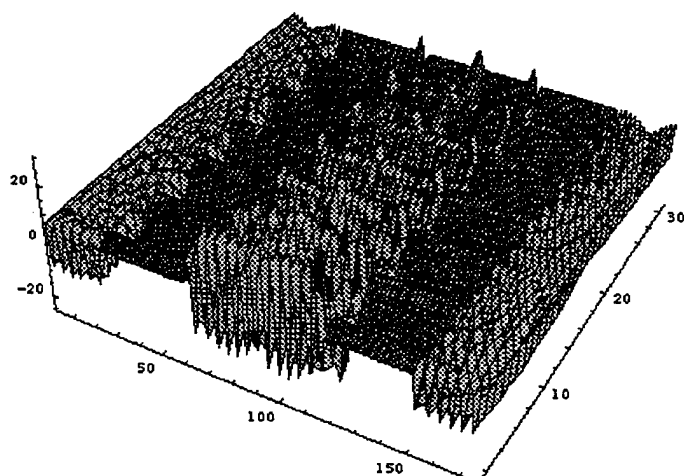
A

Combined Wigner-Ville Function, 13 x 4 Adaptive Gabor Wavelet, Frequency
Hopping Signal + Pulse



B

Combined Wigner-Ville Function, 13 x 4 Adaptive Gabor Wavelet, Frequency
Hopping Signal + Pulse



C

Fig. 9.10. Combined Wigner-Ville transform of the high frequency components of the frequency hopping signal plus pulse of Fig. 9.1.

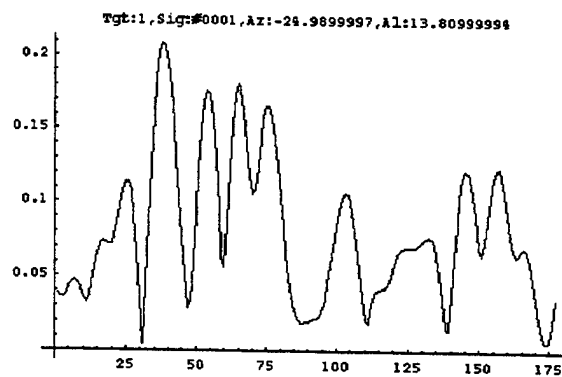
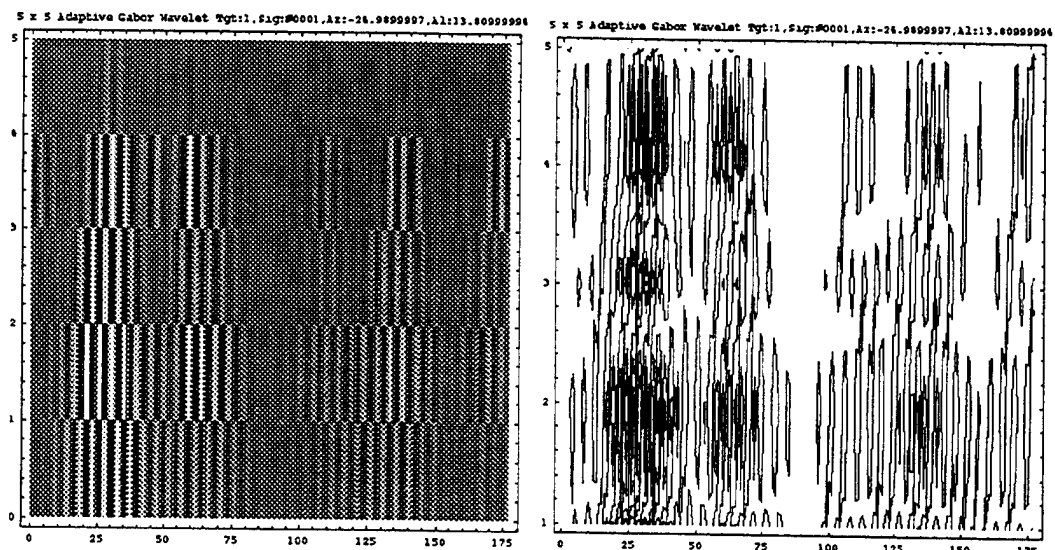


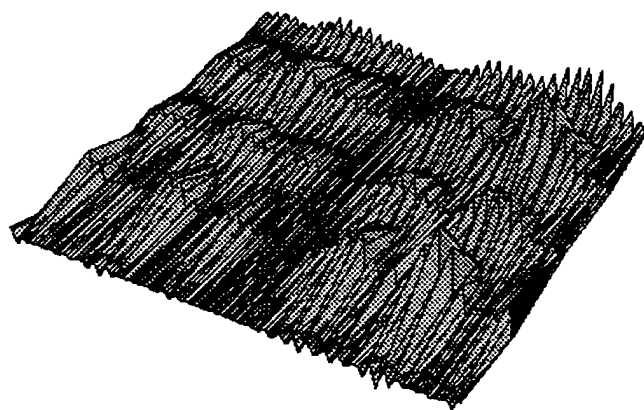
Fig. 9.11. Representative radar return signal.



A

B

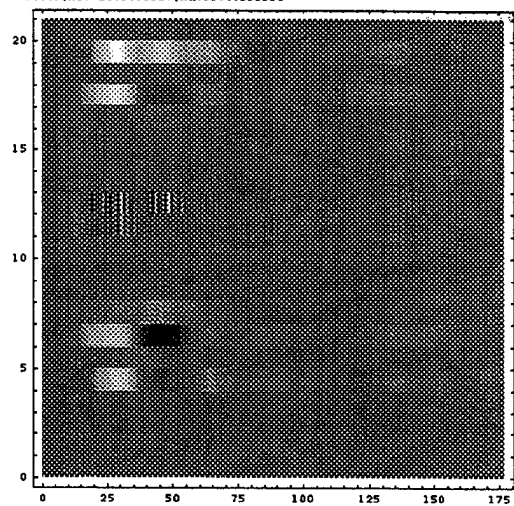
5 x 5 Adaptive Gabor Wavelet Tgt:1, Sig:#0001, Az:-24.9899997, Al:13.80999994



C

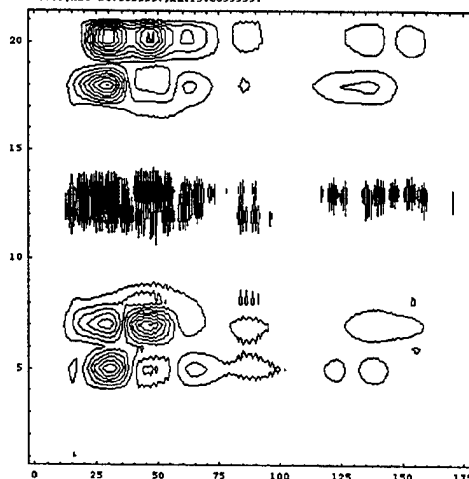
Fig. 9.12. Adaptive Gabor-Wavelet Transform of representative signal of Fig. 9.11. $5 f_0$ s were used and 1 original signal plus 4 residuals.

Combined Wigner-Ville Function, 5 x 5 Adaptive Gabor Wavelet Tgt:1,Sig:
#0001,Az:-24.9899997,Al:13.80999994



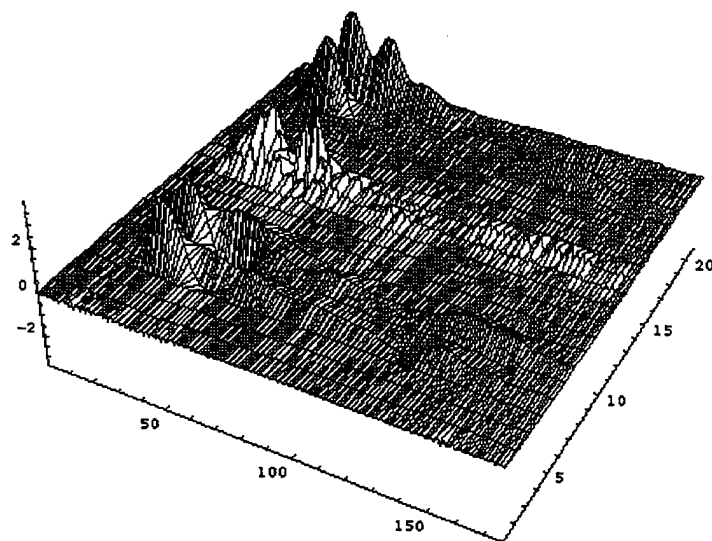
(I)A.

Combined Wigner-Ville Function, 5 x 5 Adaptive Gabor Wavelet Tgt:1,Sig:
#0001,Az:-24.9899997,Al:13.80999994



(I)B.

Combined Wigner-Ville Function, 5 x 5 Adaptive Gabor Wavelet Tgt:1,Sig:
#0001,Az:-24.9899997,Al:13.80999994



(I)C.

Fig. 9.13(I). Combined Wigner-Ville Distribution Transform of the 5 x 5 Adaptive Gabor-Wavelet Transform of Fig. 9.2.

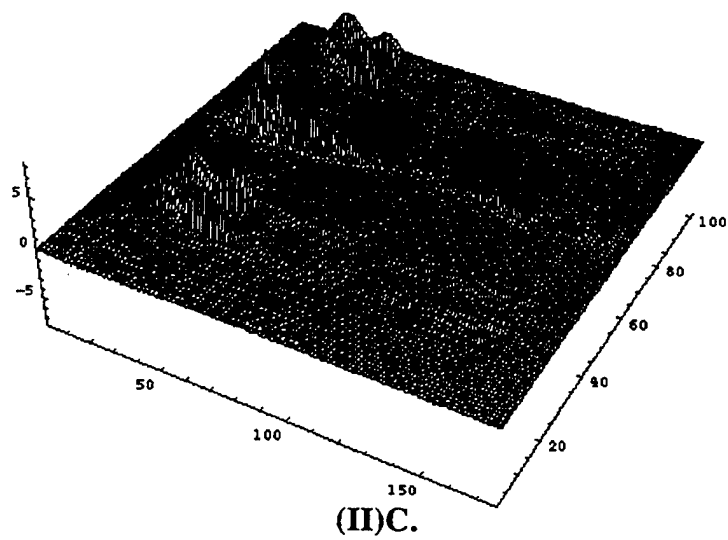
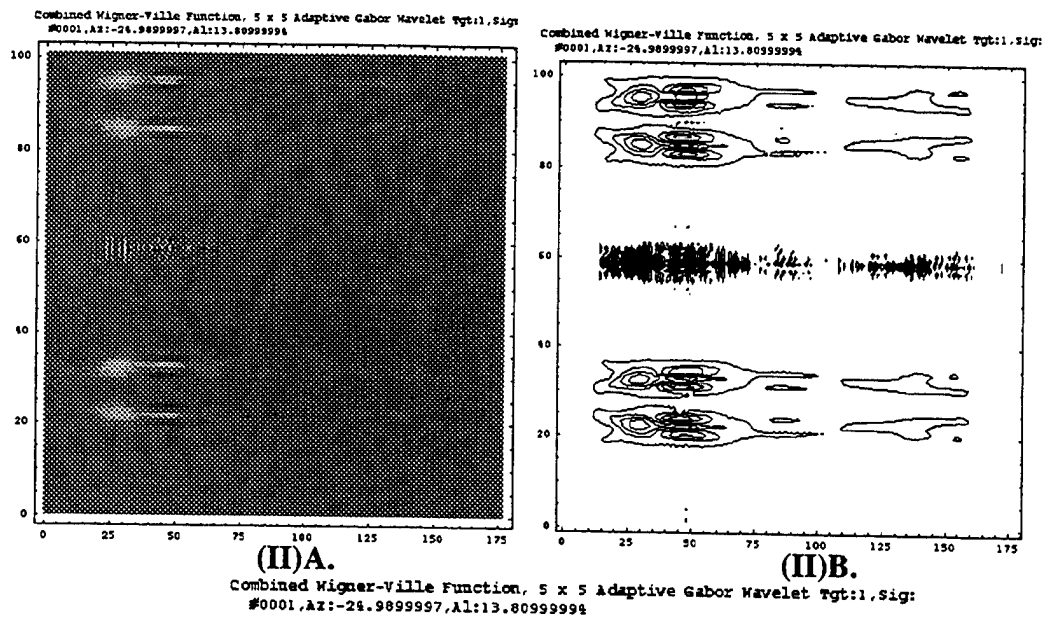
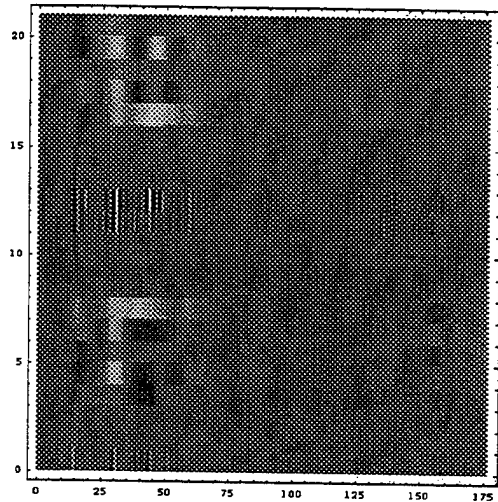


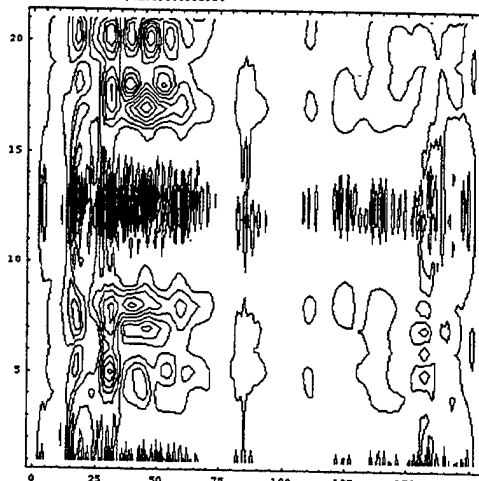
Fig. 9.13(II). Combined Wigner-Ville Distribution Transform of the 5 x 5 Adaptive Gabor-Wavelet Transform of Fig. 9.2. Same as Fig. 9.13(I) but x 5 magnification.

#5 Wigner-Ville Function, 5 x 5 Adaptive Gabor Wavelet Tgt:1, Sig:#0001,
Az:-24.9899997,Al:13.80999994



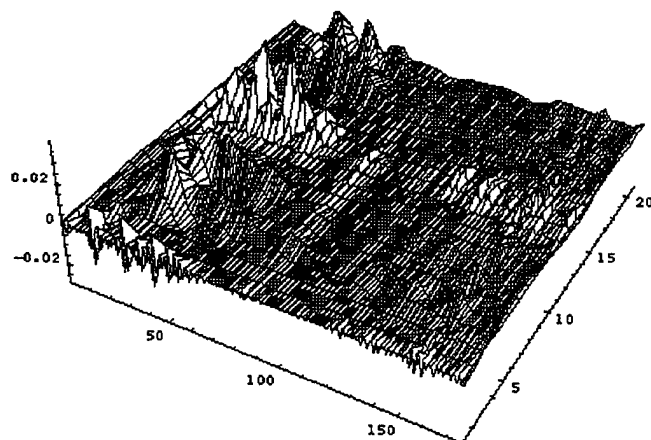
A

#5 Wigner-Ville Function, 5 x 5 Adaptive Gabor Wavelet Tgt:1, Sig:#0001,
Az:-24.9899997,Al:13.80999994



B

#5 Wigner-Ville Function, 5 x 5 Adaptive Gabor Wavelet Tgt:1, Sig:#0001,
Az:-24.9899997,Al:13.80999994



C

Fig. 9.14. Wigner-Ville Distribution Transform of the 5th level (highest frequency components) x 5 Adaptive Gabor-Wavelet Transform of Fig. 9.2.

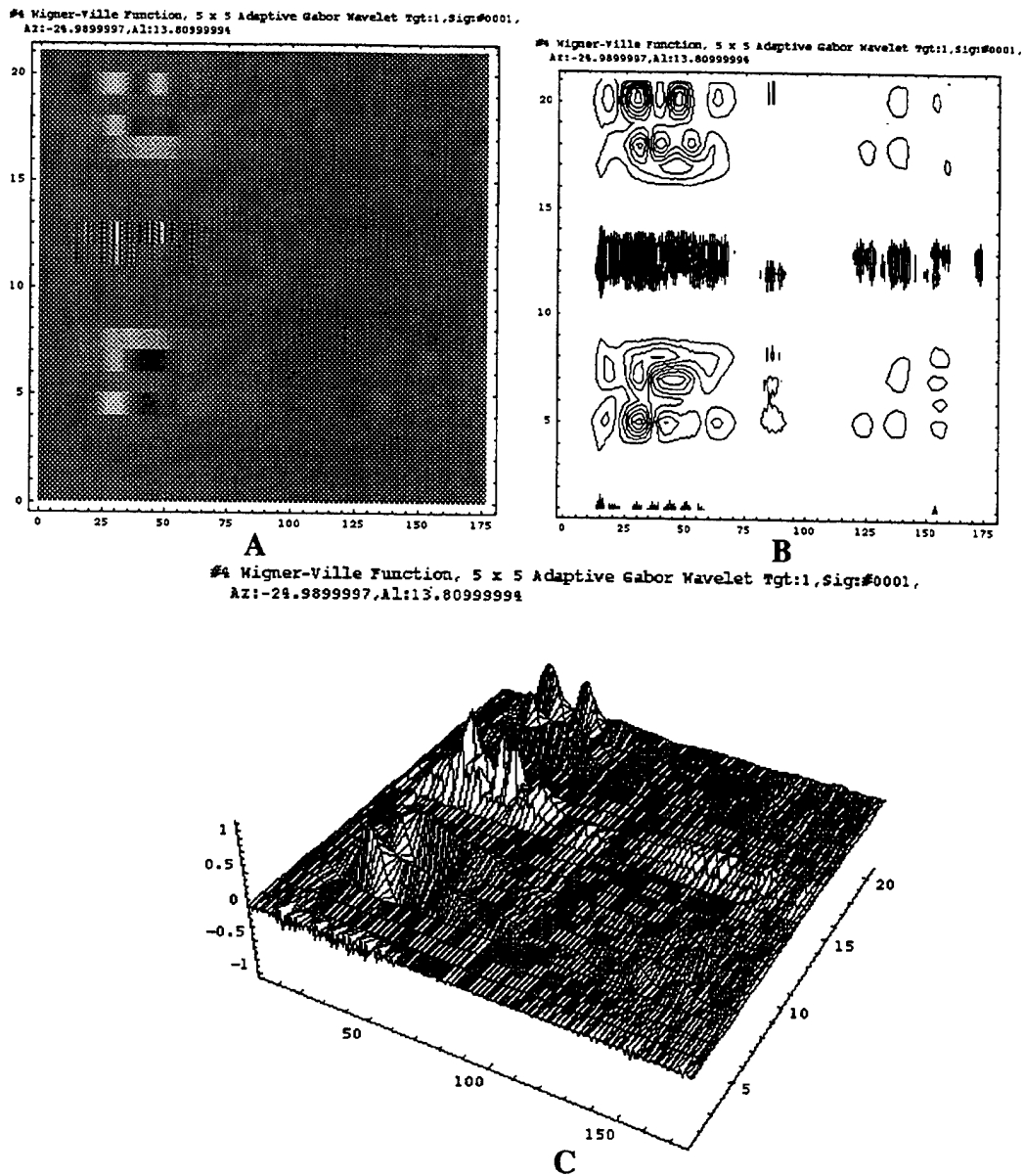
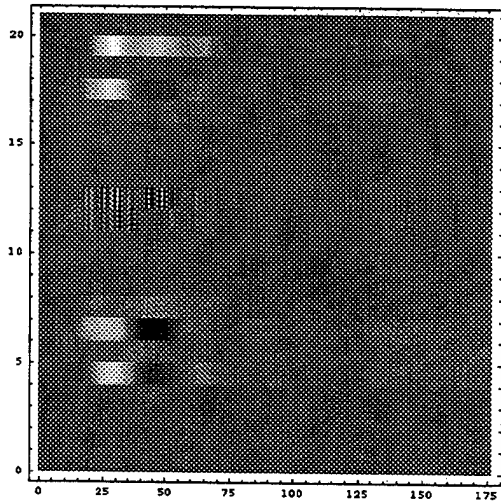


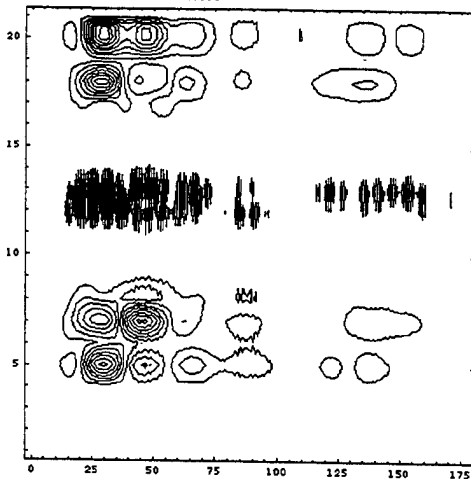
Fig. 9.15. Wigner-Ville Distribution Transform of the 4th level (next to highest frequency) x 5 Adaptive Gabor-Wavelet Transform of Fig. 9.12.

#3 Wigner-Ville Function, 5 x 5 Adaptive Gabor Wavelet Tgt:1, Sig:#0001,
Az:-24.9899997,Al:13.80999999



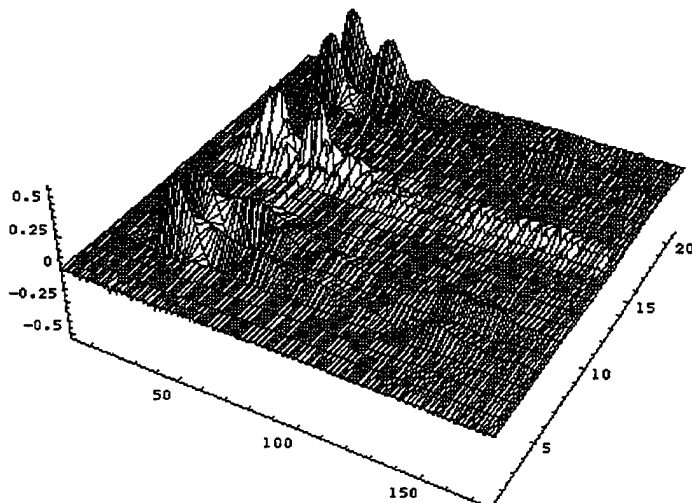
A

#3 Wigner-Ville Function, 5 x 5 Adaptive Gabor Wavelet Tgt:1, Sig:#0001,
Az:-24.9899997,Al:13.80999999



B

#3 Wigner-Ville Function, 5 x 5 Adaptive Gabor Wavelet Tgt:1, Sig:#0001,
Az:-24.9899997,Al:13.80999999



C

Fig. 9.16. Wigner-Ville Distribution Transform of the 3rd level (middle frequencies) x 5 Adaptive Gabor-Wavelet Transform of Fig. 9.12.

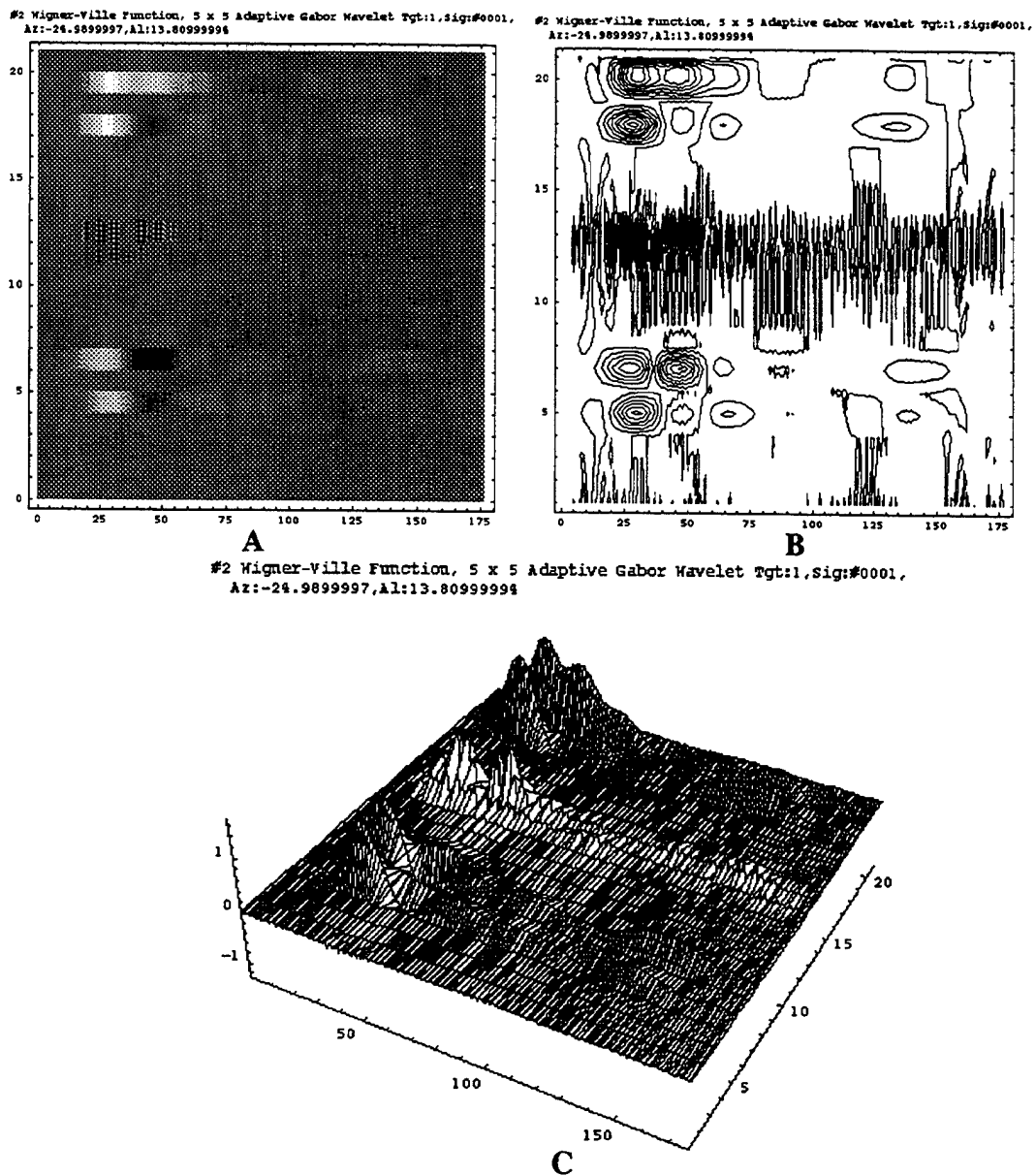
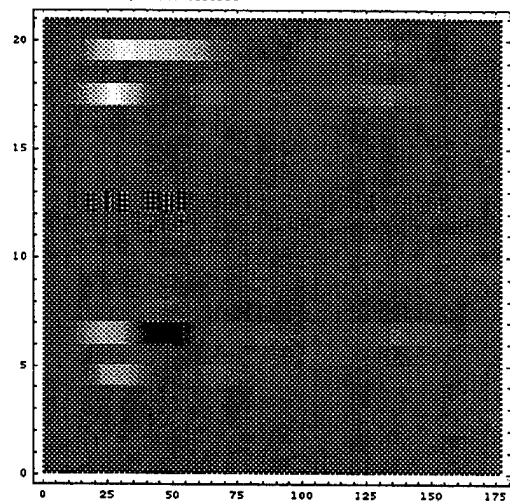


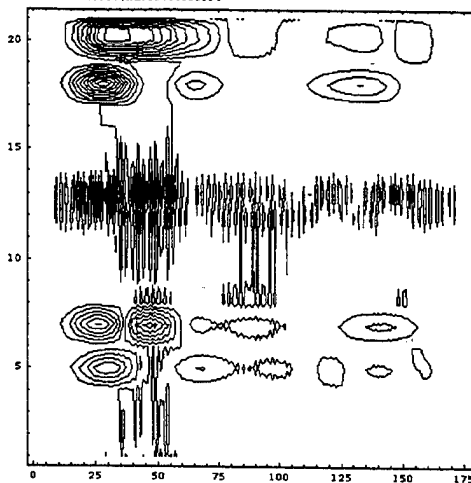
Fig. 9.17. Wigner-Ville Distribution Transform of the 2nd level (next to lowest frequency) x 5 Adaptive Gabor-Wavelet Transform of Fig. 9.12.

#1 Wigner-Ville Function, 5 x 5 Adaptive Gabor Wavelet Tgt:1, Sig:#0001,
Az:-24.9899997,Al:13.80999994



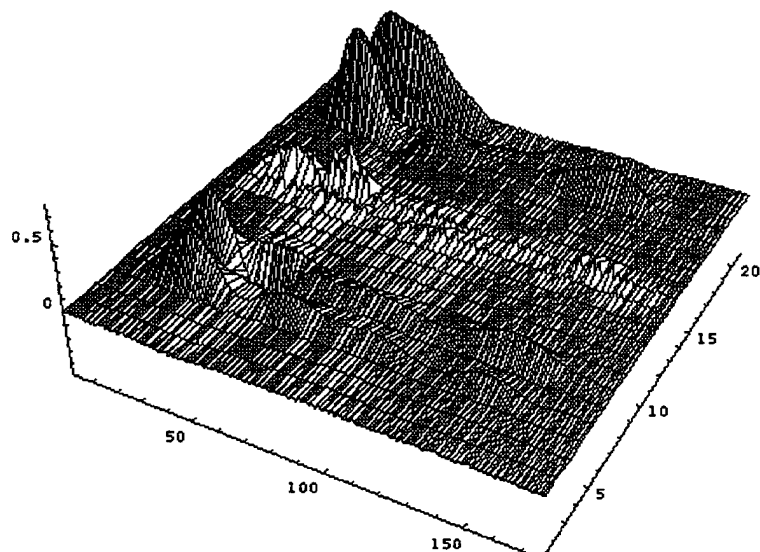
A

#1 Wigner-Ville Function, 5 x 5 Adaptive Gabor Wavelet Tgt:1, Sig:#0001,
Az:-24.9899997,Al:13.80999994



B

#1 Wigner-Ville Function, 5 x 5 Adaptive Gabor Wavelet Tgt:1, Sig:#0001,
Az:-24.9899997,Al:13.80999994



C

Fig. 9.18. Wigner-Ville Distribution Transform of the 1st level (lowest frequency components) x 5 Adaptive Gabor-Wavelet Transform of Fig. 9.12.

10.0 Extension of the Gabor Transform (CQOW)

We initiated investigations of wavelets based on orthogonal parabolic cylinder or Weber functions of increasing level described by the expansions: $\Delta f \Delta t = f_0 t_0 = 1/2 (2n + 1)$, $n = 0, 1, 2, \dots$ (i.e., Constant Q Orthogonal Weber Function Wavelets (CQOWs)). Using a frequency hopping and pulse test signals, these wavelets are able to detect both resonance and pulse scattering features. Using scattergram plots between three levels of wavelets and two scale dilations, unique features of both the test signal and radar return signals can be demonstrated. *This research is unique in two respects: using orthogonal wavelets of different levels and in the scatterogram cross-comparison of three levels of analysis, which can provide unique signatures for targets.* In the case of the test signal of a frequency hopping signal, plus a pulse, it is seen that discernible cyclic patterns occur which may be correlated with the number of frequencies in the signal - four. In the case of the radar return test signal, it is seen that recognizable helical patterns occur, which may provide a unique signature for targets.

In previous expositions of the Gabor transform, the four signal variables of center frequency, f_0 , midperiod, t_0 , frequency bandwidth Δf and time bandwidth, Δt , are separately defined. For example,

$$\Delta f = \sqrt{\frac{1}{2} \left(\frac{\alpha_p}{1} \right)},$$

$$\Delta t = \sqrt{\frac{1}{2} \left(\frac{1}{\alpha_p} \right)},$$

with

$$f_0 = \text{mid } \Delta f,$$

$$t_0 = \text{mid } \Delta t.$$

Obviously, this does not provide a constant Q wavelet.

However, a constant Q Gabor wavelet is achieved from the following definitions¹:

$$f_0 = \sqrt{8\alpha_p},$$

$$t_0 = \sqrt{\frac{1}{32} \frac{1}{\alpha_p}},$$

$$\Delta f = \sqrt{\frac{1}{2} \frac{\alpha_p}{1}},$$

$$\Delta t = \sqrt{\frac{1}{2} \frac{1}{\alpha_p}}.$$

The constant Q Gabor wavelet thus conforms to the following condition:

¹ Barrett, T.W., Structural information theory. *J. Acoust. Soc. Am.*, 54, 1092-1098, 1973.

$$f_0 \cdot t_0 = \Delta f \cdot \Delta t = \frac{1}{2},$$

A more general condition has been derived²:

$$f_0 \cdot t_0 = \Delta f \cdot \Delta t = \frac{1}{2}(2n+1) \quad n = 0, 1, 2, \dots$$

which provides a range of orthogonal wavelets.

Specifically, these wavelets are based on modulations which are Weber's functions. Weber's equation is:

$$\frac{d^2 D}{dt^2} + (\lambda - \xi^2) D = 0,$$

where ξ is a dimensionless independent variable and λ is a dimensionless eigenvalue. The solutions to Weber's equation are the parabolic cylinder or Weber-Hermite functions:

$$D_n(t) = 2^{-n/2} H_n\left(\frac{t}{\sqrt{2}}\right) \exp\left[-\frac{t^2}{4}\right],$$

where

$$H_n(t) = (-1)^n \exp[t^2] \frac{\partial^n \exp[-t^2]}{\partial t^n}$$

are Hermite polynomials satisfying:

$$\frac{d^2 x}{dt^2} - 2t \frac{dx}{dt} - 2nx = 0$$

and the orthogonality relationship:

-
- ² Barrett, T.W., On vibrating strings and information theory. *J. Sound & Vibration*, 20, 407-412, 1972a.
 _____, Conservation of information. *Acustica*, 27, 44-47, 1972b.
 _____, The definition precedence of signal parameters: sequential versus simultaneous information. *Acustica*, 27, 90-93, 1972c.
 _____, The conceptual basis of two information theories - a reply to some criticisms. *J. Sound & Vibration*, 25, 638-642, 1972d.
 _____, Analytical information theory. *Acustica*, 29, 65-67, 1973.
 _____, Nonlinear analysis and structural information theory: a comparison of mathematical and physical derivations. *Acustica*, 33, 149-165, 1975.
 _____, On linearizing nonlinear systems. *J. Sound & Vibration*, 39, 265-268, 1975.
 _____, Linearity in secular systems: four parameter superposition. *J. Sound & Vibration*, 41, 259-261, 1975.
 _____, Information measurement I. On Maximum entropy conditions applied to elementary signals. *Acustica*, 35, 80-85, 1975.
 _____, Information measurement II. On minimum conditions of energy order applied to elementary signals. *Acustica*, 36, 282-286, 1975.
 _____, Structural information theory of sound. *Acustica*, 36, 271-281, 1976.

$$\int_{-\infty}^{+\infty} H_m(t) H_n(t) \exp[-t^2] dt = 0 \text{ for } m \neq n.$$

The Weber functions, 0'th to 6th order, are:

Weber Functions - see Fig. 10.1.	
ORDER (LEVEL)	
0'th order, $n=0$	$2^{-0/2} H_0\left(\frac{t}{\sqrt{2}}\right) \exp\left[\frac{-t^2}{4}\right]$
1st order, $n=1$	$2^{-1/2} H_1\left(\frac{t}{\sqrt{2}}\right) \exp\left[\frac{-t^2}{4}\right]$
2nd order, $n=2$	$2^{-2/2} H_2\left(\frac{t}{\sqrt{2}}\right) \exp\left[\frac{-t^2}{4}\right]$
3rd order, $n=3$	$2^{-3/2} H_3\left(\frac{t}{\sqrt{2}}\right) \exp\left[\frac{-t^2}{4}\right]$
4th order, $n=4$	$2^{-4/2} H_4\left(\frac{t}{\sqrt{2}}\right) \exp\left[\frac{-t^2}{4}\right]$
5th order, $n=5$	$2^{-5/2} H_5\left(\frac{t}{\sqrt{2}}\right) \exp\left[\frac{-t^2}{4}\right]$
6th order, $n=6$	$2^{-6/2} H_6\left(\frac{t}{\sqrt{2}}\right) \exp\left[\frac{-t^2}{4}\right]$

The Weber function wavelets, 0'th to 6th order, are:

Constant Q Weber Function Wavelets, see Fig. 10.2	
ORDER (LEVEL)	
0'th order, $n=0$	$2^{-0/2} H_0\left(\frac{t}{\sqrt{2}}\right) \exp\left[\frac{-t^2}{4}\right] \exp[i(4/1)t]$
1st order, $n=1$	$2^{-1/2} H_1\left(\frac{t}{\sqrt{2}}\right) \exp\left[\frac{-t^2}{4}\right] \exp[i(4/3)t]$
2nd order, $n=2$	$2^{-2/2} H_2\left(\frac{t}{\sqrt{2}}\right) \exp\left[\frac{-t^2}{4}\right] \exp[i(4/5)t]$
3rd order, $n=3$	$2^{-3/2} H_3\left(\frac{t}{\sqrt{2}}\right) \exp\left[\frac{-t^2}{4}\right] \exp[i(4/7)t]$
4th order, $n=4$	$2^{-4/2} H_4\left(\frac{t}{\sqrt{2}}\right) \exp\left[\frac{-t^2}{4}\right] \exp[i(4/9)t]$
5th order, $n=5$	$2^{-5/2} H_5\left(\frac{t}{\sqrt{2}}\right) \exp\left[\frac{-t^2}{4}\right] \exp[i(4/11)t]$
6th order, $n=6$	$2^{-6/2} H_6\left(\frac{t}{\sqrt{2}}\right) \exp\left[\frac{-t^2}{4}\right] \exp[i(4/11)t]$

At the 0'th order, i.e., $n = 0$, the Weber-Hermite function is the well-known Gaussian and the Weber Function wavelet of the 0'th order is a unique Gabor function - a constant Q Gabor function - due to the two uncertainty restrictions described above. This 0'th order wavelet is:

$$s(t) = \frac{\alpha_p^{1/4}}{\sqrt{2}} \exp\left[-\frac{\alpha_p}{2}(t-t_0)^2\right] \exp[i8(t-t_0)]; \quad s(f) = \sqrt{\frac{1}{2\alpha_p^{1/4}}} \exp\left[-(2/\alpha_p)(f-f_0)^2\right] \exp[-i(f-f_0)/8]$$

or, with $\alpha_p = \frac{1}{a^2}$:

$$s(t) = \sqrt{\frac{1}{2a}} \exp\left[-\frac{1}{2}\left(\frac{t-t_0}{a}\right)^2\right] \exp\left[i8\left(\frac{t-t_0}{a}\right)\right]; \quad s(f) = \sqrt{\frac{a}{2}} \exp\left[-2(a(f-f_0))^2\right] \exp[-ia(f-f_0)/8]$$

All of the Constant Q Orthogonal Weber Function Wavelets, which include the above as the 0'th order wavelet are:

$$2^{-n/2} H_n\left(\frac{(t-t_0)}{\sqrt{2}}\right) \exp\left[\frac{-\left(\frac{t-t_0}{a}\right)^2}{4}\right] \exp\left[i(4/(2(n+1)))\left(\frac{t-t_0}{a}\right)\right], \quad n = 0, 1, 2, 3, \dots$$

Integration showed that these continuous wavelets are reasonably well compactly supported.

10.1 Applications

Fig. 10.3 shows the test signals. The first is a frequency hopping signal with a pulse; the second is a representative radar return. Figs 10.4 and 10.5 show the application of the Constant Q Orthogonal Weber Function Wavelets (CQOW) to the two test signals for the 0'th order through the 6th order and at two scale dilations. It can be seen that CQOWs provide excellent detection of both signal frequencies and pulse scattering.

A new form of analysis was tried using the results of the normalized CQOW coefficients. Scatterograms were calculated (Figs 10.6 and 10.7) for the two test signals by parametrically plotting the coefficients for the 0'th order, 1st dilation or 01, the 1st order, 1st dilation or 11, and the 2nd order, 1st dilation or 21, i.e., 01,11,21, then the 0'th order, 2nd dilation or 02, the 1st order, 2nd dilation, or 12, and the 2nd order, 2nd dilation, or 22, i.e., 02,12,22. These parametric plots were carried out among the orders 0'th through 6th and for 2 scale dilations.

In the case of the frequency hopping signal, plus a pulse, Fig. 10.6, it can be seen that discernible cyclic patterns occur which may be correlated with the number of frequencies in the signal - four. In the case of the radar return test signal, Fig. 10.7, it can be seen that recognizable helical patterns occur, which may provide a unique signature for targets.

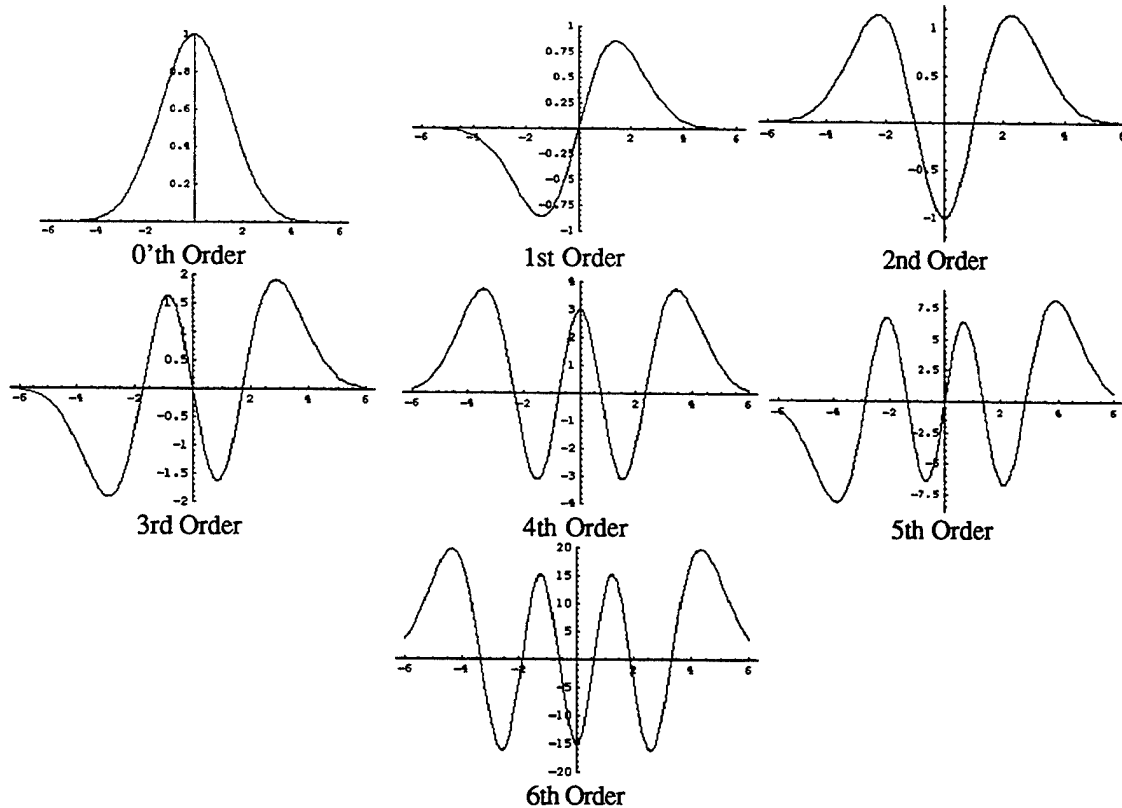


Fig. 10.1. Weber functions, 0'th to 6'th order.

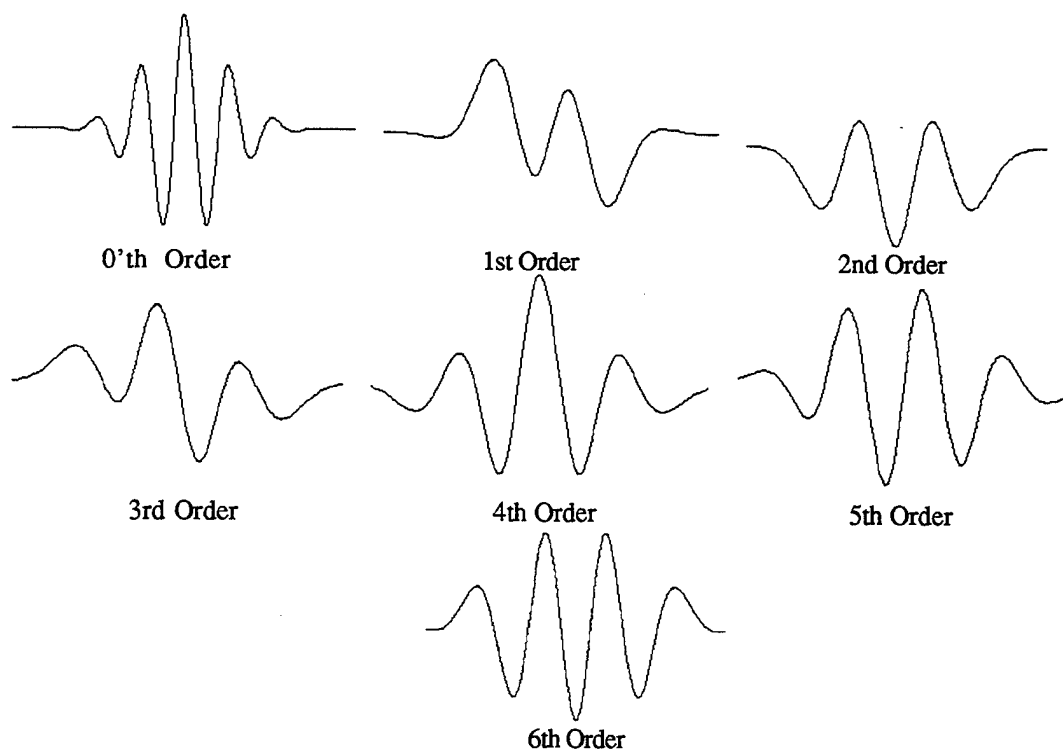


Fig. 10.2. Wavelets based on Weber functions, 0'th to 6'th order.

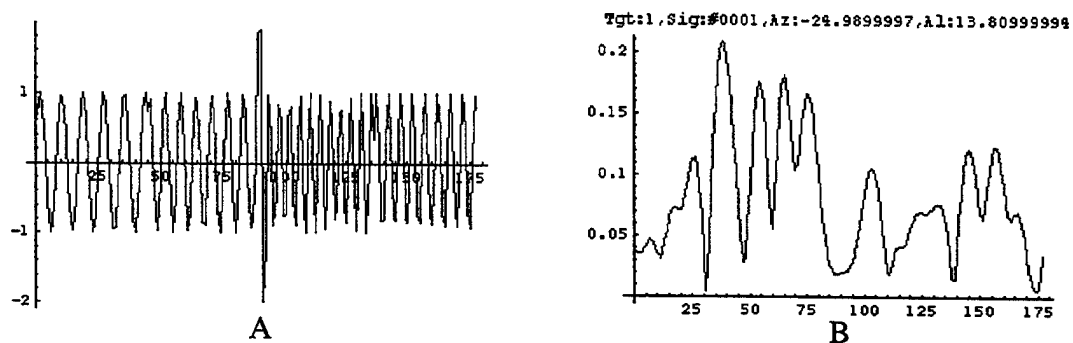
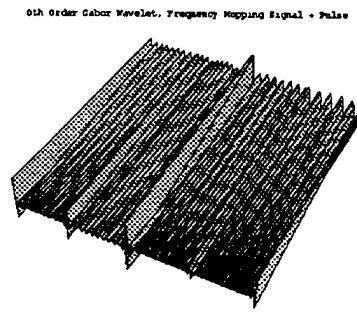
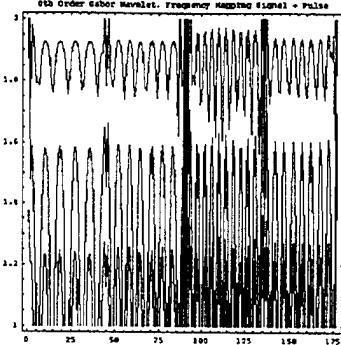
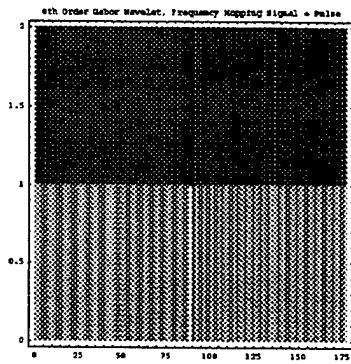
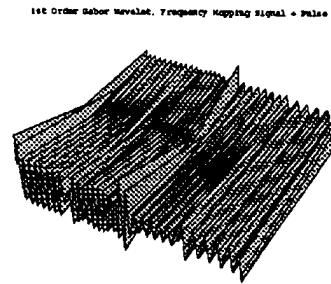
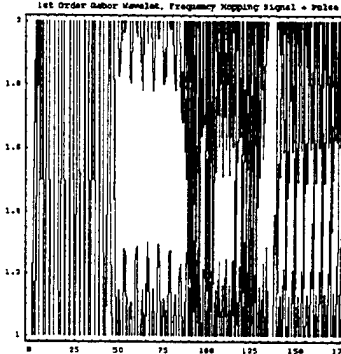
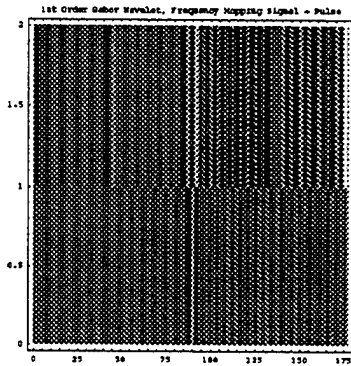


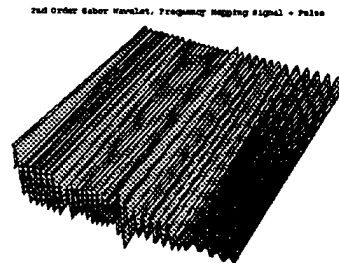
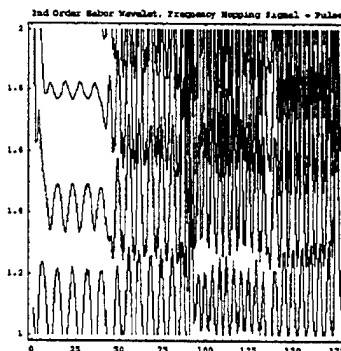
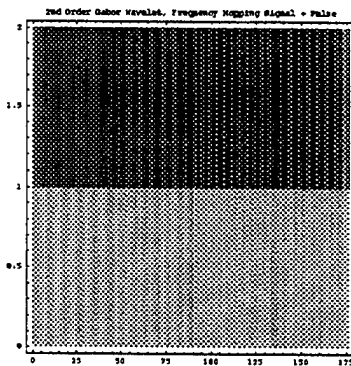
Fig. 10.3. A. Frequency Hopping plus Pulse Test Signal. B. Radar Return Test Signal.



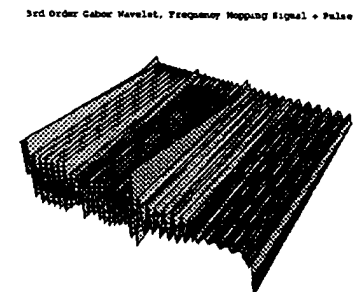
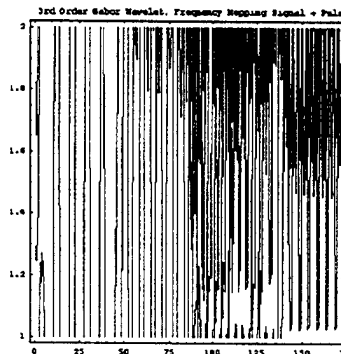
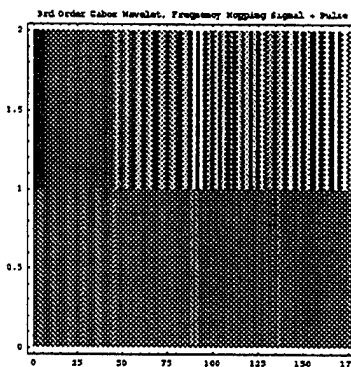
0th Order, 1 and 2.



1st Order, 1 and 2.



2nd Order, 1 and 2.



3rd Order, 1 and 2

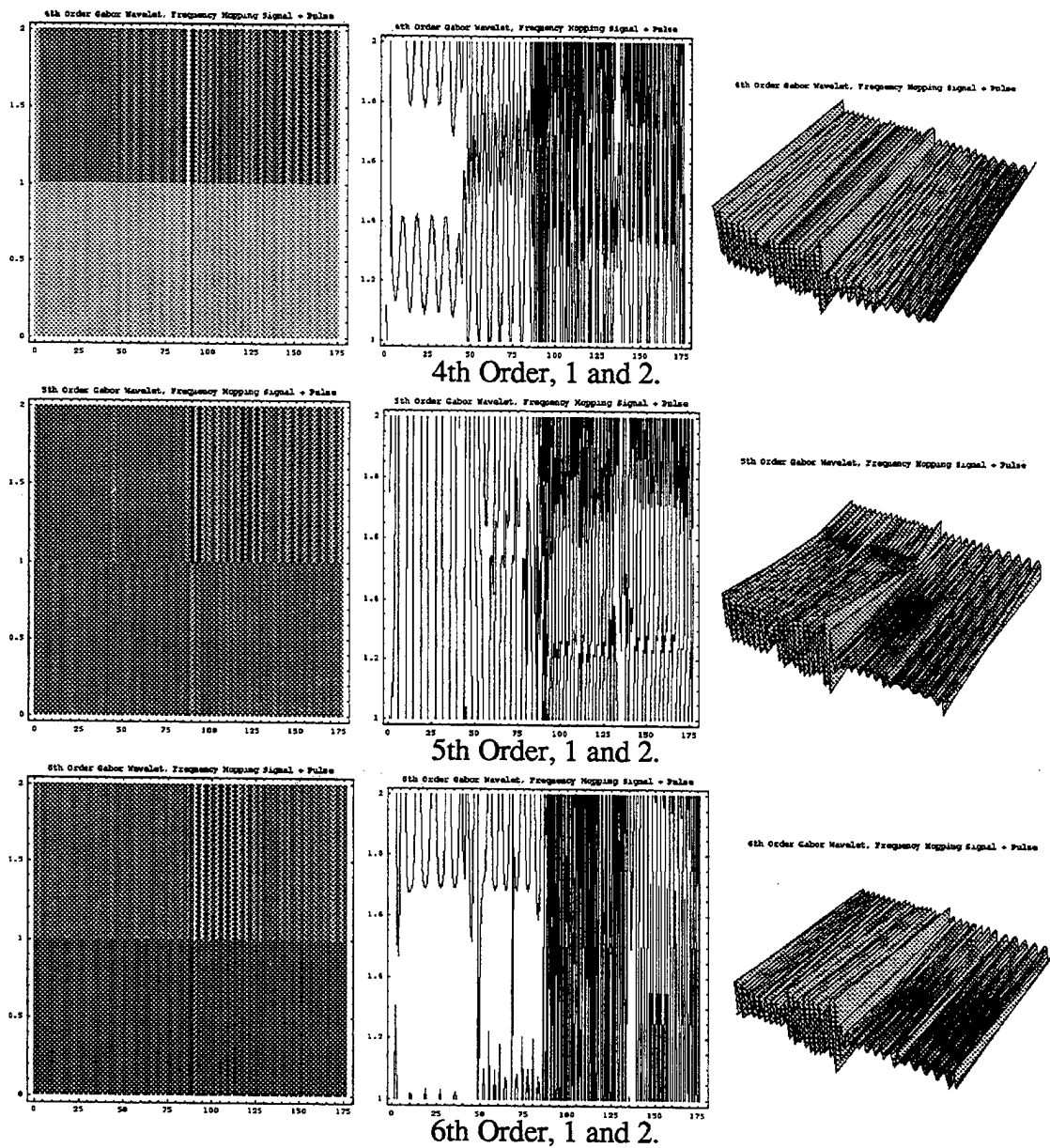
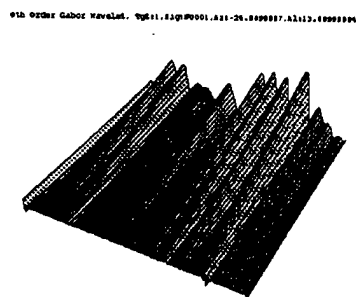
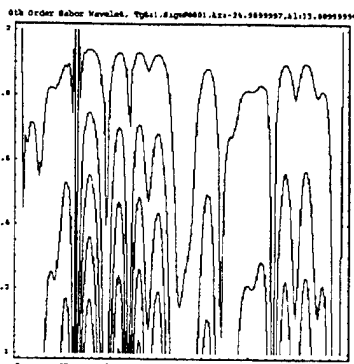
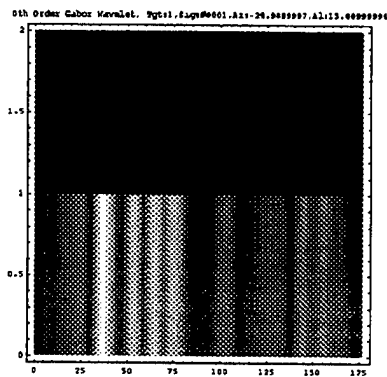
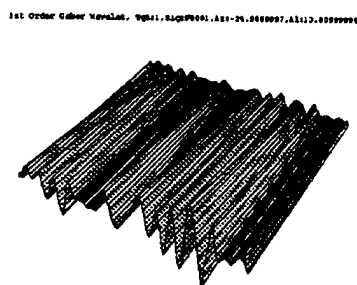
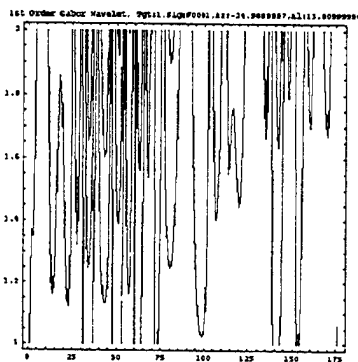
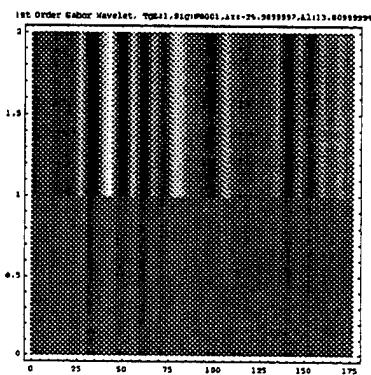


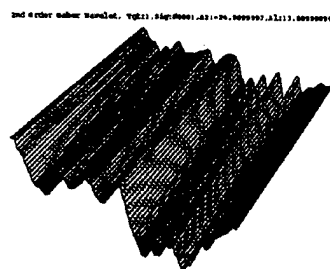
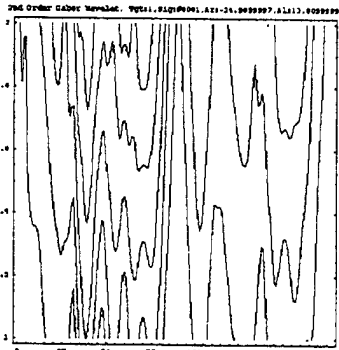
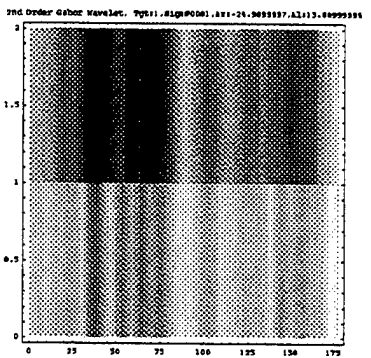
Fig. 10.4. Test Signal: Frequency Hopping with Pulse. Weber function wavelet analysis, 0th to 6th Order, Dilation Filters 1 and 2.



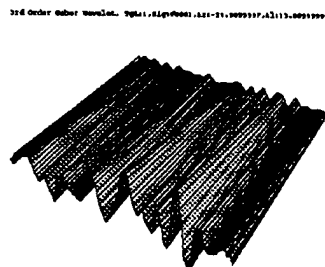
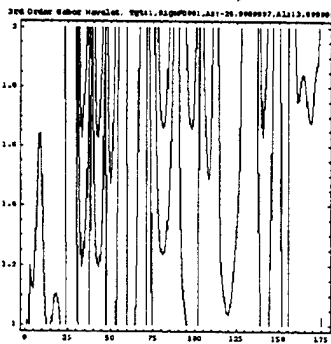
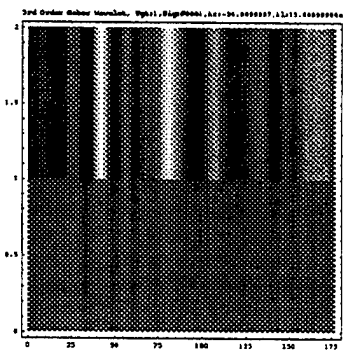
0th Order, 1 and 2.



1st Order, 1 and 2.



2nd Order, 1 and 2.



3rd Order, 1 and 2.

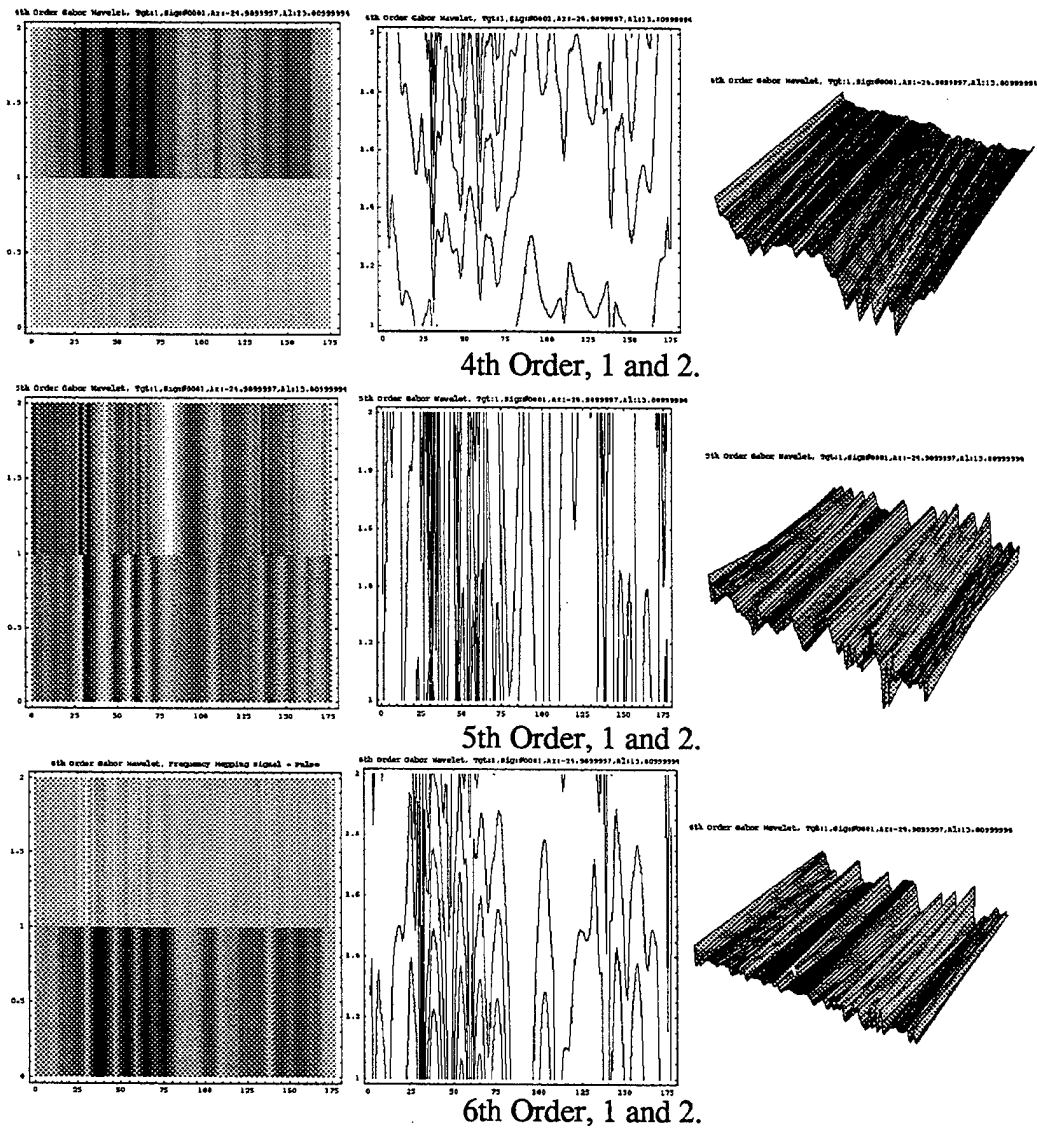
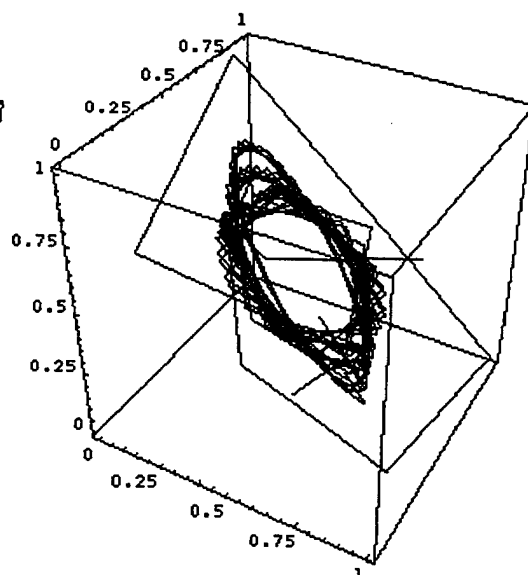
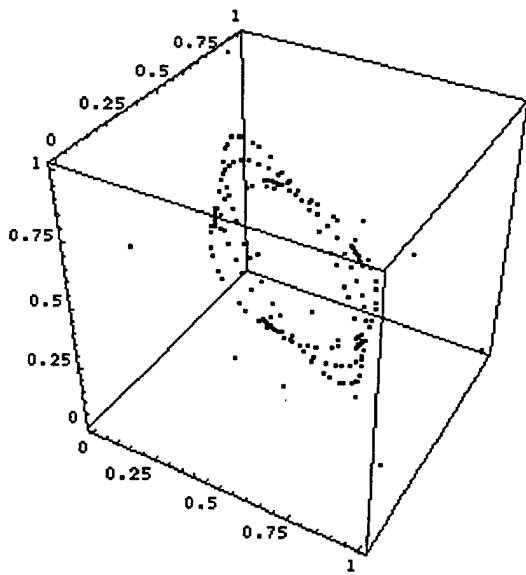
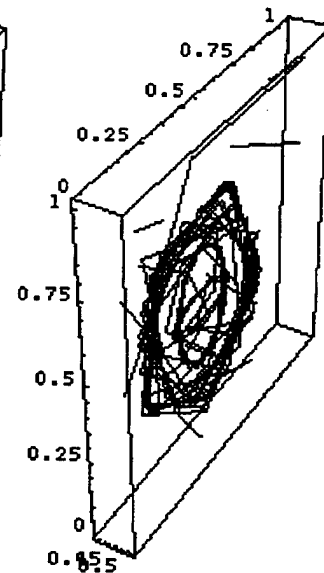
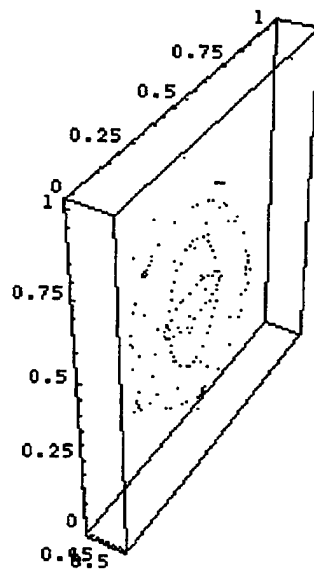


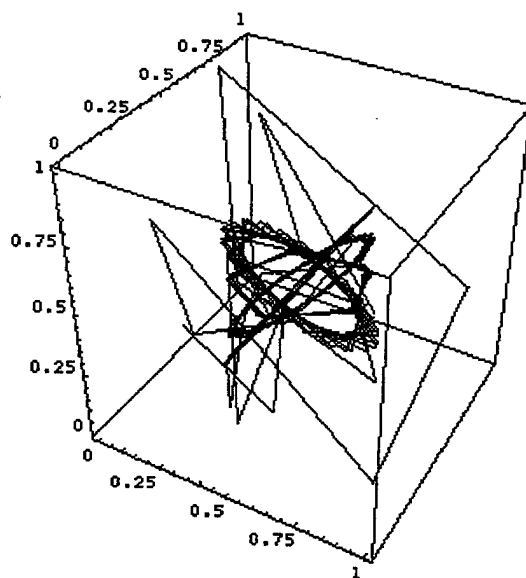
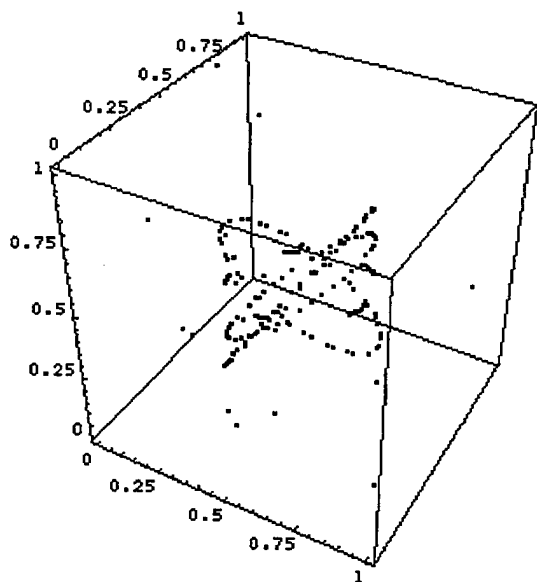
Fig. 10.5. Test Signal: Radar Signal Return. Weber function wavelet analysis, 0th to 6th Order, Filters 1 and 2.



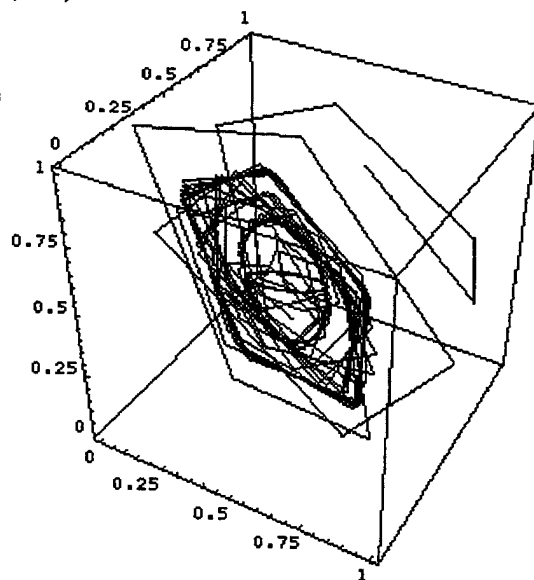
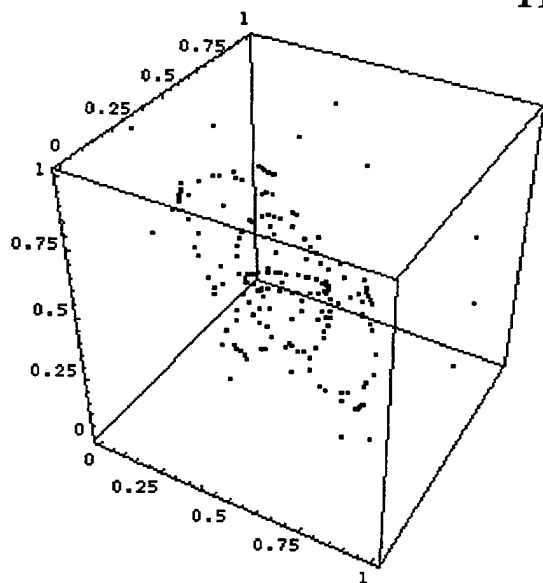
01,11,21



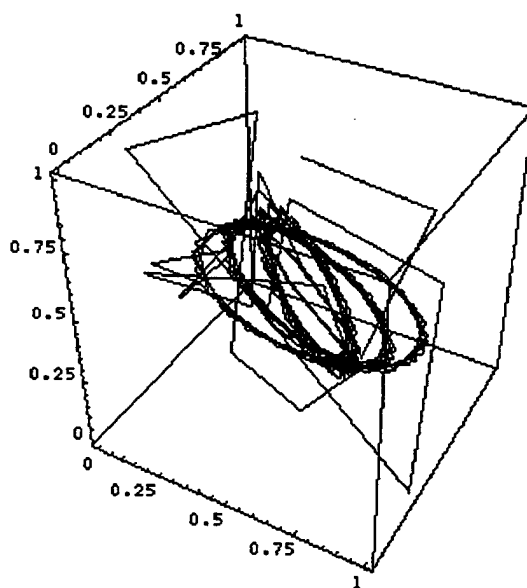
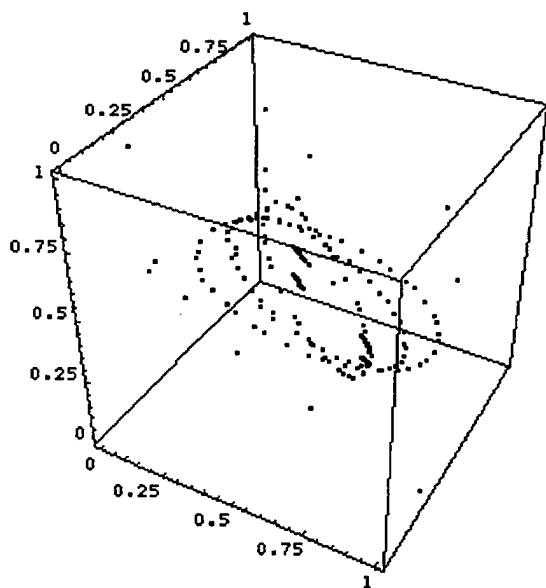
02,12,22



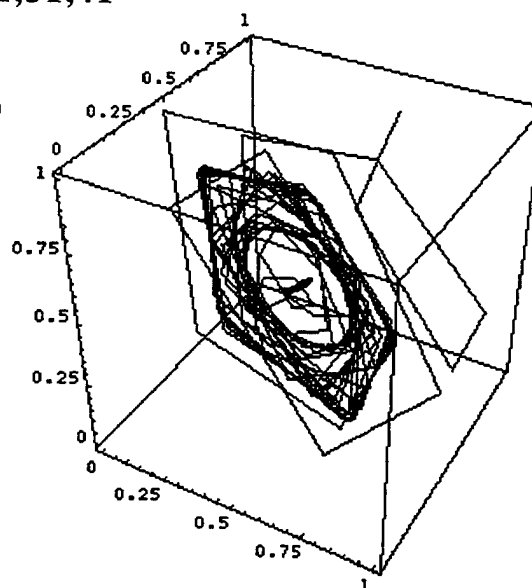
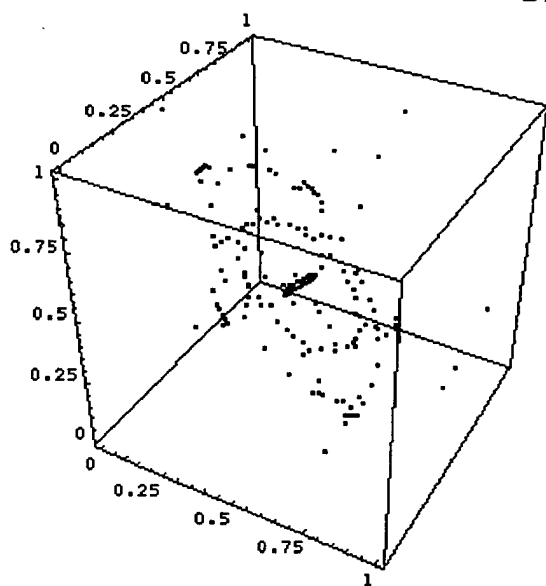
11,21,31



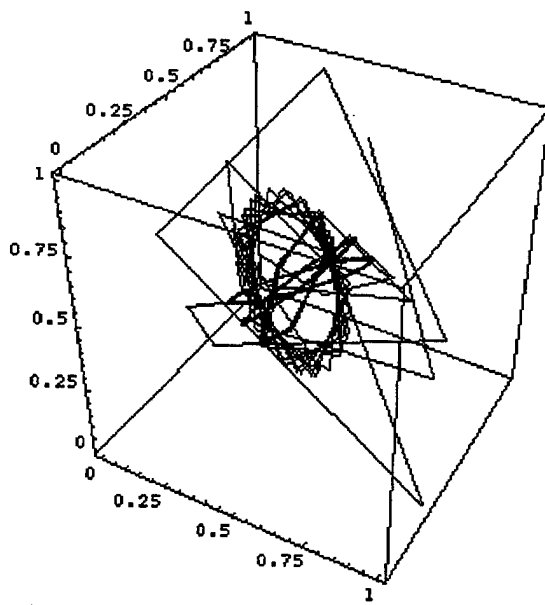
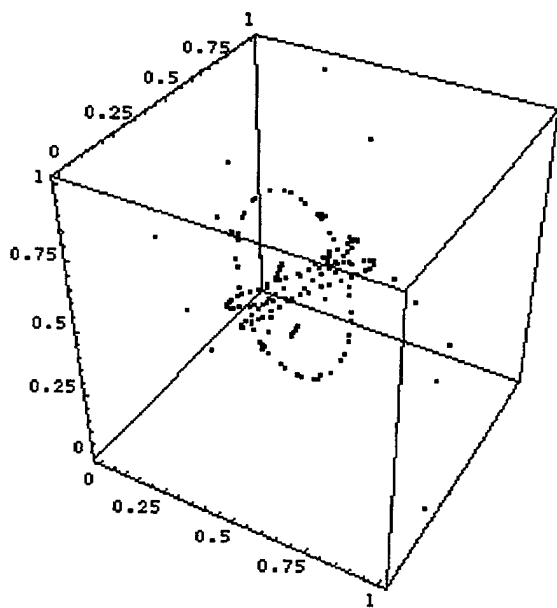
12,22,32



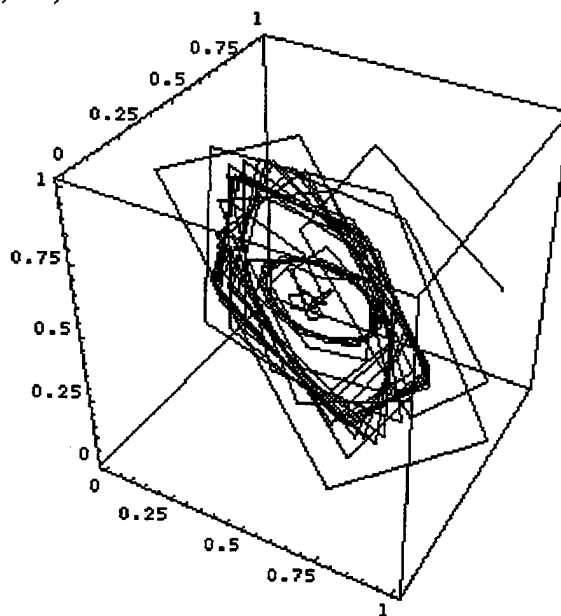
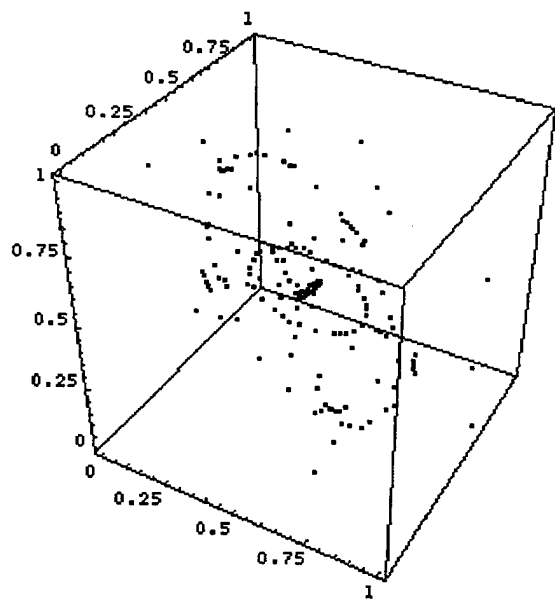
21,31,41



22,32,42



31,41,51



32,42,52

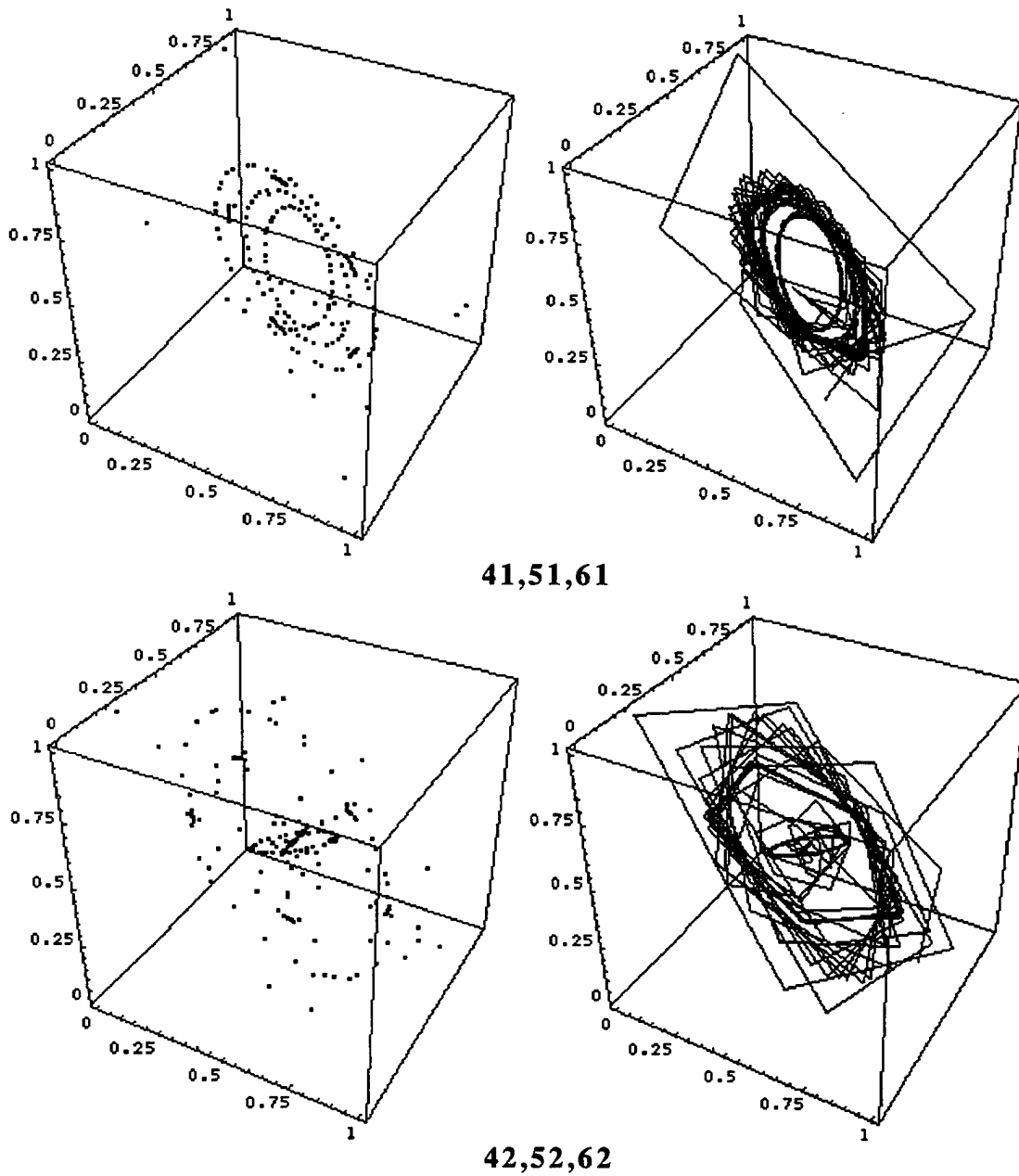
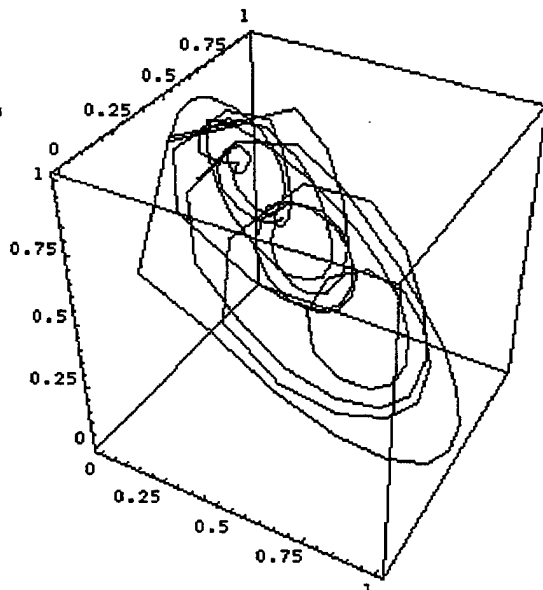
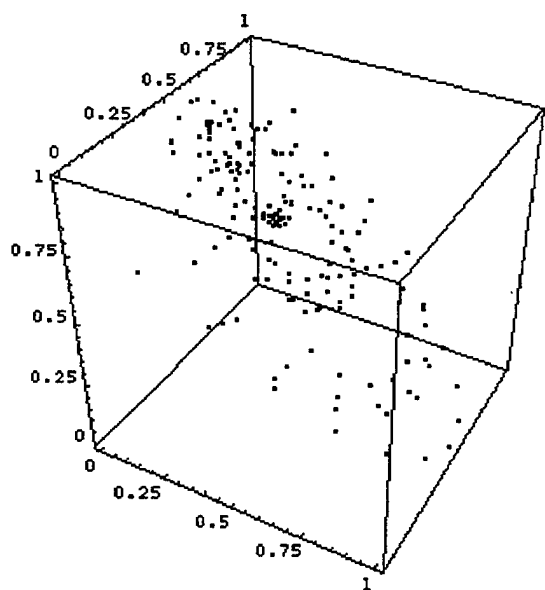
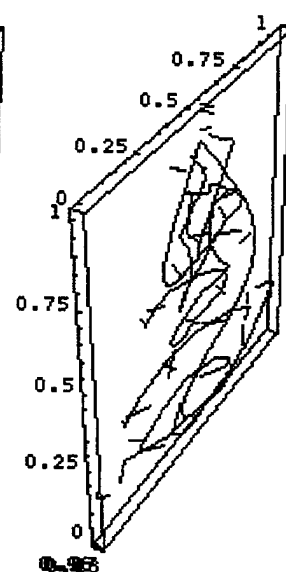
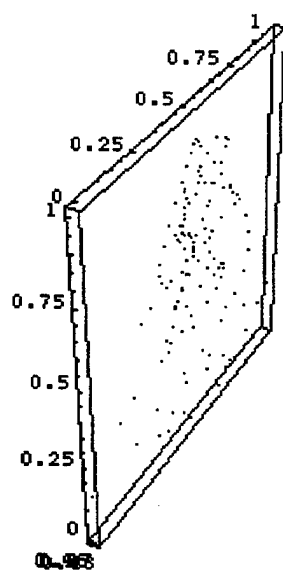


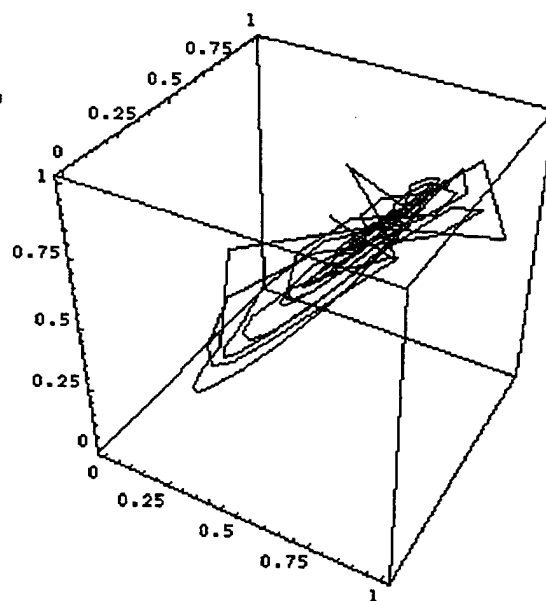
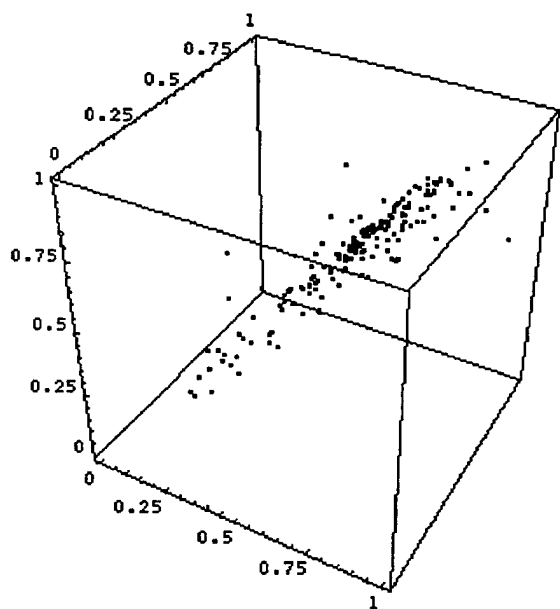
Fig. 10.6. Parametric plots of 0th Order, 1st Order, 2nd Order, 1st Filters (01,11,21), 2nd Filters (02,12,22), etc. ... (42,52,62) for the Test Signal, Frequency Hopping plus Pulse.



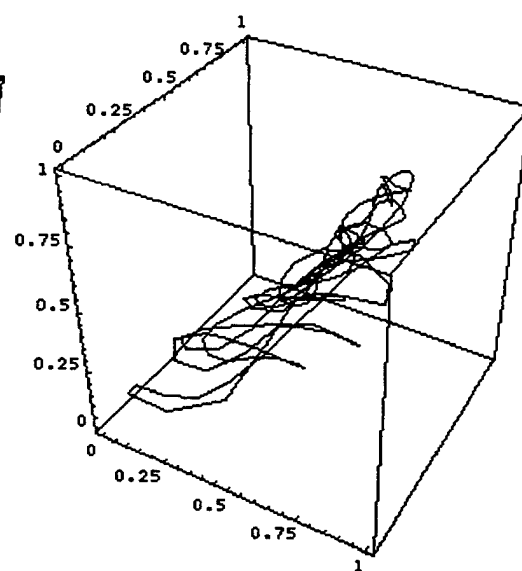
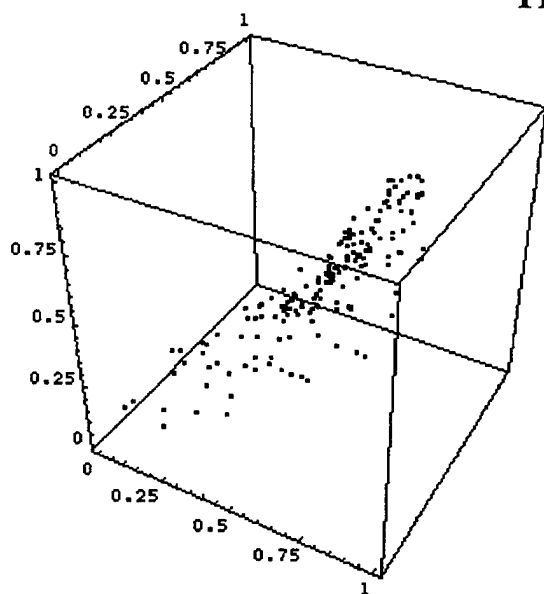
01,11,21



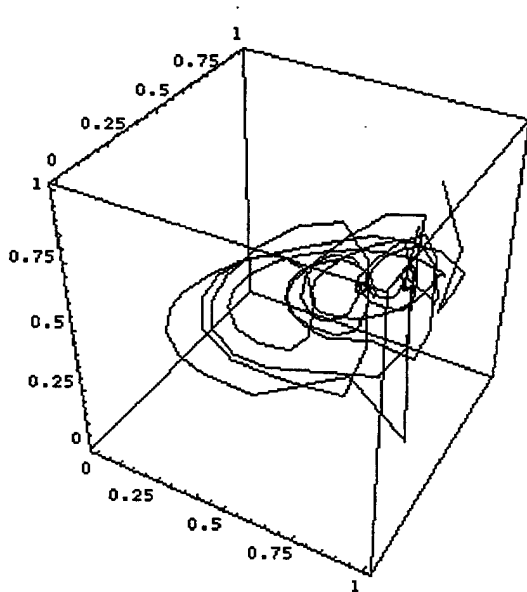
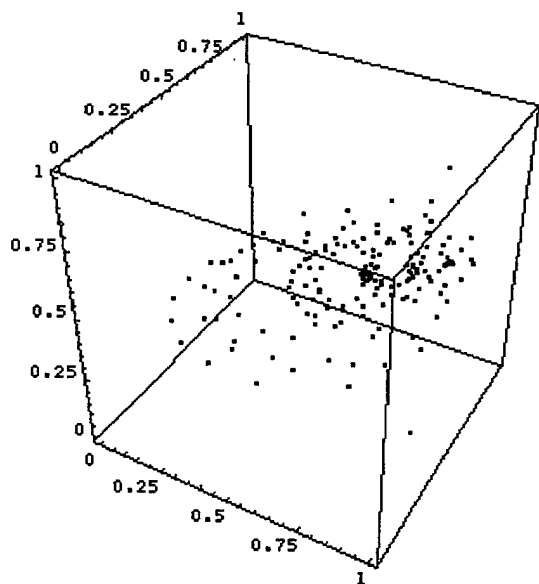
02,12,22



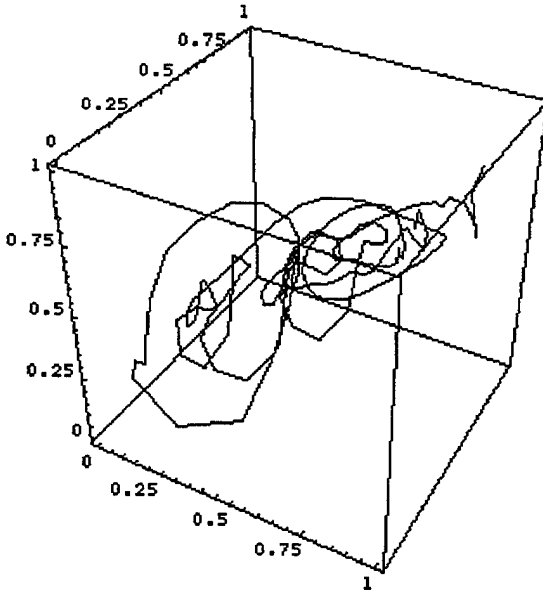
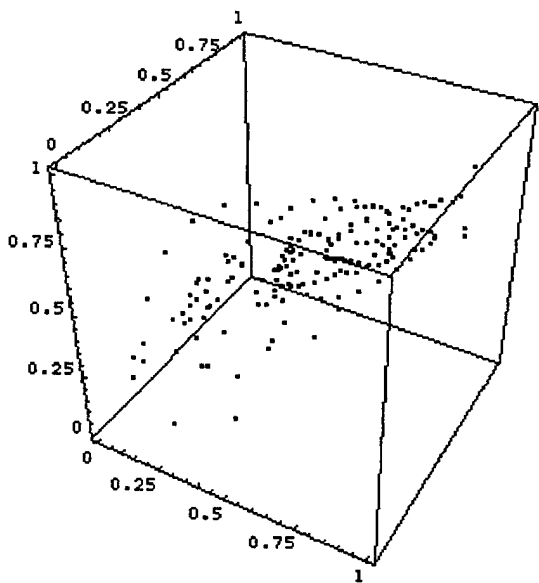
11,21,31



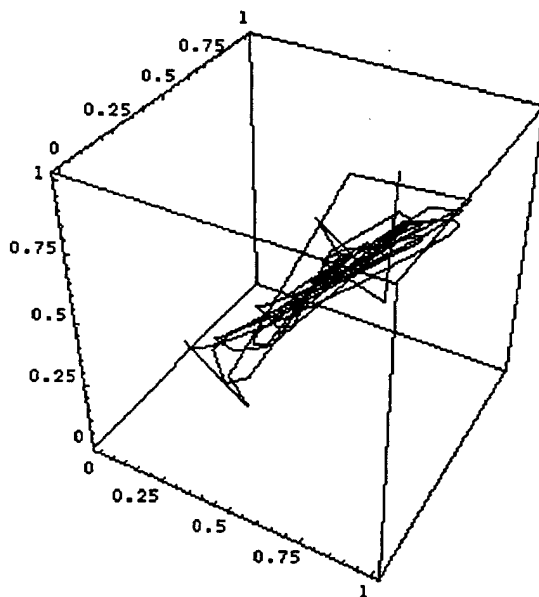
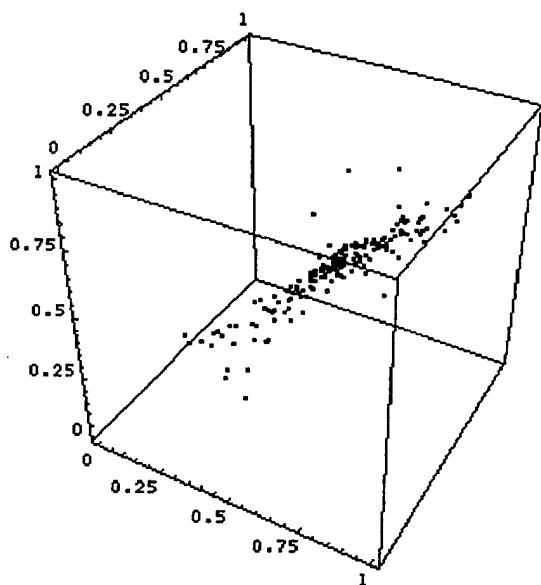
12,22,32



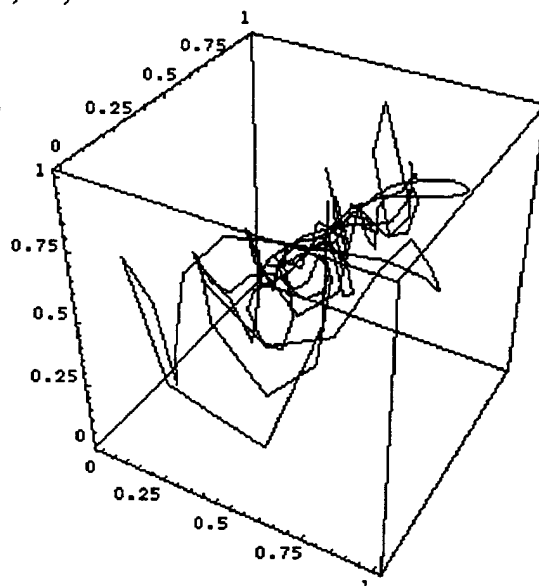
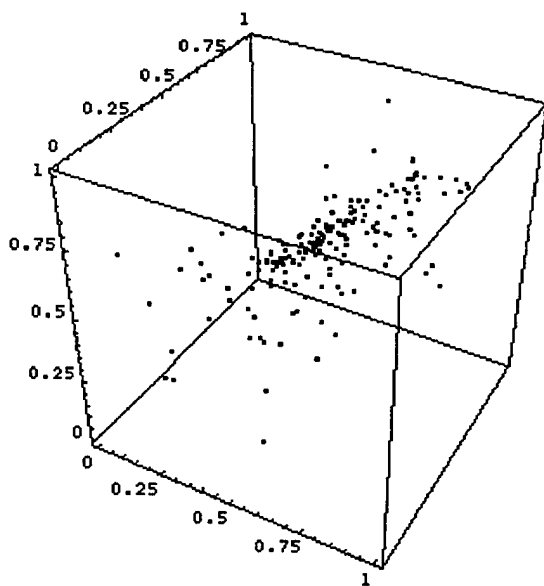
21,31,41



22,32,42



31,41,51



32,42,52

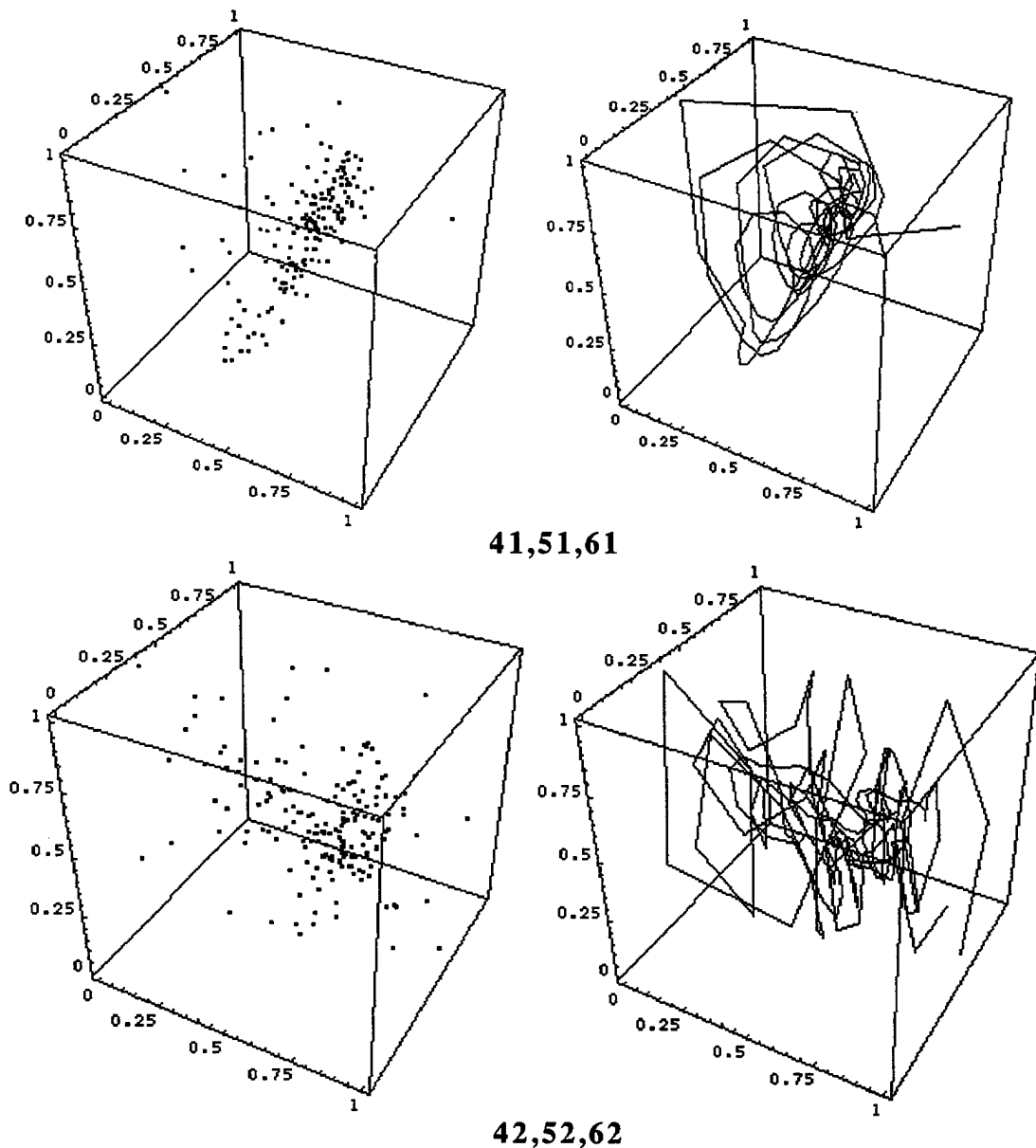


Fig. 10.7. Parametric plots of 0th Order, 1st Order, 2nd Order, 1st Filters (01,11,21), 2nd Filters (02,12,22), etc. ... (42,52,62) for the Test Signal, Radar Return Signal.

10.2 Paraunitary Properties

Using a frequency hopping and pulse test signals, CQOWs wavelets are able to detect both resonance and pulse scattering features. The characteristics of these wavelets are based on IIF filter principles. It is customary to believe that a discrete time scaling (low pass) wavelet is first necessary to obtain the discrete time (high pass) wavelet. Here we show that the expansion method permits an estimate of the continuous time high pass wavelet from the summed Fourier spectra of the expansions, $n = 1, 2, \dots \infty$. Future work will examine whether repeated analysis of the original signal by higher order wavelets is equivalent to the customary method of using but one scaling function and one wavelet with signal decimation.

Paraunitary properties underlie not only the perfect reconstruction capabilities of certain wavelets but the relation of the low pass (scaling) and high pass (wavelet) filters. These properties are defined as follows³. Some definitions are necessary, which are:

If $H(z)$ is the z -transform of $h(n)$, then

$$H(z) = \sum_{n=-\infty}^{\infty} h(n)z^{-n}$$

If $z = \exp[i\omega]$, then $H(z)$ is the Fourier transform of $h(n)$.

$$\tilde{H}(z) = [H(z)]^*,$$

that is, $\tilde{H}(z)$ is the paraconjugate of $H(z)$.

$H^*(x)$ is the complex conjugate of $H(x)$ and $H_*(x)$ indicates that only the coefficients are conjugated.

$H^\dagger(x)$ denotes the transpose-conjugate of $H(x)$.

Using the above, if $\tilde{H}(z)H(z) = d\mathbf{I}$, for some $d > 0$ and for all z ,

then the filter has the paraunitary property. Furthermore, if $\mathbf{E}(z)$ is a filter analysis bank, and $\mathbf{R}(z)$ is a filter synthesis bank, then the perfect reconstruction property is expressed by:

$$\mathbf{R}(z) = cz^{-K}\tilde{\mathbf{E}}(z).$$

Under the paraunitary condition, the analysis filters are then related as:

$$h_1(n) = -c(-1)^n h_0^*(L - n),$$

from which relation has arisen the customary observation that the discrete time high pass filter must be obtained from the discrete time low pass filter and that knowing the continuous time low pass filter does not permit the definition of the high pass filter - continuous or discrete time.

10.3 Applications

Here we obtain the high pass filter in another way. The Fourier transforms of a number of Weber functions are shown in Fig. 10.3.1. With the $n = 0$ function as the scaling wavelet (the first shown in Fig. 10.3.1) then the higher order functions can be viewed as approximations to the high pass wavelet. Thus the high pass wavelet can be obtained by the inverse transform of the summation of the Fourier spectra of the series above $n = 0$. Fig. 10.3.2A shows that summation for the small number of the series shown in Fig. 10.3.1. Fig. 10.3.2B. shows the limiting extrapolation.

³ Cf. Vaidyanathan, P.P. *Multirate Systems and Filter Banks*, Prentice Hall, 1993; Vetterli, M. & Kovacevic, *Wavelets and Subband Coding*, Prentice Hall, 1995.

The inverse transform of Fig. 10.3.2B provides the high pass wavelet which is shown in Fig. 3B (with the scaling function shown in Fig. 10.3.3A for cross comparison). The low pass scaling function and the high pass wavelet were then used to analyze the frequency hopping signal plus pulse shown in Fig. 10.3.4. Figs 10.3.5 and 10.3.6 provides the results. It can be seen that the low pass and high pass features are adequately displayed. It is straightforward to use this scaling function and this wavelet in a multiscale analysis, utilizing the customary decimation procedures.

Alternatively, the signal can be analyzed, without decimation, by utilizing the Weber functions wavelet series, $n = 0, 1, 2, 3, 4, 5, 6$, in a Gram-Schmidt-like expansion. Future work will examine the advantages of this approach.

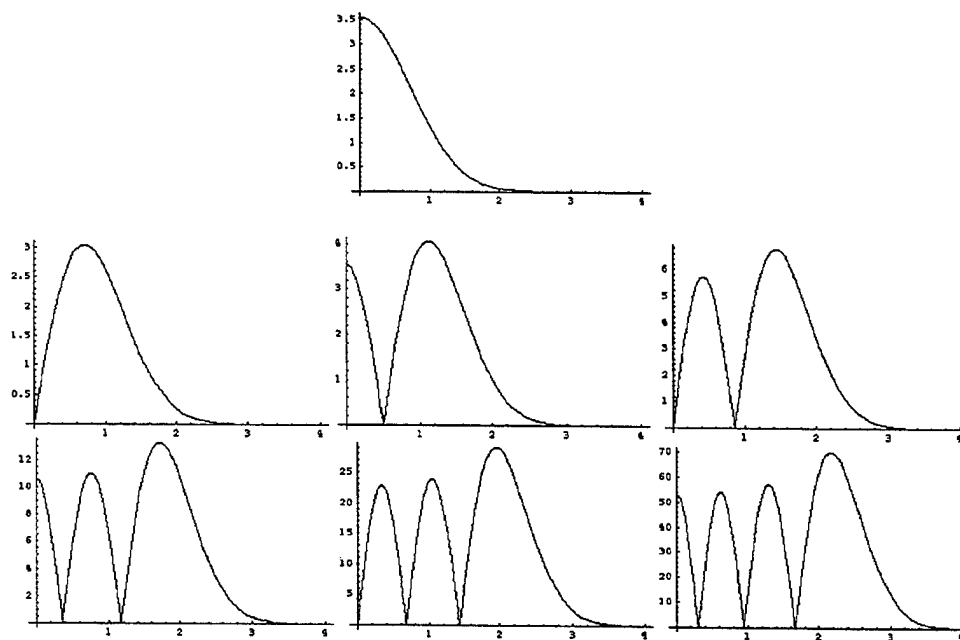


Fig. 10.3.1. Fourier transforms of Weber functions (elementary signals) for $n = 0, 1, 2, 3, 4, 5$ and 6 .

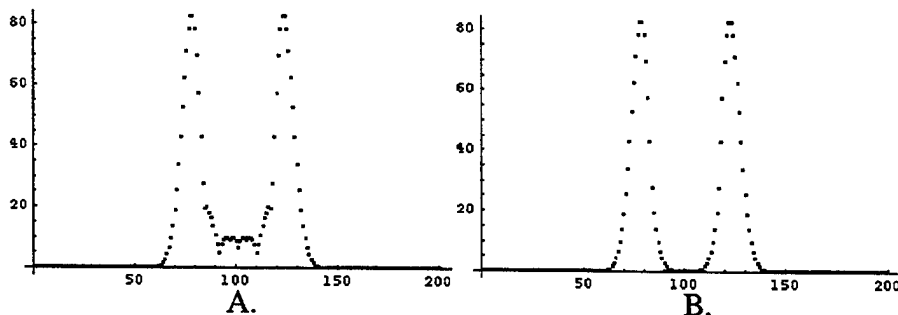


Fig. 10.3.2. A. The additive Fourier transforms of the Weber functions for $n = 1, 2, 3, 4, 5$ and 6 . B: The projected additive Fourier transform of the Weber functions for $n = 1 \dots \rightarrow \infty$.

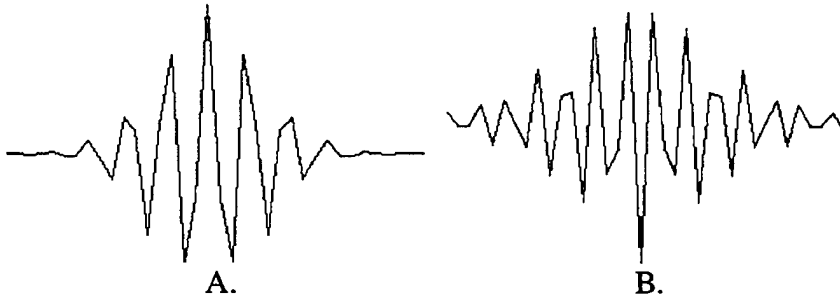


Fig. 10.3.3. A: The scaling (low pass) Weber function. B: the (high pass) wavelet from the inverse Fourier transform of the Fourier spectra of Fig. 2B.

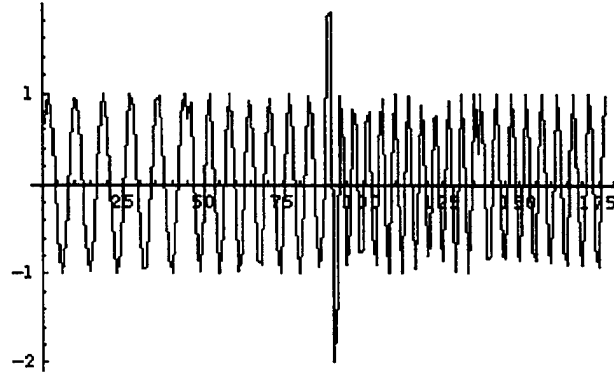


Fig. 10.3.4. Representative frequency hopping signal plus pulse.

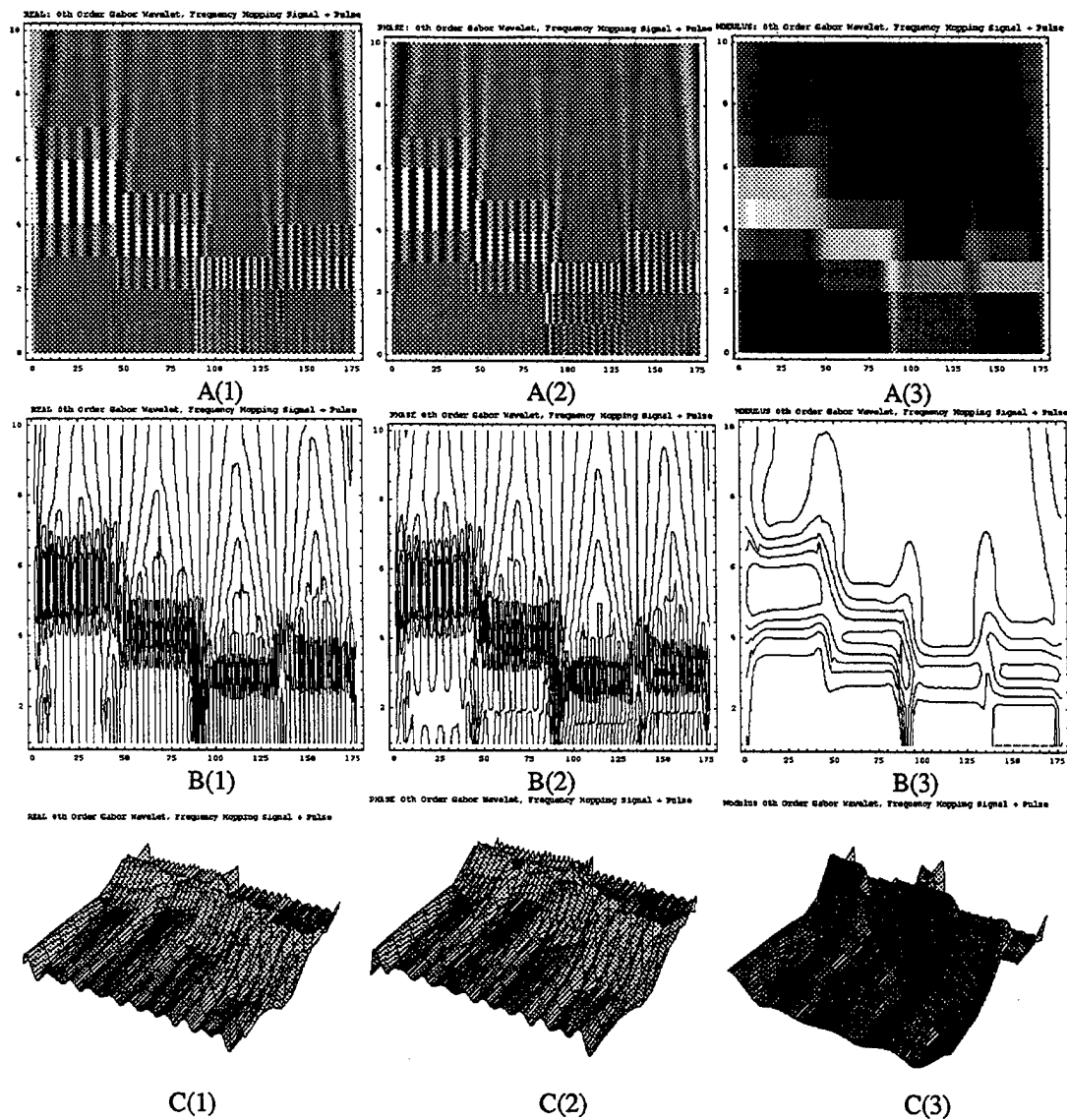


Fig. 10.3.5. Wavelet transform of the frequency hopping signal plus pulse shown in Fig. 4, using the low pass Weber function wavelet shown in Fig. 10.3.3A. A(1)-B(1)-C(1), A(2)-B(2)-C(2), A(3)-B(3)-C(3), show the real part, the phase and modulus of the wavelet transform.

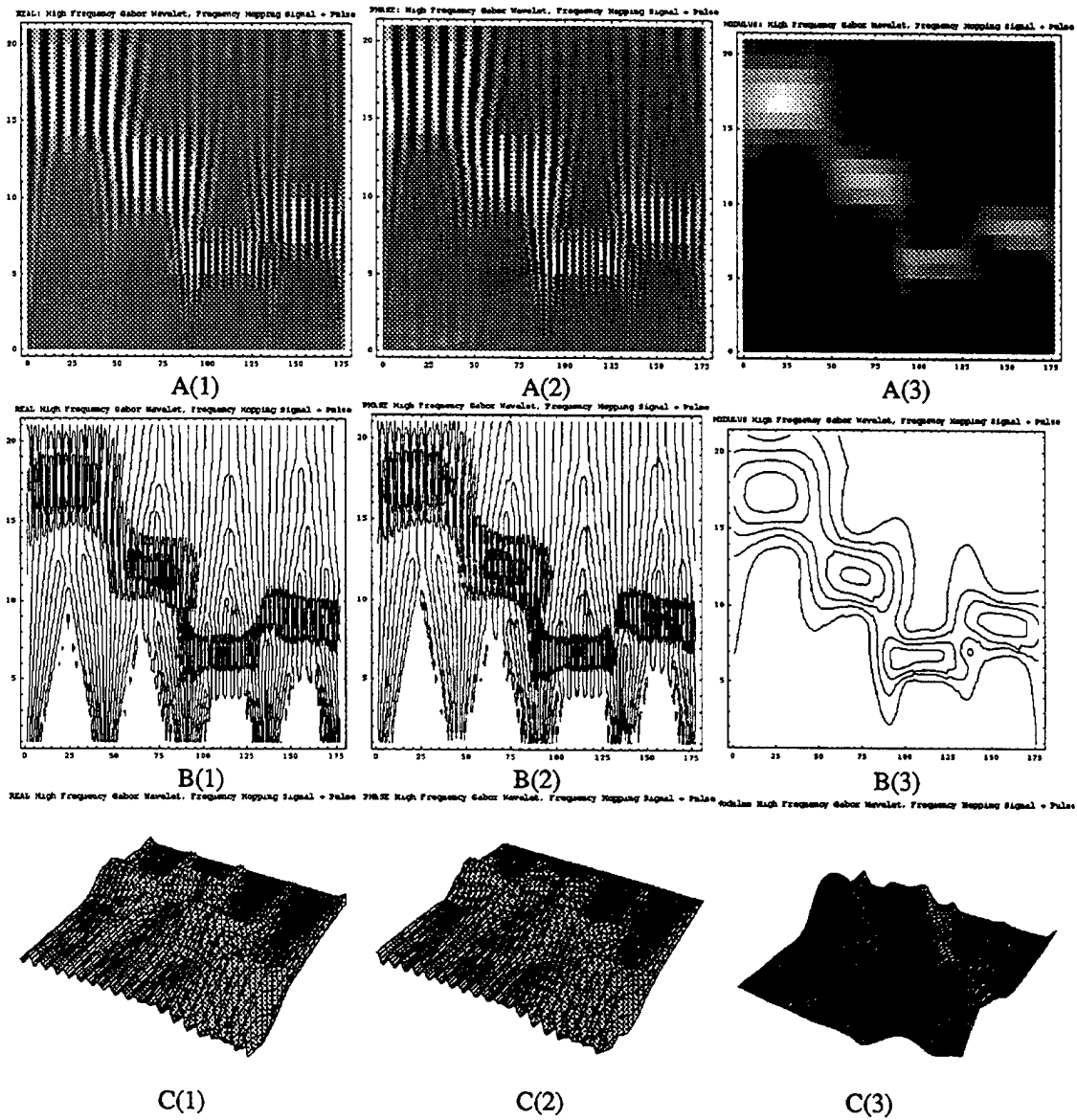


Fig. 10.3.6. Wavelet transform of the frequency hopping signal plus pulse shown in Fig. 10.3.4, using the high pass Weber function wavelet shown in Fig. 10.3.3B. A(1)-B(1)-C(1), A(2)-B(2)-C(2), A(3)-B(3)-C(3), show the real part, the phase and modulus of the wavelet transform.

11.0 Instantaneous Phase

This section addresses instantaneous phase information obtainable from application of wavelet analysis. We show that a detailed thumbprint of a complex (target return) signal can be obtained which can be used as data supporting a detailed wavelet modulus description of the same signal. We also show a result from calculating the differential phase which also provides supporting data. It is also shown that there are optimum dilations for providing correlated measures.

We also calculated the probability distribution function for the target return signal processed with a specific dilation of the wavelet and the mutual information for two dilations. This form of analysis also provides supporting data to the modulus thumbprint of the signal.

In summary, the phase information and mutual information provide excellent supporting data to that providing by the wavelet modulus. In combination a more detailed analysis of target information is possible.

1. Instantaneous Phase

The Weber functions are defined as extensions of the Gabor transform with the four signal variables of center frequency, f_0 , midperiod, t_0 , frequency bandwidth Δf and time bandwidth, Δt , are separately defined. For example,

$$\Delta f = \sqrt{\frac{1}{2} \left(\frac{\alpha_p}{1} \right)},$$

$$\Delta t = \sqrt{\frac{1}{2} \left(\frac{1}{\alpha_p} \right)},$$

with

$$f_0 = \text{mid } \Delta f,$$

$$t_0 = \text{mid } \Delta t.$$

Obviously, this does not provide a constant Q wavelet.

However, a constant Q Gabor wavelet is achieved from the following definitions¹:

$$f_0 = \sqrt{8\alpha_p},$$

$$t_0 = \sqrt{\frac{1}{32} \frac{1}{\alpha_p}},$$

$$\Delta f = \sqrt{\frac{1}{2} \frac{\alpha_p}{1}},$$

$$\Delta t = \sqrt{\frac{1}{2} \frac{1}{\alpha_p}}.$$

¹ Barrett, T.W., Structural information theory. *J. Acoust. Soc. Am.*, 54, 1092-1098, 1973.

The constant Q Gabor wavelet thus conforms to the following condition:

$$f_0 \cdot t_0 = \Delta f \cdot \Delta t = \frac{1}{2},$$

A more general condition has been derived²:

$$f_0 \cdot t_0 = \Delta f \cdot \Delta t = \frac{1}{2}(2n+1) \quad n = 0, 1, 2, \dots$$

which provides a range of orthogonal wavelets.

Specifically, these wavelets are based on modulations which are Weber's functions. Weber's equation is:

$$\frac{d^2 D}{dt^2} + (\lambda - \xi^2) D = 0,$$

where ξ is a dimensionless independent variable and λ is a dimensionless eigenvalue. The solutions to Weber's equation are the parabolic cylinder or Weber-Hermite functions:

$$D_n(t) = 2^{-n/2} H_n\left(\frac{t}{\sqrt{2}}\right) \exp\left[\frac{-t^2}{4}\right],$$

where

$$H_n(t) = (-1)^n \exp[t^2] \frac{\partial^n \exp[-t^2]}{\partial t^n}$$

are Hermite polynomials satisfying:

$$\frac{d^2 x}{dt^2} - 2t \frac{dx}{dt} - 2nx = 0$$

-
- ² Barrett, T.W., On vibrating strings and information theory. *J. Sound & Vibration*, 20, 407-412, 1972a.
 _____, Conservation of information. *Acustica*, 27, 44-47, 1972b.
 _____, The definition precedence of signal parameters: sequential versus simultaneous information. *Acustica*, 27, 90-93, 1972c.
 _____, The conceptual basis of two information theories - a reply to some criticisms. *J. Sound & Vibration*, 25, 638-642, 1972d.
 _____, Analytical information theory. *Acustica*, 29, 65-67, 1973.
 _____, Nonlinear analysis and structural information theory: a comparison of mathematical and physical derivations. *Acustica*, 33, 149-165, 1975.
 _____, On linearizing nonlinear systems. *J. Sound & Vibration*, 39, 265-268, 1975.
 _____, Linearity in secular systems: four parameter superposition. *J. Sound & Vibration*, 41, 259-261, 1975.
 _____, Information measurement I. On Maximum entropy conditions applied to elementary signals. *Acustica*, 35, 80-85, 1975.
 _____, Information measurement II. On minimum conditions of energy order applied to elementary signals. *Acustica*, 36, 282-286, 1975.
 _____, Structural information theory of sound. *Acustica*, 36, 271-281, 1976.

and the orthogonality relationship:

$$\int_{-\infty}^{+\infty} H_m(t) H_n(t) \exp[-t^2] dt = 0 \text{ for } m \neq n.$$

The following analysis is based on the 0'th order ($n = 0$) wavelet:

$$\psi(t) = 2^{-0/2} H_0\left(\frac{t}{\sqrt{2}}\right) \exp\left[\frac{-t^2}{4}\right].$$

The signal analyzed is the frequency hopping plus pulse signal shown in Fig. 1.

The wavelet can be viewed as an analytic signal:

$$\psi(t) = s(t) + i\hat{s}(t),$$

where $\hat{s}(t)$ is the Hilbert transform of $s(t)$:

$$\hat{s}(t) = \frac{1}{\pi} P.V. \int_{-\infty}^{+\infty} \frac{s(\tau)}{t - \tau} d\tau,$$

P.V. indicates that the integral is taken in the sense of the Cauchy principal value. The *instantaneous phase* is then defined as:

$$\phi(t) = \arctan \frac{\hat{s}(t)}{s(t)}.$$

The differential of instantaneous phase is represented by means of obtaining the difference in phase between the phases obtained from applying the Gabor wavelet at different dilations.

11.1 Mutual Information.

If the phases of the wavelet filtered signal are considered as n discrete random variables, X_1, \dots, X_n , with sets of values, Ξ_1, \dots, Ξ_n , the probability distribution for an individual phase for a particular time in the signal and using a particular dilation of a Gabor wavelet, X_i , is:

$$p(x_i) = \Pr[X_i = x_i], x_i \in \Xi_i.$$

The joint probability distribution can then be defined for n variables X_1, \dots, X_n as $p(x_1, \dots, x_n)$.

The mutual information, $I(X_1; X_2)$, is defined as:

$$I(X_1; \dots; X_n) = \sum_{x_1 \in \Xi_1} \dots \sum_{x_n \in \Xi_n} p(x_1, \dots, x_n) \log \frac{p(x_1, \dots, x_n)}{p(x_1) \dots p(x_n)}.$$

11.2 Applications

Fig. 11.2 shows the instantaneous phase information from application of the 0th order Gabor wavelet to the signal of Fig. 11.1. It can be seen that a detailed thumbprint of the frequency hopping plus impulse signal can be obtained which could be used as data supporting a detailed wavelet modulus description of the signal. Fig. 11.3 shows the differential phase result which also provides supporting data. Fig. 11.4 is a more detailed single cut analysis of Fig. 11.3 and shows the fine structure correspondence to the frequency components of the signal.

Fig. 11.5 provides 3-dimensional cross-phase plots of the data of Fig. 11.2 and reveals the fine structural changes in phase at increasing dilations of the wavelet. Fig. 11.6 also provides the same information for the differential phase measurements of Fig. 11.3. Figs 11.7 and 11.8 are phase-phase plots for different dilations of the wavelet for the instantaneous and differential phase measurements. It can be seen that there are optimum dilations for providing correlated measures.

Fig. 11.9 shows examples of a probability distribution function for the signal processed with a specific dilation of the wavelet and the mutual information for two dilations; and Fig. 11.10 shows the mutual information from application of the 0th order Gabor wavelet at a number of dilations. This form of analysis also provides supporting data to the modulus thumbprint of the signal.

In summary, the phase information and mutual information provide excellent supporting data to that providing by the wavelet modulus. In combination a more detailed analysis of target information is possible.

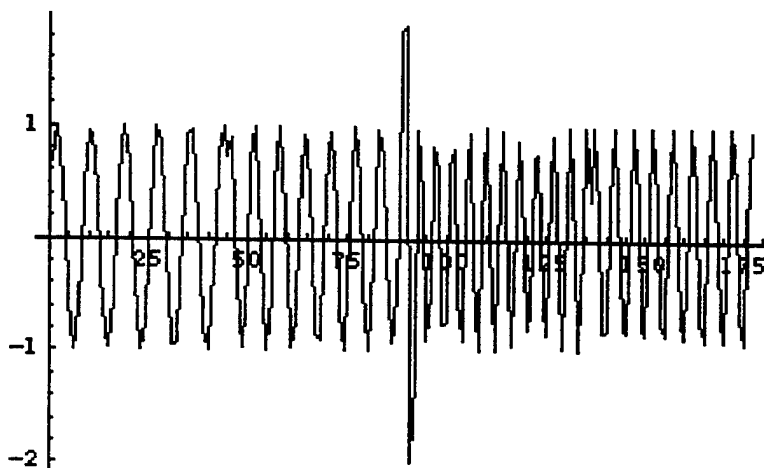
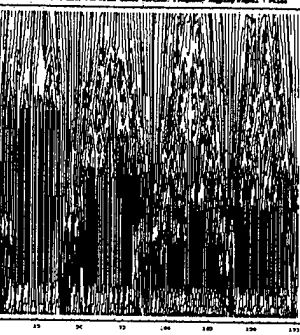
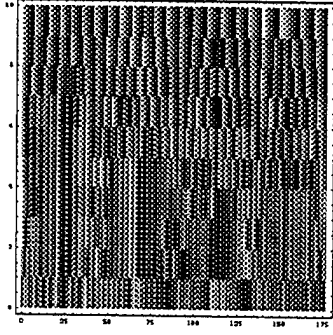


Fig. 11.1. Frequency Hopping plus Pulse representative signal.

Instantaneous Phase, 0th Order Gabor Wavelet, Frequency Hopping signal + Pulse



Instantaneous Phase, 0th Order Gabor Wavelet, Frequency Hopping signal + Pulse

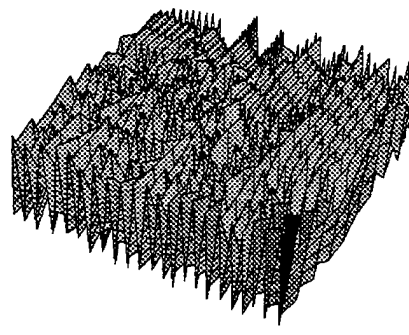
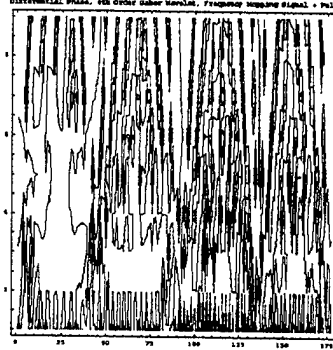
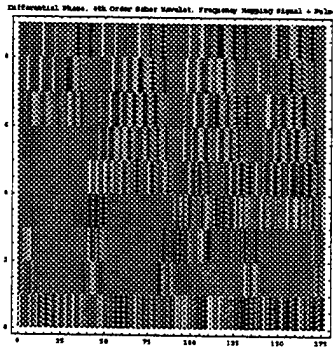


Fig. 11.2. Instantaneous phase measurements of the signal of Fig. 1 using the 0th order Gabor wavelet function.



Differential Phase, 0th Order Gabor Wavelet, Frequency Hopping signal + Pulse

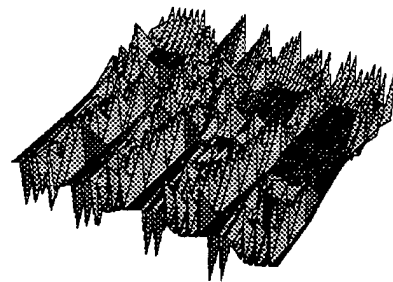


Fig. 11.3. Differential phase measurements of the signal of Fig. 11.1 using the 0th order Gabor wavelet function.

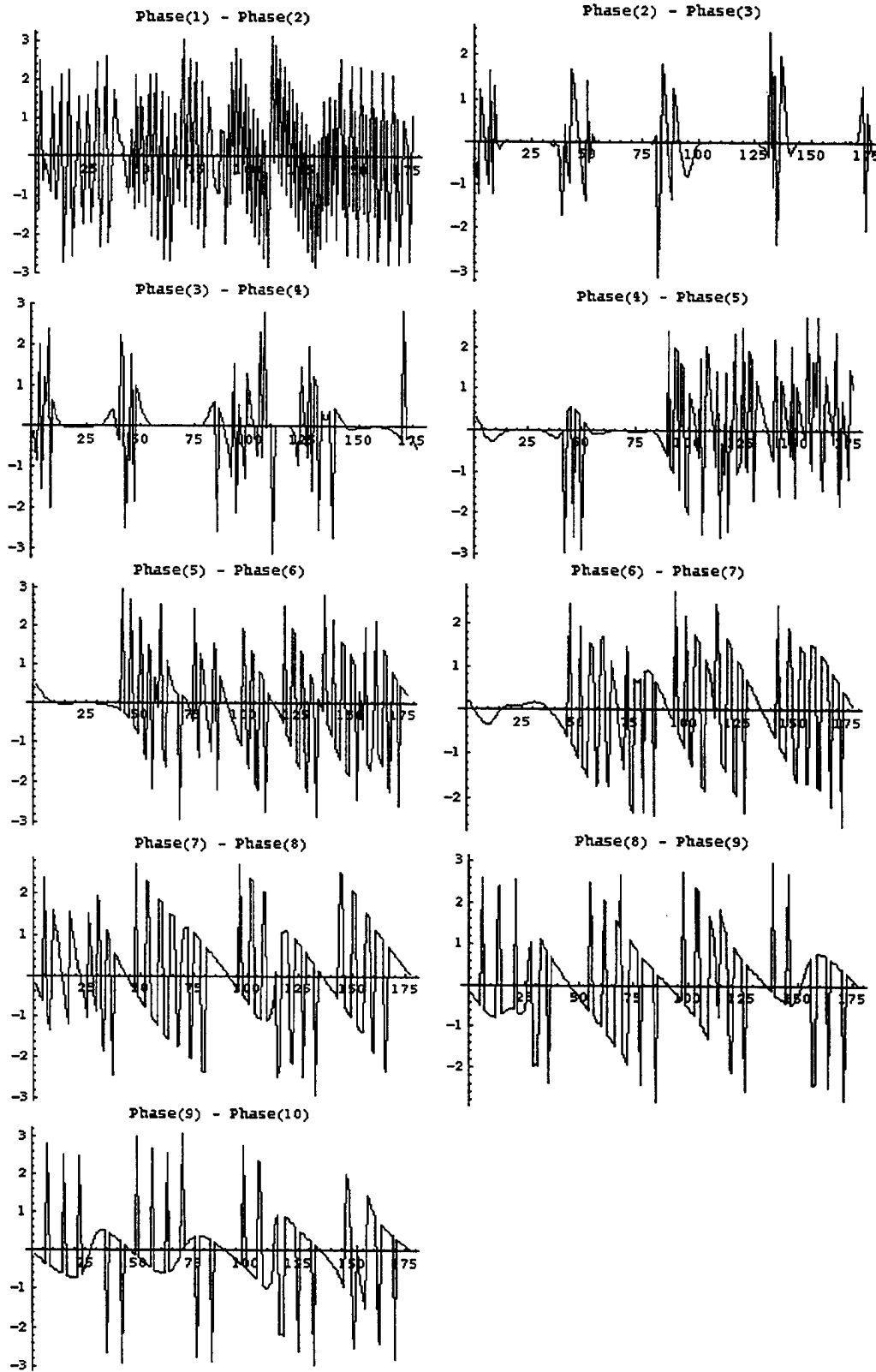
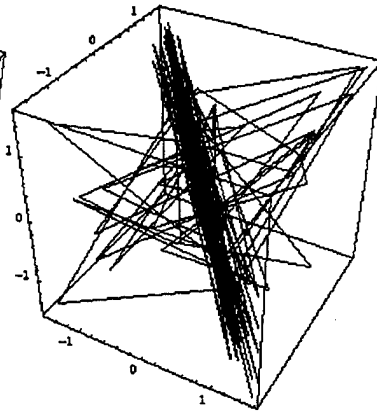
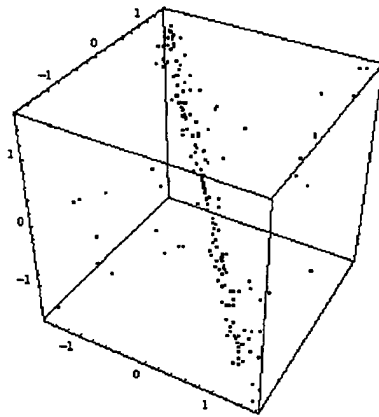
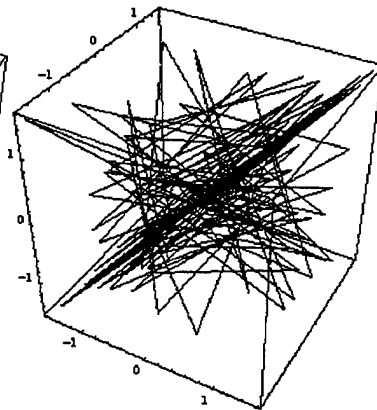
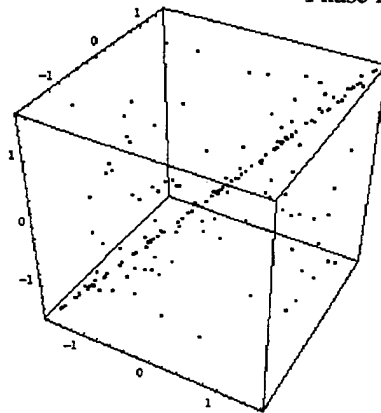


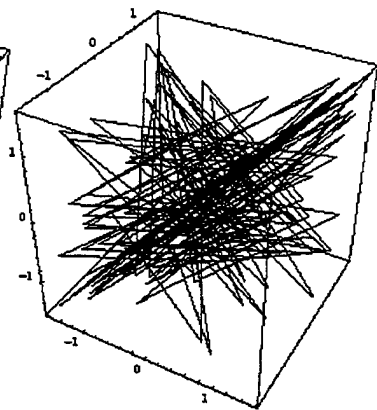
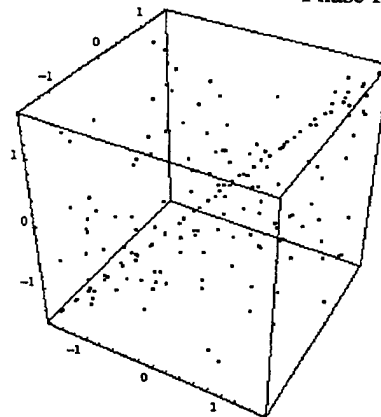
Fig. 11.4. Differential phase measurements: cuts through the 3-dimensional representation of Fig. 11.3.



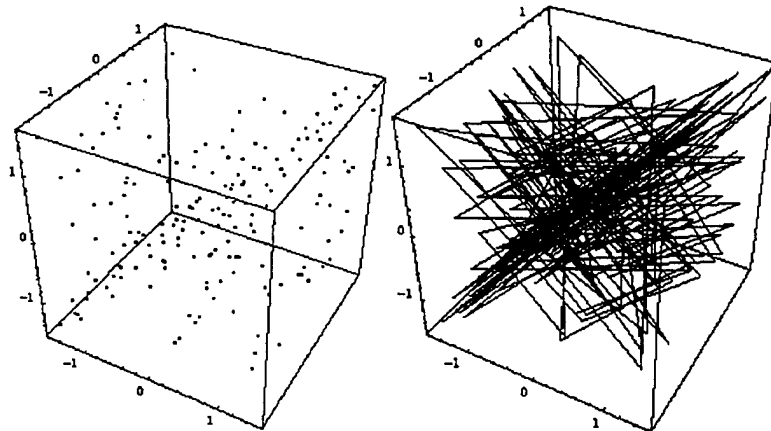
Phase for 1,2,3



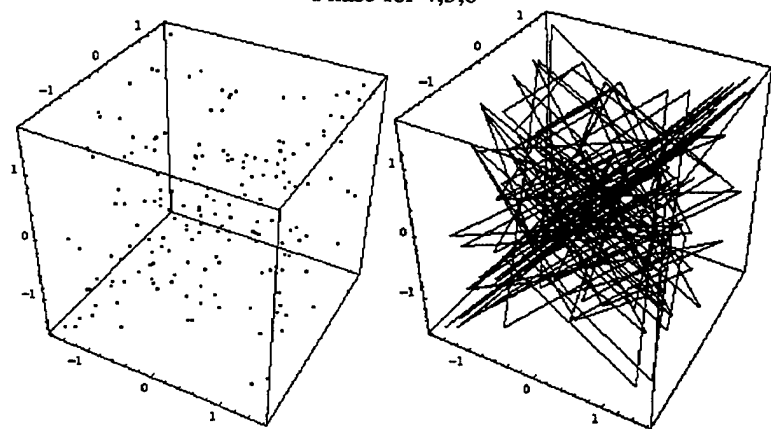
Phase for 2,3,4



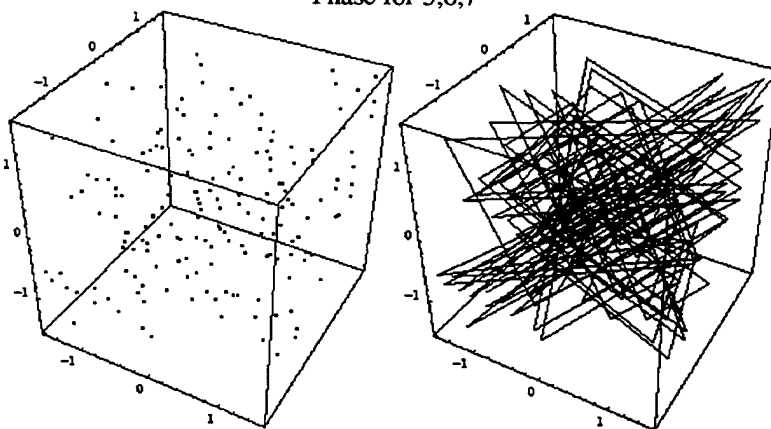
Phase for 3,4,5



Phase for 4,5,6



Phase for 5,6,7



Phase for 6,7,8

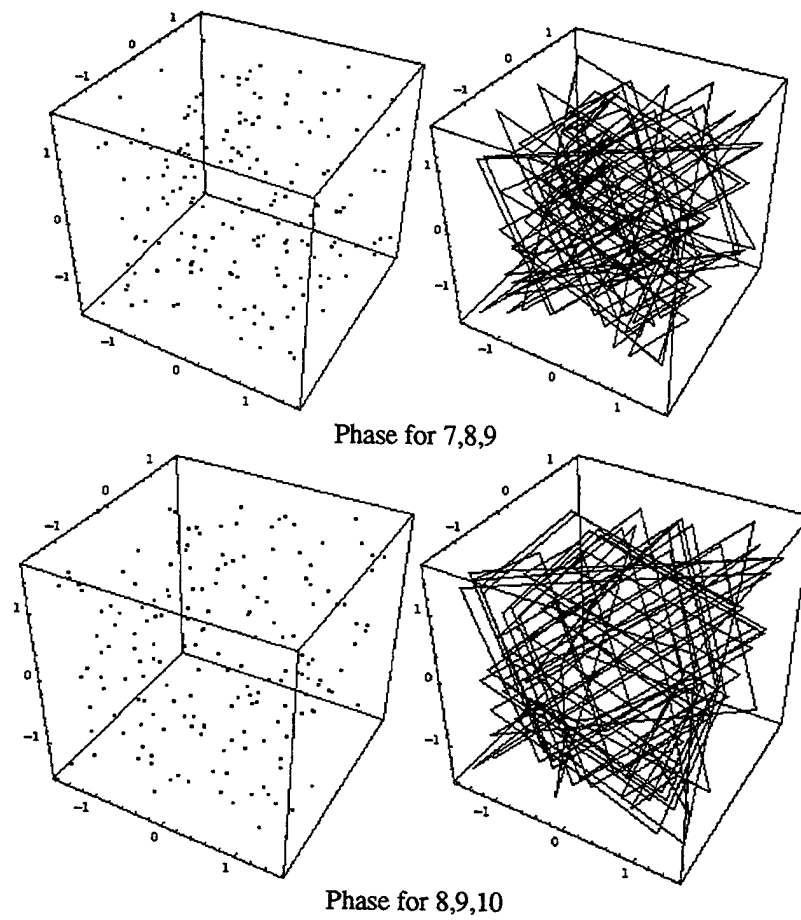
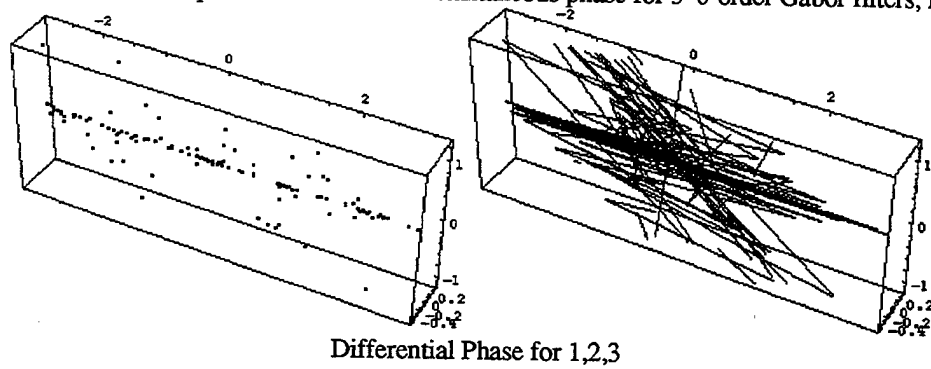
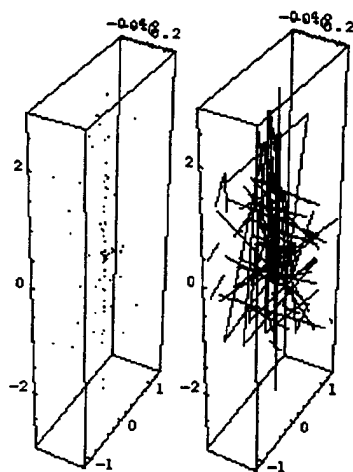
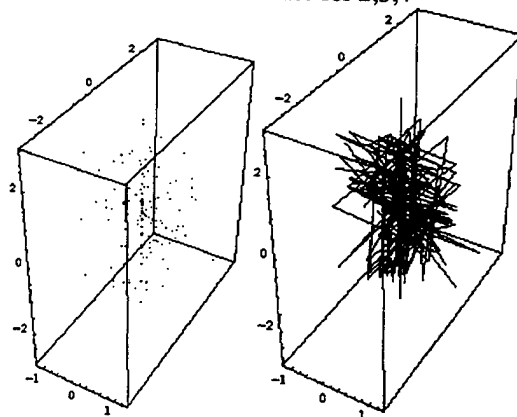


Fig. 11.5. 3-dimensional representations of the instantaneous phase for 3 0-order Gabor filters, from 1-10.

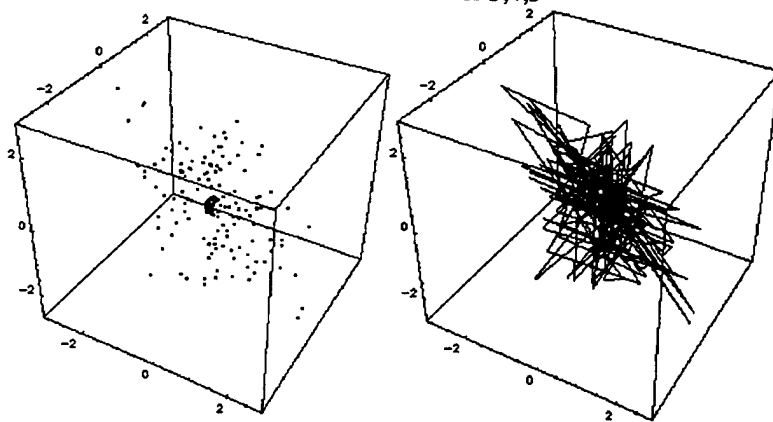




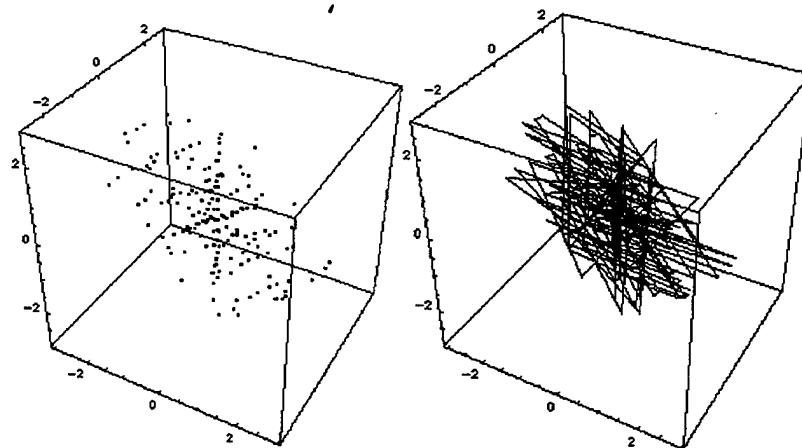
Differential Phase for 2,3,4



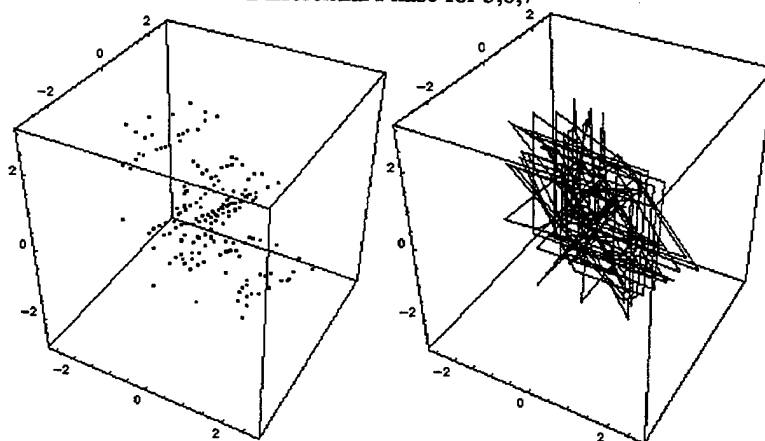
Differential Phase for 3,4,5



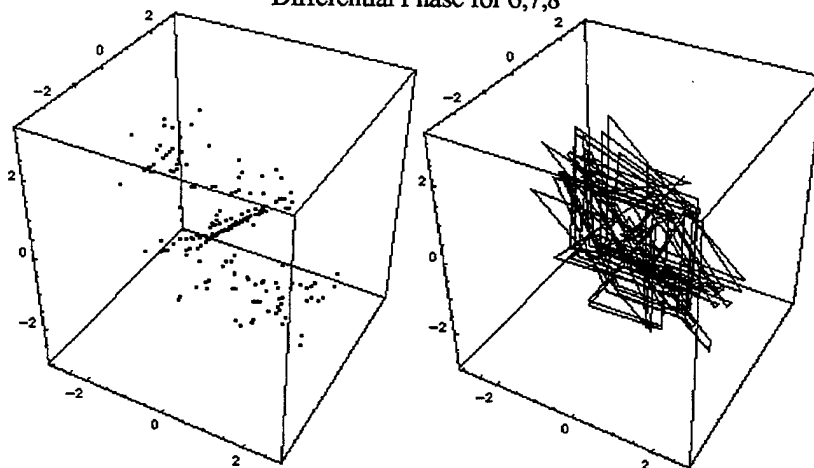
Differential Phase for 4,5,6



Differential Phase for 5,6,7



Differential Phase for 6,7,8



Differential Phase for 7,8,9

Fig. 11.6. 3-dimensional representations of the differential instantaneous phase for 3 0-order Gabor filters, from 1-9.

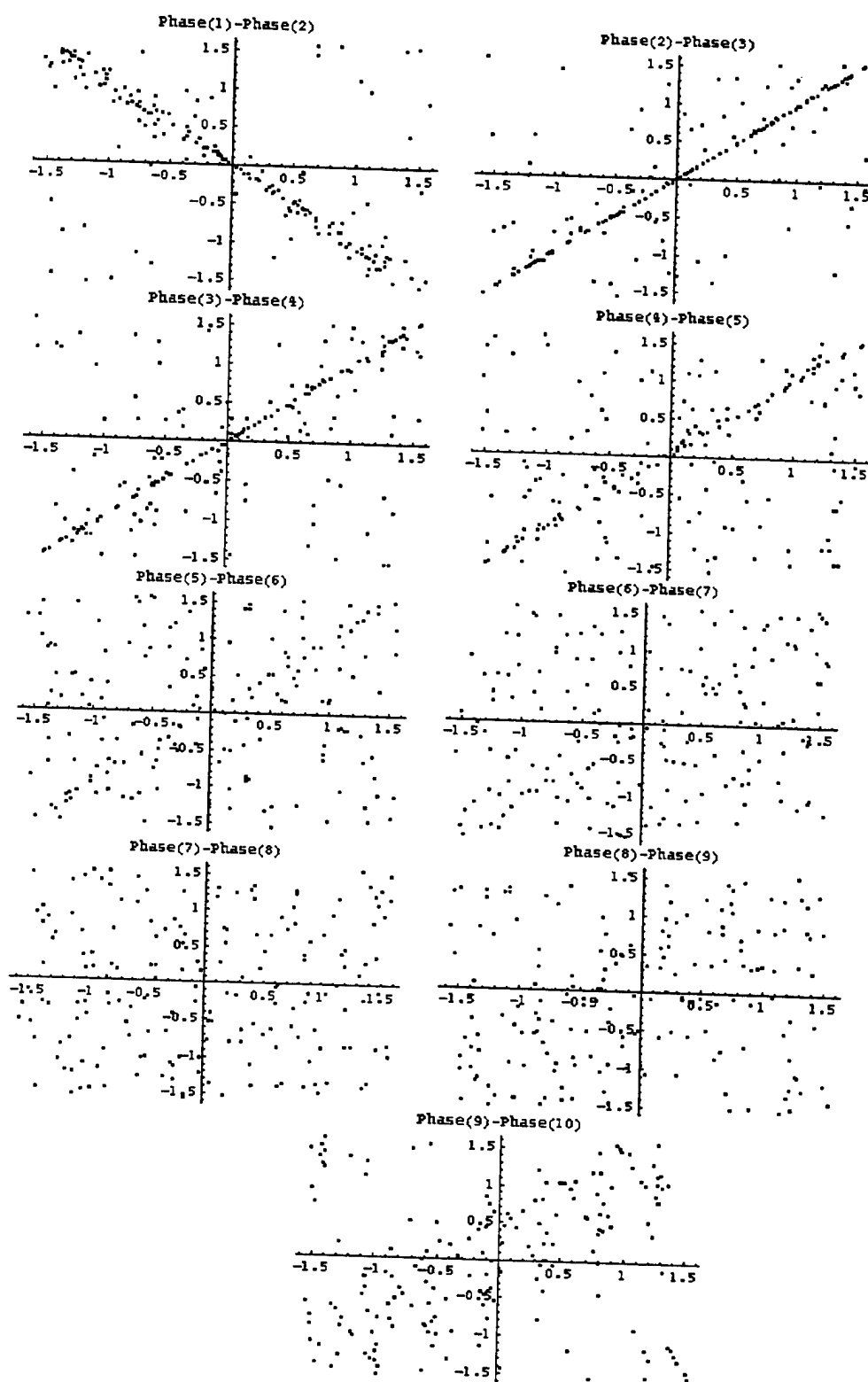


Fig. 11.7. Plots of instantaneous phases obtained from 0'th Gabor wavelet sampling.

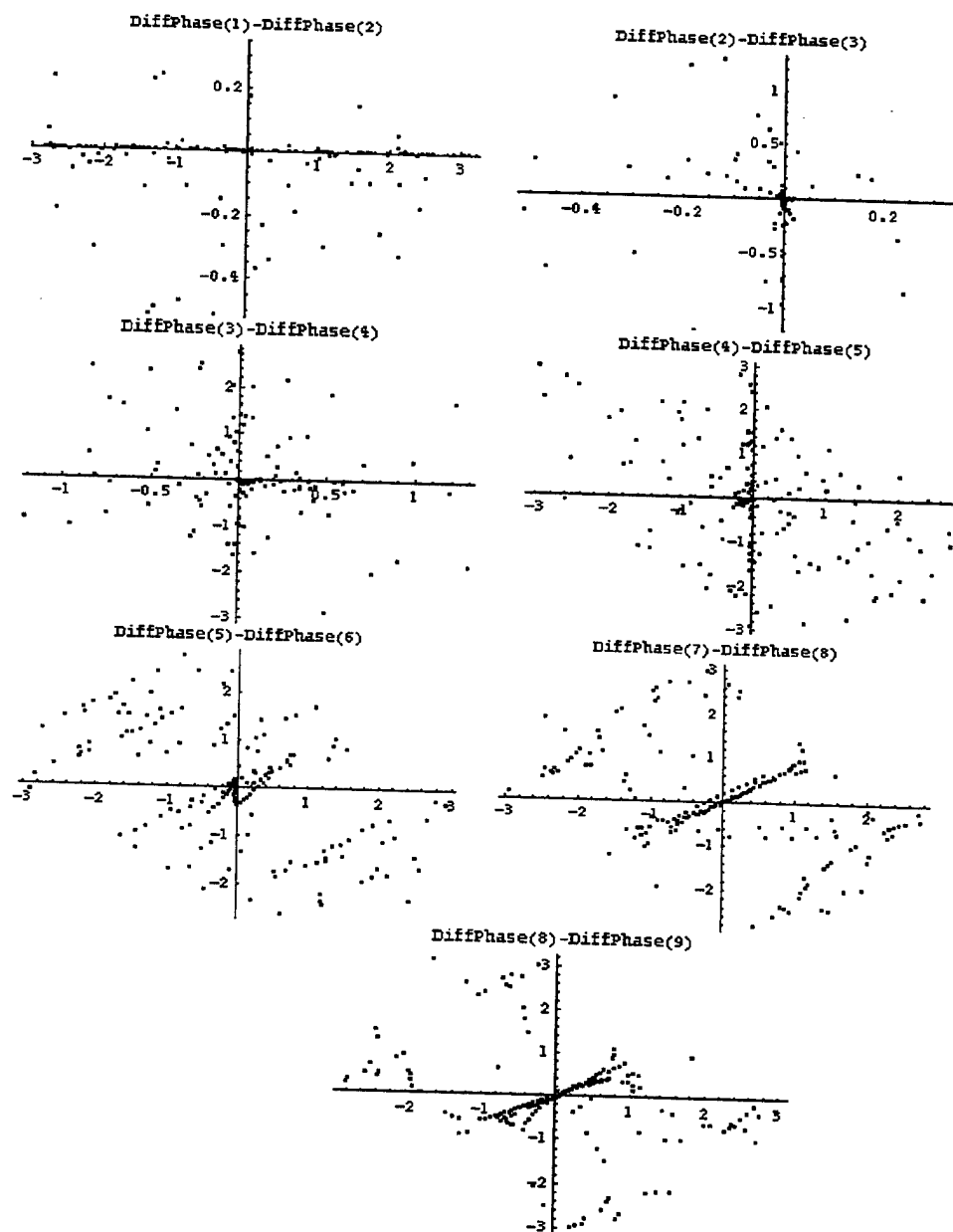


Fig. 11.8. Plots of differential instantaneous phases obtained from 0'th Gabor wavelet sampling.

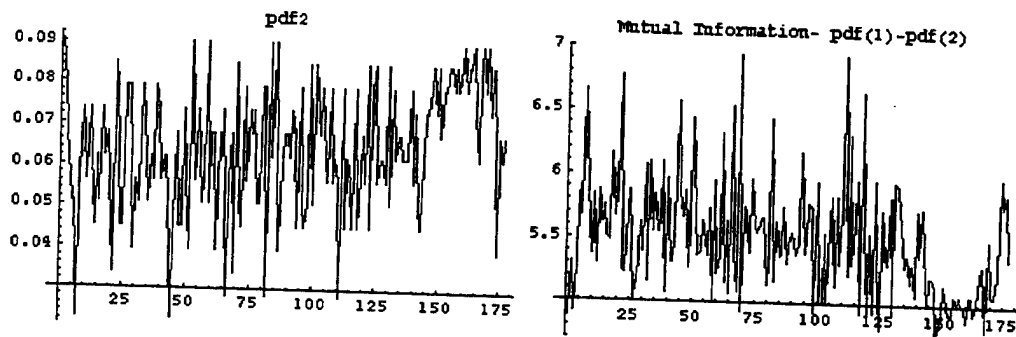


Fig. 11.9. Left: Probability density function obtained from the 2nd dilation of the 0th order wavelet Gabor transform; Right: the mutual information obtained from the 1st and 2nd probability density functions obtained from the 1st and 2nd dilations of the 0th order Gabor wavelet transform.

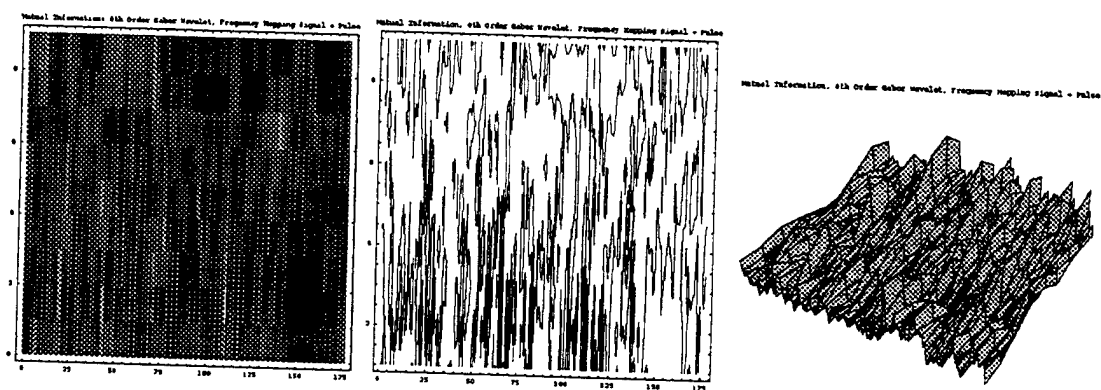


Fig. 11.10. The mutual information obtained from the 0th order Gabor wavelet transform for the signal of Fig. 11.1.

12.0 Fractals and Fano Factors

This section addresses the differentiation of two target return signals using (1) wavelet processing and (2) fractal analysis of the results of that wavelet analysis. Log-Log plots (amplitude versus filter scale) revealed stable distributions (as opposed to asymptotically Gaussian distribution) behavior - increasing in the case of one signal, and decreasing in the case of the other. This is a fractal property. The computed fractional dimension per time bin revealed clear differences between the two signals. The Fano factors for means across filters and for each time bin were also computed. There is a clear difference in the Fano factor patterns generated permitting the differentiation of the signals. Thus, fractal analysis appears to be a promising approach to differentiating signals and will be further explored in future months.

The fractal power relationship is that the measured value of a property $Q(r)$ depends on the resolution used to make the measurement with the equation:

$$Q(r) = Br^b f\left(\frac{\log(r)}{\log(a)}\right)$$

where B , b and a are constants and $f(x)$ is a periodic function such that $f(1+x) = f(x)$. In its simpler form, this relationship is:

$$Q(r) = Br^b$$

Thus in the case of fractal data, the scaling relationship for a statistical property $Q(r)$ has a power law form in that $Q(r)$ is proportional to r^b , where r is the resolution. The exponent b is related to the fractal dimension.

The two are related as follows. The fractal dimension, d , means that a number of pieces or samples, $N(r)$, measured at resolution r is proportional to r^{-d} :

$$N(r) \approx r^{-d}.$$

The scaling exponent, b , means that the value of the property, $Q(r)$, measured at resolution r is proportional to r^b :

$$Q(r) \approx r^b.$$

Furthermore, the property, $Q(r)$, is also equal to the number, $N(r)$, of samples, multiplied by the length, r , of the samples:

$$Q(r) = rN(r).$$

Therefore, by substitution:

$$Q(r) = r \cdot r^{-d} = r^{1-d} = r^b,$$

and

$$d = 1 + b.$$

In general,

$$N(r) \approx r^{-d},$$

$$Q(r) \approx r^b,$$

$$Q(r) \approx [N(r)]^\alpha r^\beta$$

and therefore:

$$d = \frac{\beta - b}{\alpha},$$

where theoretical justification is needed for how $Q(r)$ depends on $N(r)$ and r . Below, we assume $\alpha = \beta = 1$.

Another measure of fractal behavior, the *Fano factor*, is equal to the variance/mean and its value is dependent on the window length over which the variance and mean are determined.

The connection of fractal behavior and wavelets is due to wavelet coefficients giving local information about differentiability and Hölder continuity of a function. Furthermore, an essential characteristic of the wavelet transform is the ability to analyze a process relative to scale or resolution. Also, the wavelet transform, by construction, builds a signal by successive refinements, commencing from a coarse approximation and proceeding at each step with finer details - a process identical to that of fractal constructions.

Therefore, we explored this relationship to determine whether this form of analysis might provide a useful thumbprint of target return signals.

12.1 Applications

The analysis was conducted on two representative target signal returns shown in Fig. 12.1(A, B). The Gabor wavelet transforms of these signals, upon which the subsequent analysis was performed, are shown in Fig. 12.2. A log-log plot (amplitude versus filter scale) is shown for both signals in Fig. 12.3. Cuts through these plots (Fig. 12.4) show a stable distribution (as opposed to asymptotically Gaussian distribution) behavior - increasing in the case of one signal, and decreasing in the case of the other. This is a fractal property.

Using the log-log plots shown in Fig. 12.5, the fractional dimension per time bin was computed and the results are shown in Fig. 12.6. The differences between the two signals are clearly shown. Fig. 12.7 recalls the original signals of Fig. 12.1 overlaid with the fractional dimension plots of Fig. 12.6.

The Fano factors for means across filters and for each time bin are shown in Fig. 12.8. There is a clear difference in the patterns generated permitting the differentiation of the signals.

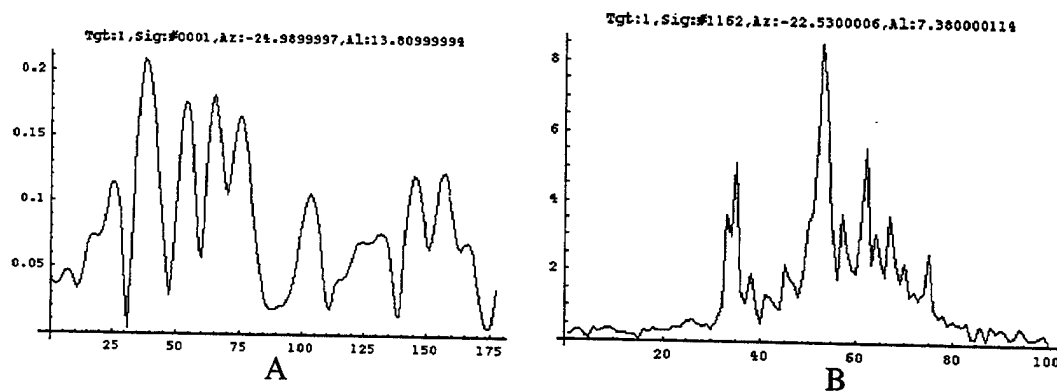


Fig. 12.1. A: Representative radar return signal #1; B: Representative radar return signal #2.

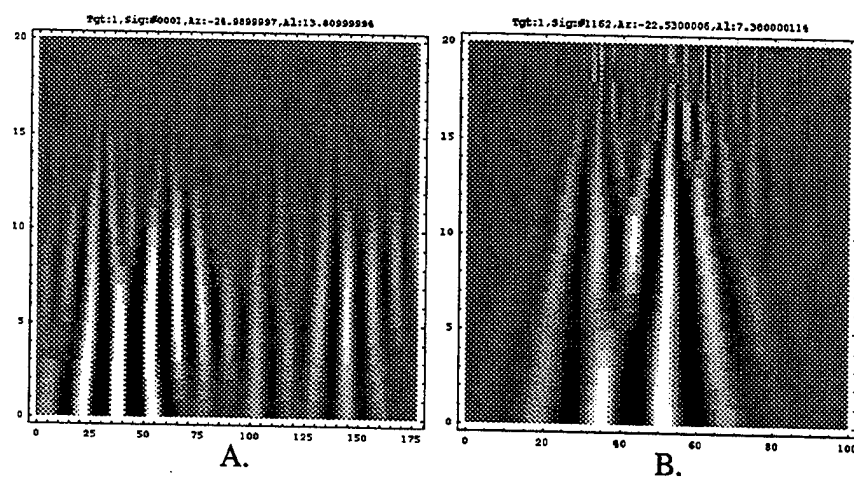


Fig. 12.2. (Gabor) wavelet transforms of signal #1 (A) and signal #2 (B).

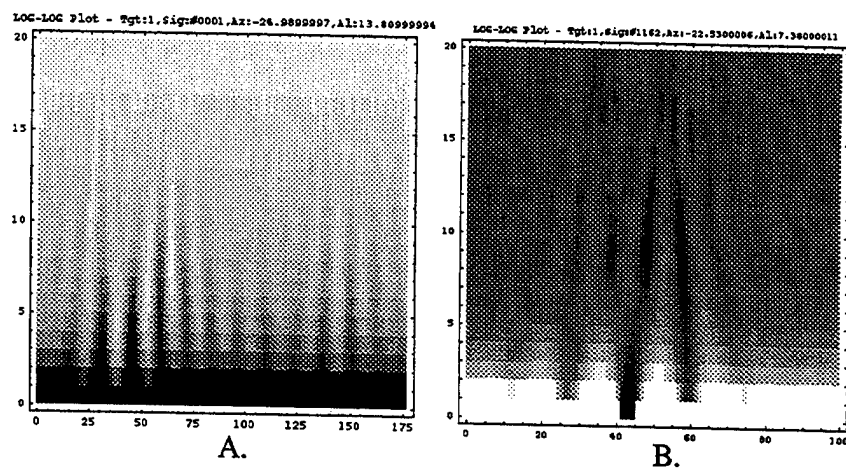


Fig. 12.3. Log-Log plots of wavelet transforms shown in Fig. 2.

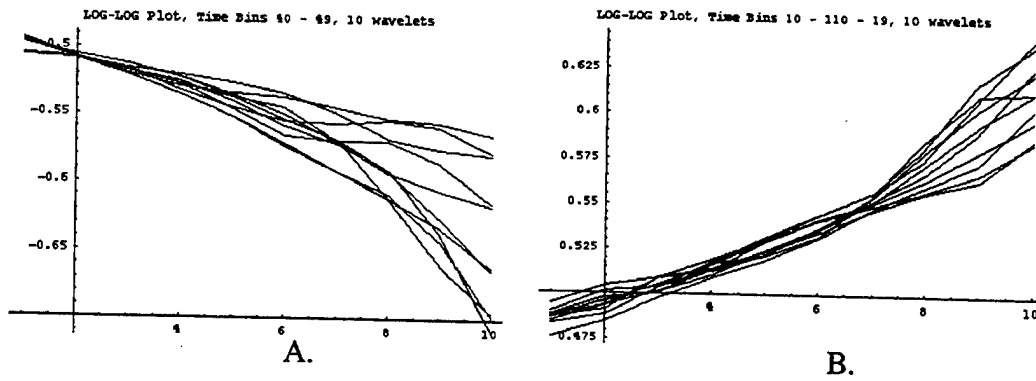


Fig. 12.4. Cuts through the log-log plots of Fig. 12.3 across transforms.

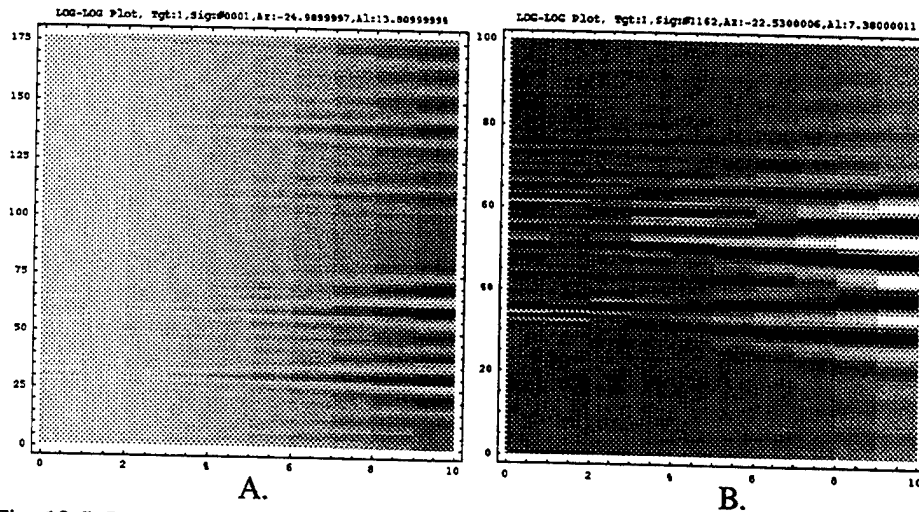


Fig. 12.5. Log-Log plots of wavelet transforms shown in Fig. 12.2 - 1st 10 transforms.

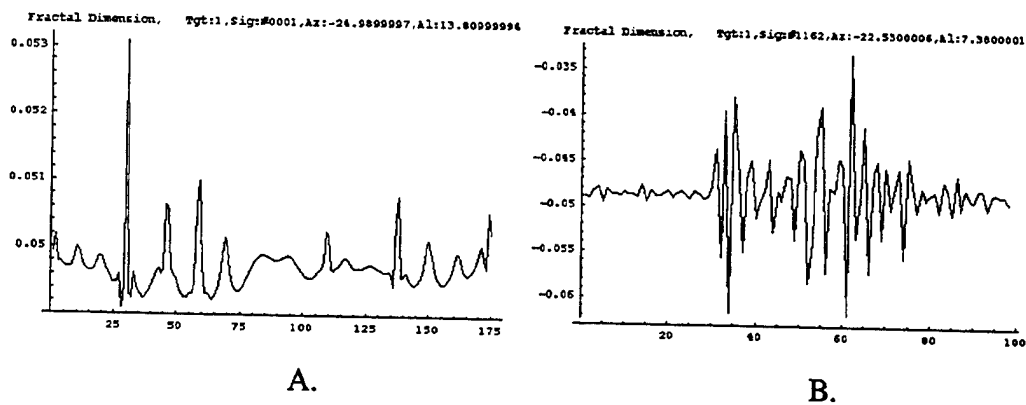


Fig. 12.6. Fractal dimensional representation of the signals of Fig. 12.2.

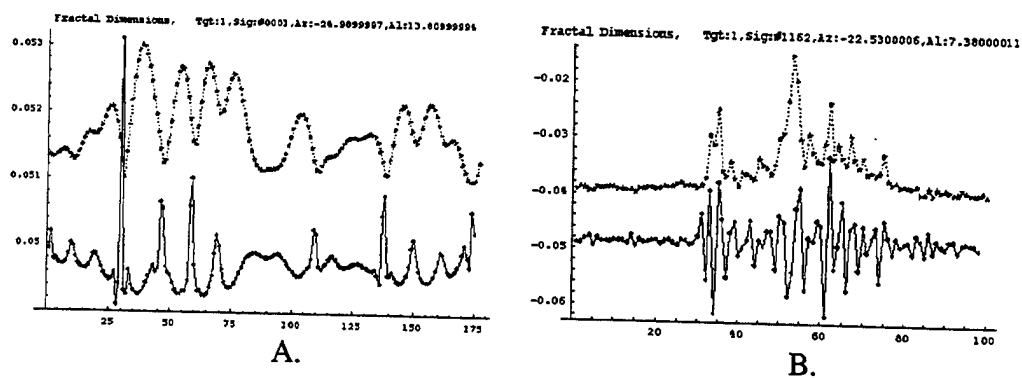


Fig.12.7. Fractal dimensional representation of the signals of Fig. 12.2 with overlay of those signals.

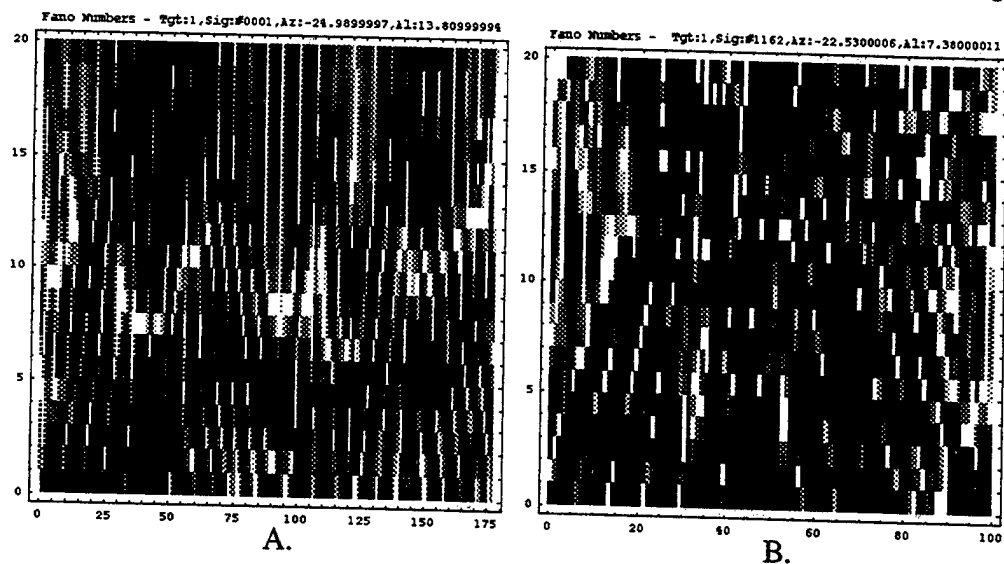


Fig. 12.8. Fano number representation of the signals of Fig. 12.2.

13.0 Group Theoretical Approaches

This section addresses analyses in terms of (a) higher-order symmetries; (b) differential forms; and (c) group theoretic, and formulations in electromagnetic theory of the role of the A -field in (a) nonlinear collective excitations in a 2-dimensional electron gas; and (b) solitons in new SAW devices and heterostructures in general. The method of generation of modulated TeraHertz pulses utilizes a plasma mirror dependent on the formation of soliton transmission. Therefore the following describes the commencement of an analysis of such soliton transmissions using the various approaches described.

The equation of motion derived by Harmuth¹:

$$\frac{\partial^2 E}{\partial y^2} - \mu\epsilon \frac{\partial^2 E}{\partial t^2} - (\mu\sigma + \epsilon s) \frac{\partial E}{\partial t} - s\sigma E = 0$$

incorporating s , the magnetic conductivity, was shown by Barrett² to be a two-dimensional Klein-Gordon equation in the sine-Gordon form, i.e., a soliton form. Soliton solutions require complete integrability and integrable systems conserve geometric features related to symmetry. Unlike the equations of motion for conventional Maxwell theory, which are solutions of U(1) symmetry systems, solitons are solutions of SU(2) symmetry systems. These notions of group symmetry are more fundamental than differential equation descriptions. Therefore, this we develop some basic concepts in order to place differential equation descriptions within the context of group theory.

Within this context, ordinary differential equations are viewed as vector fields on manifolds or configuration spaces. For example, Newton's equations are second order differential equations describing smooth curves on Riemannian manifolds. Noether's theorem states that a diffeomorphism, ϕ , of a Riemannian manifold, C , induces a diffeomorphism, $D\phi$, of its tangent bundle, TC . If ϕ is a symmetry of Newton's equations, then $D\phi$ preserves the Lagrangian, i.e.,

$$L \circ D\phi = L.$$

As opposed to equations of motion in conventional Maxwell theory, soliton flows are Hamiltonian flows. Such Hamiltonian functions define *symplectic structures* for which

¹ Harmuth, H.F., Correction for Maxwell's equations for signals I. *IEEE Trans. Electromagn. Compat.*, EMC-28, 250-258, 1986a;

_____, Correction for Maxwell's equations for signals II. *IEEE Trans. Electromagn. Compat.*, EMC-28, 259-265, 1986a;

² Barrett, T.W., Comments on the Harmuth Ansatz: use of a magnetic current density in the calculation of the propagation velocity of signals by amended Maxwell theory. *IEEE Trans. Electromagn. Compat.*, 30, 419-420, 1988.

_____, Comments on 'Solutions of Maxwell's equations for general nonperiodic waves in lossy media', *IEEE Trans. Electromagn. Compat.*, 31, 197-199, 1989.

_____, Comments on 'Some comments on Harmuth and his critics'. *IEEE Trans. Electromagn. Compat.*, 31, 201-202, 1989.

_____, Electromagnetic phenomena not explained by Maxwell's equations. pp. 6-86 in A. Lakhtakia (Ed.) *Essays on the Formal Aspects of Electromagnetic Theory*, World Scientific, 1993.

there is an absence of local invariants but an infinite dimensional group of diffeomorphisms which preserve global properties. In the case of solitons, the global properties are those permitting the matching of the nonlinear and dispersive characteristics of the medium through which the wave moves.

In order to relate the three major soliton equations to group theory it is necessary to examine the Lax equation or the zero-curvature condition (ZCC). The ZCC expresses the flatness of a connection by the commutation relations of the covariant derivative operators (Palais, 1997):

$$\left[\frac{\partial}{\partial x} - A, \frac{\partial}{\partial t} - B \right] = 0,$$

or

$$\left(\frac{\partial}{\partial x} - A \right)_t = \left[B, \frac{\partial}{\partial x} - A \right].$$

Palais (1997) shows that the generic cases of soliton - the Korteweg de Vries Equation (KdV), the Nonlinear Schrödinger Equation (NLS), the Sine-Gordon Equation (SGE) - can be given an $SU(2)$ formulation. In each case, below, V is a one-dimensional space that is embedded in the space of off-diagonal complex matrices, $\begin{pmatrix} 0 & b \\ c & 0 \end{pmatrix}$ and in each case $A(u) = a\lambda + u$, where u is a potential, λ is a complex parameter, and a is the constant, diagonal, trace zero matrix $a = \begin{pmatrix} -i & 0 \\ 0 & i \end{pmatrix}$ - which links these equation to an $SU(2)$ formulation.

From inverse scattering theory, a function is needed, defined:

$$B(\xi) = \sum_{n=1}^N c_n^2 \exp[-\kappa_n \xi] + \frac{1}{2\pi} \int_{-\infty}^{+\infty} b(k) \exp[ik\xi] dk, \text{ where}$$

$-\kappa_1^2, \dots, -\kappa_N^2$ are discrete eigenvalues of u ,

c_1, \dots, c_N are normalizing consts, and

$b(k)$ are reflection coefficients.

In the first case, if $u(x) = \begin{pmatrix} 0 & q(x) \\ -1 & 0 \end{pmatrix}$ and

$$B(u) = a\lambda^3 + u\lambda^2 + \begin{pmatrix} \frac{i}{2}q & \frac{i}{2}q_x \\ 0 & -\frac{i}{2}q \end{pmatrix} \lambda + \begin{pmatrix} \frac{q_x}{4} & \frac{-q^2}{2} \\ \frac{q}{2} & \frac{-q_x}{4} \end{pmatrix},$$

then ZCC is satisfied if and only if q satisfies the KdV in the form $q_t = -\frac{1}{4}(6qq_x + q_{xxx})$.

In the second case, if $u(x) = \begin{pmatrix} 0 & q(x) \\ -\bar{q}(x) & 0 \end{pmatrix}$ and

$$B(u) = a\lambda^3 + u\lambda^2 + \begin{pmatrix} \frac{i}{2}|q|^2 & \frac{i}{2}q_x \\ -\frac{i}{2}\bar{q}_x & -\frac{i}{2}|q|^2 \end{pmatrix},$$

then ZCC is satisfied if and only if $q(x,t)$ satisfies the NLS in the form $q_t = \frac{i}{2}(q_{xx} + 2|q|^2 q)$.

In the third case, if $u(x) = \begin{pmatrix} 0 & -\frac{q_x(x)}{2} \\ \frac{q_x(x)}{2} & 0 \end{pmatrix}$ and

$$B(u) = \frac{i}{4\lambda} \begin{pmatrix} \cos[q(x)] & \sin[q(x)] \\ \sin[q(x)] & -\cos[q(x)] \end{pmatrix},$$

then ZCC is satisfied if and only if q satisfies the SGE in the form $q_t = \sin[q]$.

Thus, with the equation of motion with electric *and* magnetic conductivity is in soliton (SGE) form, the group symmetry for which is SU(2). Solitons define Hamiltonian flows and their energy conservation is due to their symplectic structure.

The following are minimal topological and group theory definitions required to follow the above-initiated arguments. The groups used in Yang-Mills theory are *continuous* groups (as opposed to *discrete* groups). Unlike discrete groups, continuous groups contain an infinite number of elements and can be differentiable or analytic.

$U(n)$ Group Algebra

Unitary matrices have a determinant equal to ± 1 . The elements are represented by $n \times n$ unitary matrices.

$U(1)$ Group Algebra

The one-dimensional unitary group, or $U(1)$, is characterized by one continuous parameter. $U(1)$ is also differentiable and the derivative is also an element of $U(1)$. A well-known example of a $U(1)$ group is that of all the possible phases of a wave function, which are angular coordinates in a 2-dimensional space. When interpreted in this way - as the internal phase of the $U(1)$ group of electromagnetism - the $U(1)$ group is merely a circle (0 - 2π).

Möbius Group, M , Algebra

Möbius, or M , transformations map the extended complex plane one-to-one onto itself. An element is

$$m : C \rightarrow C \text{ or}$$

$$m(z) = \frac{az + b}{cz + d} \text{ with}$$

$$ad - bc \neq 0.$$

There is a homomorphism between M and $GL(2, C)$. The mapping from $GL(2, C)$ to M is:

$$\rho : \lambda \begin{pmatrix} a & b \\ c & d \end{pmatrix} \rightarrow m(z) = \frac{az + b}{cz + d}$$

The determinant of $\lambda \begin{pmatrix} a & b \\ c & d \end{pmatrix}$ is $\lambda^2 \det \begin{pmatrix} a & b \\ c & d \end{pmatrix}$, whence it is seen that (1) λ may be chosen in two ways and that (2) the determinant can be equal to ± 1 - which gives the group $SL(2, C)$.

Because of (1) it is seen that whereas $SL(2, C)$ is simply connected, M is not. Therefore $SL(2, C)$ is the universal covering group of M . If u and v are complex numbers and

$$u' = au + bv$$

$$v' = cu + dv$$

and if $z = u/v$ and $w = u'/v'$, then

$$w = \frac{az + b}{cz + d} \quad a, b, c, d \in \Re$$

and

$$ad - bc = 1.$$

$O(n)$ Group Algebra

The orthogonal group, $O(n)$, is the group of transformation (including inversion) in an n -dimensional Euclidean space. The elements of $O(n)$ are represented by $n \times n$ real orthogonal matrices with $n(n-1)/2$ real parameters satisfying $AA^t = 1$.

$O(3)$ Group Algebra

The orthogonal group, $O(3)$, is the well-known and familiar group of transformations (including inversions) in 3-dimensional space with 3 parameters, those parameters being the rotation or Euler angles (α, β, γ) . $O(3)$ leaves the distance squared, $x^2 + y^2 + z^2$, invariant.

$SO(2)$ Group Algebra

The collection of matrices in Euclidean 2-dimensional space (the plane) which are orthogonal and moreover for which the determinant is $+1$ is a subgroup of $O(2)$. $SO(2)$ is the special orthogonal group in two variables.

The rotations in the plane is represented by the $SO(2)$ group:

$$R(\theta) = \begin{pmatrix} \cos[\theta] & -\sin[\theta] \\ \sin[\theta] & \cos[\theta] \end{pmatrix} \quad \theta \in \Re$$

where

$$R(\theta)R(\gamma) = R(\theta + \gamma).$$

S^1 , or the unit circle in the complex plane with multiplication as the group operation is an $SO(2)$ group.

$SO(3)$ Group Algebra

The collection of matrices in Euclidean 3-dimensional space which are orthogonal and moreover for which the determinant is +1 is a subgroup of $O(3)$. $SO(3)$ is the special orthogonal group in three variables and defines rotations in 3-dimensional space.

Rotation of the Riemann sphere is a rotation in \Re^3 or $\xi - \eta - \zeta$ space, for which

$$\begin{aligned}\xi^2 + \eta^2 + \zeta^2 &= 1 \\ \xi &= \frac{2x}{|z|^2 + 1}, \quad \eta = \frac{2y}{|z|^2 + 1}, \quad \zeta = \frac{|z|^2 - 1}{|z|^2 + 1}, \\ z = x + iy &= \frac{\xi + i\eta}{1 - \zeta}.\end{aligned}$$

$$\begin{aligned}U_\xi(\alpha) &= \frac{1}{\sqrt{2}} \begin{pmatrix} 1 & -1 \\ 1 & 1 \end{pmatrix} \begin{pmatrix} e^{i\alpha/2} & 0 \\ 0 & e^{-i\alpha/2} \end{pmatrix} \frac{1}{\sqrt{2}} \begin{pmatrix} 1 & 1 \\ -1 & 1 \end{pmatrix} = \begin{pmatrix} \cos \alpha/2 & i \sin \alpha/2 \\ i \sin \alpha/2 & \cos \alpha/2 \end{pmatrix} \quad \text{or} \quad \pm U_\xi(\alpha) \rightarrow R_1(\alpha), \\ U_\eta(\beta) &= \frac{1}{\sqrt{2}} \begin{pmatrix} 1 & -i \\ -i & 1 \end{pmatrix} \begin{pmatrix} e^{i\beta/2} & 0 \\ 0 & e^{-i\beta/2} \end{pmatrix} \frac{1}{\sqrt{2}} \begin{pmatrix} 1 & i \\ i & 1 \end{pmatrix} = \begin{pmatrix} \cos \beta/2 & -\sin \beta/2 \\ \sin \beta/2 & \cos \beta/2 \end{pmatrix} \quad \text{or} \quad \pm U_\eta(\beta) \rightarrow R_2(\beta), \\ U_\zeta(\gamma) &= \frac{1}{\sqrt{2}} \begin{pmatrix} 1 & 0 \\ 0 & 1 \end{pmatrix} \begin{pmatrix} e^{i\gamma/2} & 0 \\ 0 & e^{-i\gamma/2} \end{pmatrix} \frac{1}{\sqrt{2}} \begin{pmatrix} 1 & 0 \\ 0 & 1 \end{pmatrix} = \begin{pmatrix} \cos \gamma/2 & -\sin \gamma/2 \\ \sin \gamma/2 & \cos \gamma/2 \end{pmatrix} \quad \text{or} \quad \pm U_\zeta(\gamma) \rightarrow R_3(\gamma).\end{aligned}$$

which are mappings from $SL(2, C)$ to $SO(3)$. However, as the $SL(2, C)$ are all unitary with determinant equal to +1, they are of the $SU(2)$ group. Therefore $SU(2)$ is the covering group of $SO(3)$. Furthermore, $SU(2)$ is simply connected and $SO(3)$ is multiply connected.

A simplification of the above is:

$$\begin{aligned}U_\xi(\alpha) &= e^{i(\alpha/2)\sigma_1}, \\ U_\eta(\beta) &= e^{-i(\beta/2)\sigma_2}, \\ U_\zeta(\gamma) &= e^{i(\gamma/2)\sigma_3}, \quad \text{where} \\ \sigma_1 &= \begin{pmatrix} 0 & 1 \\ 1 & 0 \end{pmatrix}, \quad \sigma_2 = \begin{pmatrix} 0 & -i \\ i & 0 \end{pmatrix}, \quad \sigma_3 = \begin{pmatrix} 1 & 0 \\ 0 & -1 \end{pmatrix}.\end{aligned}$$

$\sigma_1, \sigma_2, \sigma_3$ are the Pauli matrices.

$SU(n)$ Group Algebra

Unitary matrices have a determinant equal to ± 1 . Special unitary matrices are elements of unitary matrices which leave the determinant equal to +1. There are $n^2 - 1$ independent parameters. $SU(n)$ is a subgroup of $U(n)$ for which the determinant equals +1.

$SU(2)$ Group Algebra

$SU(2)$ is a subgroup of $SL(2, C)$. There are $2^2 - 1 = 3$ independent parameters for the special unitary group $SU(2)$ of 2×2 matrices. $SU(2)$ is a Lie algebra such that for the angular momentum generators, J_i , the commutation relations are $[J_i, J_j] = i\epsilon_{ijk}J_k, i, j, k = 1, 2, 3$. The $SU(2)$ group describes rotation in 3-dimensional space with 2 parameters (see below). There is a well-known $SU(2)$ matrix relating the Euler angles of $O(3)$ and the complex parameters of $SU(2)$ is:

$$\begin{pmatrix} \cos\left[\frac{\beta}{2}\right] \exp\left[\frac{i(\alpha + \gamma)}{2}\right] & \sin\left[\frac{\beta}{2}\right] \exp\left[\frac{-(\alpha - \gamma)}{2}\right] \\ -\sin\left[\frac{\beta}{2}\right] \exp\left[\frac{i(\alpha - \gamma)}{2}\right] & \cos\left[\frac{\beta}{2}\right] \exp\left[\frac{-i(\alpha + \gamma)}{2}\right] \end{pmatrix}$$

where α, β, γ are the Euler angles. It is also well known that a homomorphism exists between $O(3)$ and $SU(2)$, and the elements of $SU(2)$ can be associated with rotations in $O(3)$; and $SU(2)$ is the *covering group* of $O(3)$. Therefore, it is easy to show that $SU(2)$ can be obtained from $O(3)$. These $SU(2)$ transformations define the relations between the Euler angles of group $O(3)$ with the parameters of $SU(2)$. For comparison with the above, if the rotation matrix $R(\alpha, \beta, \gamma)$ in $O(3)$ is represented as:

$$\begin{pmatrix} \cos[\alpha]\cos[\beta]\cos[\gamma] - \sin[\alpha]\sin[\gamma] & \sin[\alpha]\cos[\beta]\cos[\gamma] + \cos[\alpha]\sin[\gamma] & -\sin[\beta]\cos[\gamma] \\ -\cos[\alpha]\cos[\beta]\sin[\gamma] - \sin[\alpha]\cos[\gamma] & -\sin[\alpha]\cos[\beta]\sin[\gamma] + \cos[\alpha]\cos[\gamma] & \sin[\beta]\sin[\gamma] \\ \cos[\alpha]\sin[\beta] & \sin[\alpha]\sin[\beta] & \cos[\beta] \end{pmatrix}$$

then the orthogonal rotations about the coordinate axes are:

$$R_1(\alpha) = \begin{pmatrix} \cos[\alpha] & \sin[\alpha] & 0 \\ -\sin[\alpha] & \cos[\alpha] & 0 \\ 0 & 0 & 1 \end{pmatrix}$$

$$R_2(\beta) = \begin{pmatrix} \cos[\beta] & 0 & -\sin[\beta] \\ 0 & 1 & 0 \\ \sin[\beta] & 0 & \cos[\beta] \end{pmatrix}$$

$$R_3(\gamma) = \begin{pmatrix} \cos[\gamma] & \sin[\gamma] & 0 \\ -\sin[\gamma] & \cos[\gamma] & 0 \\ 0 & 0 & 1 \end{pmatrix}$$

An isotropic parameter, ϖ , can be defined:

$$\varpi = \frac{x - iy}{z},$$

where x, y, z are the spatial coordinates. If ϖ is written as the quotient of μ_1 and μ_2 , or the homogeneous coordinates of the bilinear transformation, then:

$$|\mu_1 \mu_2\rangle = \begin{bmatrix} \cos\left[\frac{\beta}{2}\right] \exp\left[\frac{i(\alpha+\gamma)}{2}\right] & \sin\left[\frac{\beta}{2}\right] \exp\left[\frac{-(\alpha-\gamma)}{2}\right] \\ -\sin\left[\frac{\beta}{2}\right] \exp\left[\frac{i(\alpha-\gamma)}{2}\right] & \cos\left[\frac{\beta}{2}\right] \exp\left[\frac{-i(\alpha+\gamma)}{2}\right] \end{bmatrix} |\mu_1 \mu_2\rangle$$

which is the relation between the Euler angles of $O(3)$ and the complex parameters of $SU(2)$. However, there is not a unique one-to-one relation, for 2 rotations in $O(3)$ correspond to 1 direction in $SU(2)$. There is thus a many-to-one or homomorphism between $O(3)$ and $SU(2)$.

In the case of a complex 2-dimensional vector (u, v) :

$$\begin{pmatrix} u' \\ v' \end{pmatrix} = \begin{pmatrix} \cos\left[\frac{\beta}{2}\right] \exp\left[\frac{i(\alpha+\gamma)}{2}\right] & \sin\left[\frac{\beta}{2}\right] \exp\left[\frac{-(\alpha-\gamma)}{2}\right] \\ -\sin\left[\frac{\beta}{2}\right] \exp\left[\frac{i(\alpha-\gamma)}{2}\right] & \cos\left[\frac{\beta}{2}\right] \exp\left[\frac{-i(\alpha+\gamma)}{2}\right] \end{pmatrix} \begin{pmatrix} u \\ v \end{pmatrix}$$

If we define:

$$a = \cos\left[\frac{\beta}{2}\right] \exp\left[\frac{i(\alpha+\gamma)}{2}\right]$$

$$b = \sin\left[\frac{\beta}{2}\right] \exp\left[\frac{-(\alpha-\gamma)}{2}\right],$$

then

$$|\mu_1 \mu_2\rangle = \begin{bmatrix} a & b \\ -b^* & a^* \end{bmatrix} |\mu_1 \mu_2\rangle,$$

where

$$\begin{bmatrix} a & b \\ -b^* & a^* \end{bmatrix}$$

are the well-known $SU(2)$ transformation rules. Defining: $c = -b^*$ and $d = a^*$, we have the determinant:

$$ad - bc = 1$$

or

$$aa^* - b(-b^*) = 1.$$

Defining the (x,y,z) coordinates with respect to a complex 2-dimensional vector (u,v) as:

$$x = \frac{1}{2}(u^2 - v^2),$$

$$y = \frac{1}{2i}(u^2 + v^2),$$

$$z = uv$$

then $SU(2)$ transformations leave the squared distance $x^2 + y^2 + z^2$ invariant.

Every element of $SU(2)$ can be written as:

$$\begin{bmatrix} a & b \\ -b^* & a^* \end{bmatrix}, \text{ where}$$

$$|a|^2 + |b|^2 = 1.$$

Now if we define:

$$a = y_1 - iy_2,$$

$$b = y_3 - iy_4,$$

then the parameters y_1, y_2, y_3, y_4 indicate positions in $SU(2)$ with the constraint:

$$y_1^2 + y_2^2 + y_3^2 + y_4^2 = 1,$$

which indicates that the group $SU(2)$ is a 3-dimensional unit sphere in the 4-dimensional y -space. This means that any closed curve on that sphere can be shrunk to a point. In other words, $SU(2)$ is *simply-connected*.

$SU(2)$ is the quantum mechanical "rotation group".

$SU(3)$ Group Algebra

$SU(3)$ has $n^2 - 1 = 8$ generators.

$SL(2,C)$ Group Algebra

The special linear group of 2×2 matrices of determinant 1 with complex entries is $SL(2,C)$.

$GL(n,R)$ Group Algebra

The collection of real non-singular $n \times n$ invertible matrices is $GL(n,R)$ or the real general linear group in n variables.

$SL(n,R)$ Group Algebra

$SL(n,R)$ is a subgroup of $GL(n,R)$ with determinant = +1.

$GL(n,C)$ Group Algebra

The collection of complex non-singular $n \times n$ invertible matrices is $GL(n,C)$ or the complex general linear group in n variables.

SL(n,C) Group Algebra

SL(n,C) is a subgroup of *GL(n,C)* with determinant = +1.

Sp(2,n) Group Algebra

A $2n$ -dimensional space can be defined as:

$$(x,y) = (x^1 y^{n+1} - x^{n+1} y^1) + (x^2 y^{n+2} - x^{n+2} y^2) + \dots + (x^n y^{2n} - x^{2n} y^n) \\ = x^t J y$$

Sp(2,n) is a noncompact symplectic group with form invariance:

$$J = \begin{pmatrix} 0 & \mathbf{1}_n \\ -\mathbf{1}_n & 0 \end{pmatrix} \text{ where } \mathbf{1}_n = n \times n \text{ unit matrix.}$$

Sp(2,n) satisfy:

$$A^t J A = J.$$

Lie Group Algebras

If a topological group is a group and also a topological space in which group operations are continuous, then Lie groups are topological groups which are also analytic manifolds on which the group operations are analytic.

In the case of Lie algebras, the parameters of a product are analytic functions of the parameters of each factor in the product. For example,

$$L(\gamma) = L(\alpha)L(\beta)$$

where

$$\gamma = f(\alpha, \beta).$$

This guarantees that the group is differentiable. The Lie groups used in Yang-Mills theory are *compact* groups, i.e., the parameters range over a closed interval.

13.1 Calculations:

The nonlinear Schrödinger equation (NLS) is:

$$\frac{\partial q}{\partial Z} = \frac{i}{2} \frac{\partial^2 q}{\partial T^2} + i|q|^2 q + \epsilon \beta_1 \left(\frac{\partial^3 q}{\partial T^3} + 6|q|^2 \frac{\partial q}{\partial T} \right)$$

where

q is the normalized effective amplitude of the wave electric field:

$$q = \frac{2\pi g n_2}{\lambda \epsilon} E,$$

where g is the gain, n_2 is the Kerr coefficient, $\lambda = 2\pi c / \omega$, $\epsilon = \Delta\omega / \omega_1$ is a small parameter and E is the electric field intensity;

T is time normalized by the characteristic time, t_0 , of the side band spectrum, $(\Delta\omega_1)^{-1}$, and the coordinate τ , defined: $\tau = \varepsilon(t - k'z)$, where k' is the derivative of the wavenumber or $\partial k/\partial\omega$ evaluated at ω_l , the angular frequency of the coherent light carrier and z is the axial distance. T is therefore:

$$T = \frac{\tau}{t_0}.$$

Z is the axial distance normalized by the dispersion distance, $z_0 = -t_0^2/k''$, defined for the spectrum, $\Delta\omega_1$, and, ζ , defined: $\zeta = \varepsilon^2/z$. Z is therefore:

$$Z = \frac{\zeta}{z_0}.$$

$\beta_1 = \frac{1}{6} \frac{k_1'''' z_0}{t_0^3}$ is the linear higher-order dispersion coefficient.

The bound two-soliton solution or N -soliton solution of the NLS equation is³:

$$q = \frac{2}{\Delta} \left(\frac{\eta_1 + \eta_2}{\eta_1 - \eta_2} \right) (\eta_1 \cosh \theta_2 \exp[i\sigma_1] + \eta_2 \cosh \theta_1 \exp[i\sigma_2])$$

where

$$\Delta = \cosh(\theta_1 + \theta_2) + \left(\frac{\eta_1 + \eta_2}{\eta_1 - \eta_2} \right) \cosh(\theta_1 - \theta_2) + \frac{4\eta_1\eta_2}{(\eta_1 - \eta_2)^2} \cos(\sigma_1 - \sigma_2),$$

$$\theta_l = \eta_l T + \theta_{l0} \quad l = 1, 2$$

$$\theta_{0l} = \text{constant}.$$

The phase, σ_l , satisfies:

$$\frac{d\sigma_l}{dZ} = \frac{1}{2} \eta_l^2.$$

η represents the amplitude as well as the pulse width of the soliton.

This solution is found for the input pulse shape initial value:

$$q(T, 0) = A \operatorname{sech} T.$$

Fig. 13.1 shows examples for two values of η_1 and η_2 and with $\theta_l = \eta_l T$, $\sigma_l = \eta_l^2 Z/2$ for $l = 1, 2$.

Higher-order terms appear at distances longer than $10^4 z_0$. In this case, $\eta_{1,2}$ are defined as³:

³ Hasegawa, A. & Kodama, Y., *Solitons in Optical Communications*, Oxford U. Press, 1995.

$$\eta_{1,2} \approx 1 \pm 2 \exp\left[-\frac{T_0}{2}\right].$$

Fig. 13.2 shows the interaction of two equal amplitude pulses in the presence of third-order dispersion.

In order to increase the rate of pulse generation it is desirable to place solitons close to each other. However, because of the nonlinearity of the system, solitons mutually interact, leading to deterioration in the repetition rate. In the case of in-phase solitons with equal amplitude we consider the solution of the NLS equation with two soliton interaction. with $T_0 = 7$, corresponding to $\eta_1 = 1.072$, $\eta_2 = 0.952$ and $Z_p = 26.3$ (Fig. 13.3). $Z_c = Z_p/2$ is the collision distance of the pulses.

In the case of off-phase solitons with equal amplitudes, the NLS takes an asymptotic form:

$$q(T, Z) \approx \sum_{l=1}^2 \eta_l \operatorname{sech} \eta_l (T + \kappa_l Z - T_{0l}^{\pm}) \exp\left[-i\kappa_l T + i(\eta_l^2 - \kappa_l^2)/2 + i\sigma_{0l}^{\pm}\right], \quad \text{as } Z \rightarrow \pm\infty.$$

where

$$\begin{aligned} \kappa_{1,2} &\approx \pm 2 \exp\left[-\frac{T_0}{2}\right] \sin\left[\frac{\phi_0}{2}\right], \\ \eta_{1,2} &\approx 1 \pm 2 \exp\left[-\frac{T_0}{2}\right] \cos\left[\frac{\phi_0}{2}\right]. \end{aligned}$$

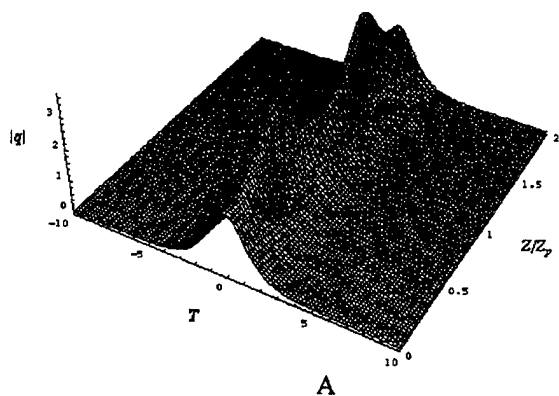
Fig. 13.4A shows the evolution of two unity amplitude sech pulses with an initial phase difference of $\phi_0 = \pi/4$ and an initial pulse separation of $T_0 = 7$.

In the case of in-phase solitons with unequal amplitudes,

$$\eta_{1,2} = \pm \left[\frac{A_0 - 1}{2} + \operatorname{sech} \left[\frac{A_0 T_0}{2} \right] \right].$$

Fig. 13.5. shows the eigenvalues $\eta_{1,2}$ for two unequal amplitude sech pulses as a function of the initial separation T_0 and Fig. 13.4B. shows soliton interaction with two unequal amplitude pulses, $A_0 = 1.1$ and the initial pulse separation $T_0 = 7$.

Bound Two-Soliton Solutions
 $\eta_1 = 3, \eta_2 = 1, Z_p = \pi/2$



Bound Two-Soliton Solutions
 $\eta_1 = 3, \eta_2 = 1.5, Z_p = 16\pi/5$

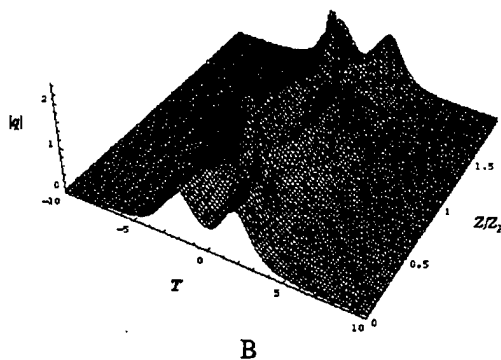
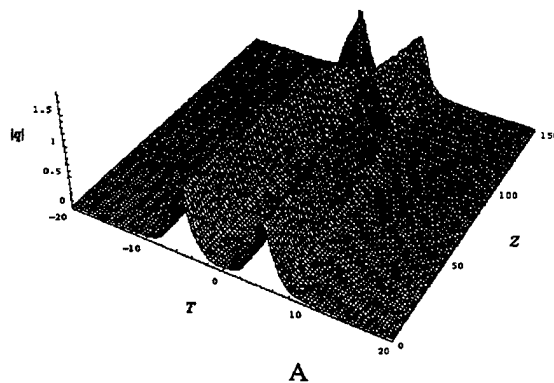


Fig. 13.1. Two examples of bound two-solitons. A: $\eta_1 = 3, \eta_2 = 1$, giving $Z_p = \pi/2$; B: $\eta_1 = 1.5, \eta_2 = 1$, giving $Z_p = 16\pi/5$.

Interaction of Two Equal Amplitude Pulses in the Presence of Third-Order Dispersion
 $\epsilon\beta_3 = 0.05$; initial separation: $T_0 = 10$.



Interaction of Two Equal Amplitude Pulses in the Presence of Third-Order Dispersion
 $\epsilon\beta_3 = 0.05$; initial separation: $T_0 = 7$.

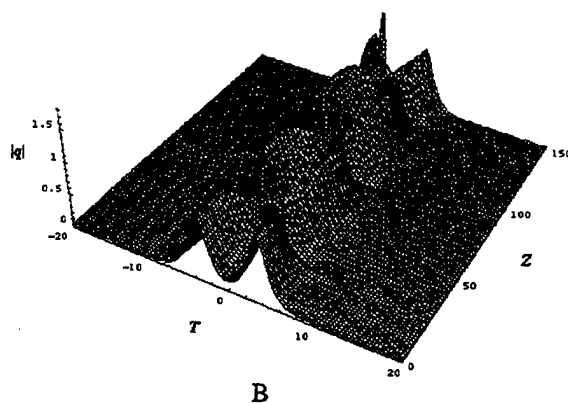


Fig. 13.2. Interaction of two equal amplitude pulses in the presence of third-order dispersion. (A): initial separation $T_0 = 10$; (B) initial separation $T_0 = 7$.

*Soliton interaction with two equal amplitude pulses;
initial pulse separation: $T_0 = 7$, corresponding to: $\eta_1 = 1.072$; $\eta_2 = 0.952$; $Z_p = 26.3$.*

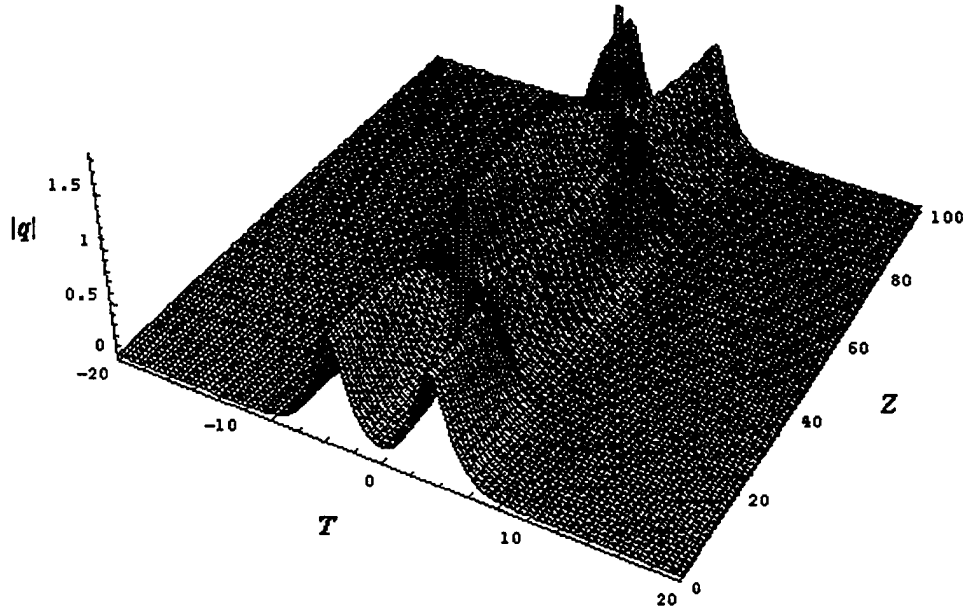


Fig. 13.3. Soliton interaction with two equal amplitude pulses. Initial pulse separation $T_0 = 7$.

*Evolution of Two Unity Amplitude Sech Pulses with initial phase difference of:
 $\phi_0 = \pi/4$; initial pulse separation: $T_0 = 7$.*

*Soliton interaction with two unequal amplitude pulses;
 $A_0 = 1.1$; initial pulse separation: $T_0 = 7$.*

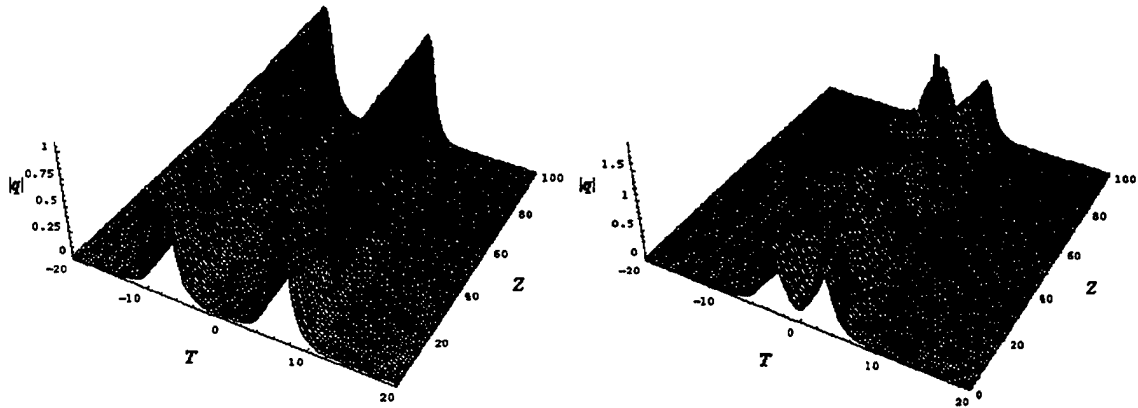


Fig. 13.4. (A) Evolution of two unity amplitude sech pulses with an initial phase difference of $\phi_0 = \pi/4$. Initial phase separation, $T_0 = 7$. (B) Soliton interaction with two unequal amplitude pulses, $A_0 = 1.1$ and the initial pulse separation $T_0 = 7$.

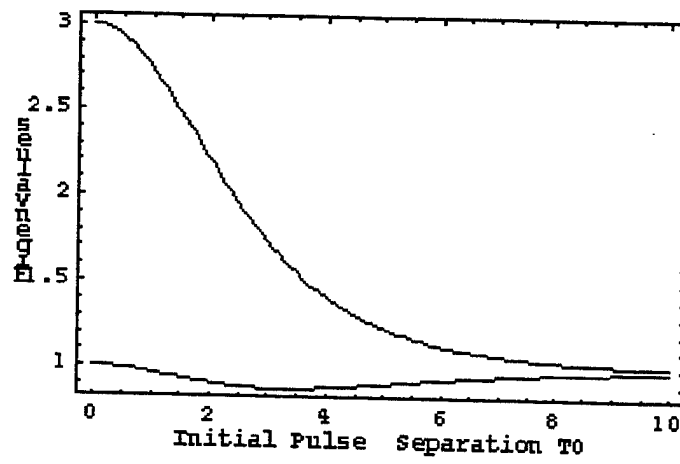


Fig. 13.5. Eigenvalues, $\eta_{1,2}$ for two unequal amplitude sech pulses as a function of the initial separation, T_0 .

14.0 The Bootstrap

This section addresses analyses offered by the Bootstrap method for estimating the accuracy of a parameter estimator taken, in the instances addressed, as radar signal returns. Here, we show - for the first time to our knowledge - that the technique can be applied to distinguish targets. We also apply techniques taken from fractal theory and deterministic chaos theory to show that radar returns have both a fractal nature and are not time series produced by a random mechanism, but rather by a deterministic chaotic mechanism. We are able to show that the fractal properties of the power spectra, the variance and Fano Factor distinguish between two target returns. Use of embedding dimensional analysis also reveals the deterministic chaotic, as opposed to random, nature of the radar returns. The third report from Northwestern University is also included.

The bootstrap⁴ is a technique for estimating the accuracy of a parameter estimator where additional re-samplings to gain additional raw data is not possible. In radar signal processing, large sample methods are not possible. Here we apply this technique to determine differences between two target returns (Fig. 14.1). The technique has only commenced to be used in radar processing⁵. The bootstrap does what in an ideal situation a radar operator would do if it were possible - that is, the operator would repeat again and again irradiating a stationary target (as if it were on a range). In the case of the bootstrap, the measurements in each time bin of the signal return are randomly reassigned and estimates are recomputed. This can be done hundreds, even thousands, of times and the results are treated as if they were real repeat test measurements.

In Ref⁵ there is discussed an application in which the distribution of the estimated "close approach probability" is used as an index of collision risk in air traffic control. Here, we show - for the first time to our knowledge - that the technique can be applied to distinguish targets.

⁴ Tibshirani, R.J., Variance stabilization and the bootstrap. *Biometrika*, 75, 433-444, 1988.

Efron, B. & Tibshirani, R., Bootstrap methods for standard errors, confidence intervals and other measures of statistical accuracy. *Statistical Science*, 1, No 1, 1217-1241, 1989.

Efron, B. & Tibshirani, R.J., *An Introduction to the Bootstrap*, Chapman & Hall, NY, 1993.

Zouhir, A.M. & Boashash, B., The bootstrap and its application in signal processing. *IEEE Signal Processing Magazine*, January, 15, No. 1, 56-76, 1998;

Politis, D.N., Computer-intensive methods in statistical analysis. *IEEE Signal Processing Magazine*, January, 15, No. 1, 39-55, 1998;

⁵ Nagaoka, S. & Amai, O., A method for establishing a separation in air traffic control using a radar estimation accuracy of close approach probability. *J. Japan Ins. Navigation* 82, 53-60, 1990;

Nagaoka, S. & Amai, O., Estimation accuracy of close approach probability for establishing a radar separation minimum. *J. Navigation* 44, 110-121, 1991.

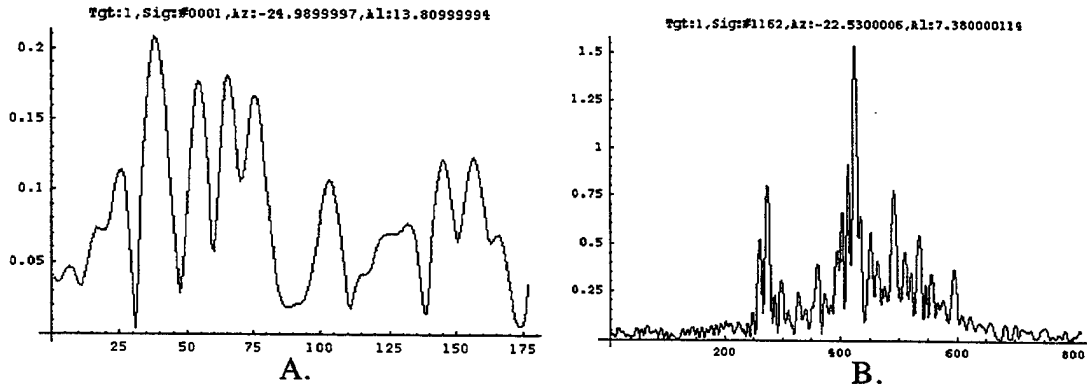


Fig. 14.1. Two radar return signals, A. and B.

The basic principle is that if $X = \{X_1, X_2, \dots, X_n\}$ is a sample - in the present instance it is a radar return signal - it may be considered as a collection of n numbers drawn at random from an unspecified distribution, F . If ϑ denotes a characteristic of F , e.g., its mean or variance, then if an estimator of ϑ , ϑ^* , were known, then ϑ could be judged to exceed a certain bound.

Put another way, the bootstrap procedure assumes that the sample X itself is the underlying distribution. By resampling from X many times and computing ϑ^* for each of the resamples a bootstrap distribution of ϑ^* is obtained that approximates the real distribution of ϑ^* and from which confidence intervals can be derived.

A way this can be done is if the X 's are considered to be independent and identically distributed random variables and are part of the sample distribution, F^* , which is considered close to the true distribution, F , i.e., F^* approaches F as $n \rightarrow \infty$.

Using a pseudorandom number generator, 100 samples of 177 values (Signal #1) and 812 values (Signal #2) were drawn, with replacement, from the Signals #1 and #2 (Fig. 14.1). The means and standard deviations of these samples were then calculated and sorted. The results are shown in Fig. 14.2, with mean standard deviations and confidence limits indicated.

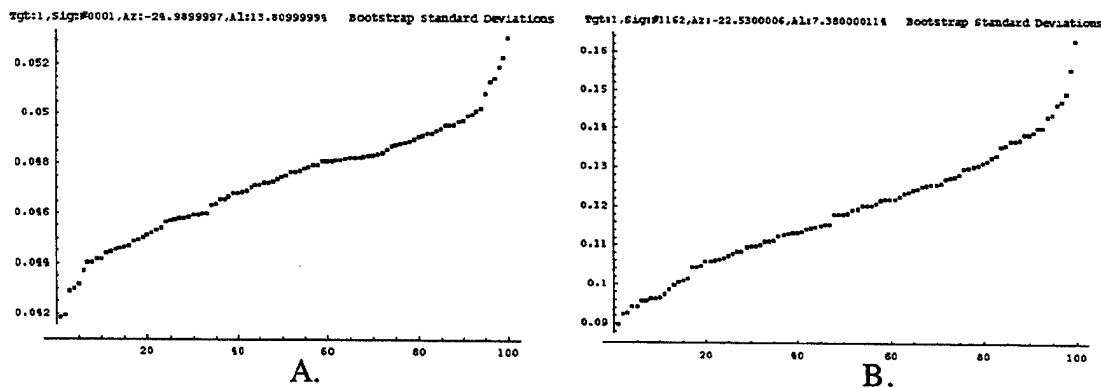


Fig. 14.2. Bootstrap Standard Deviations: 100 random samples, with replacement, from the radar signal returns. In A. the mean standard deviation is 0.0476 and the 95% confidence interval is (0.0419, 0.0539). In B. the mean standard deviation is 0.1154 and the 95% confidence interval is (0.09553, 0.15114).

The bootstrap method also is able to indicate skewness of distributions. Fig. 14.3 shows histogram plots of the data shown in Fig. 14.2 with superimposed probability density function of a Gaussian variable. It is evident that Signal #1 is skewed to the higher density values and Signal #2 to the lower.

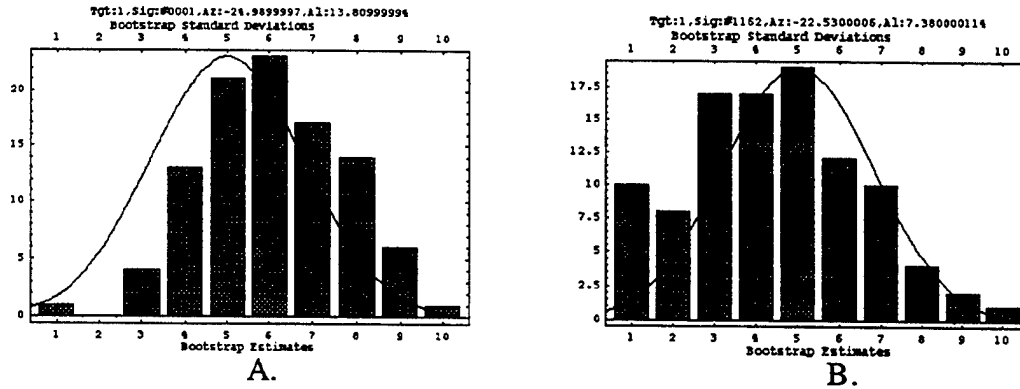


Fig. 14.3. Histograms of the bootstrap standard deviations based on random samplings of signal A. and signal B. The solid line indicates the probability density function of a Gaussian variable with a mean of 5.0 and variance 2.5.

14.1 Fractal Dimensions and Chaos

The power spectra of fractal processes in time reflect the statistical properties of those properties. Self-similarity means that there is a relationship between the power at the high frequencies (fine resolution) and the power at the low frequencies (coarse resolution). This relationship has power law scaling and the energy at a given frequency is proportional to $1/f^\alpha$. Therefore, $\log(\text{power spectrum}) = -\alpha \log(\text{spatial frequency})$, and α can be found from the slope of the power spectrum curve in log-log plots.

In the case of fractal processes, the total power at all frequencies in the power spectrum and the average power do not exist. If $\alpha \geq 1$, (as in Fig. 14.4, below), the total energy increases as the lowest frequency used to measure it decreases, or, the longer the interval of data that is analyzed, the larger the total power in the power spectrum. If $\alpha \leq 1$, the total power increases as the highest frequency used to measure it increases, or, the ever shorter intervals of data contain ever larger amounts of power.

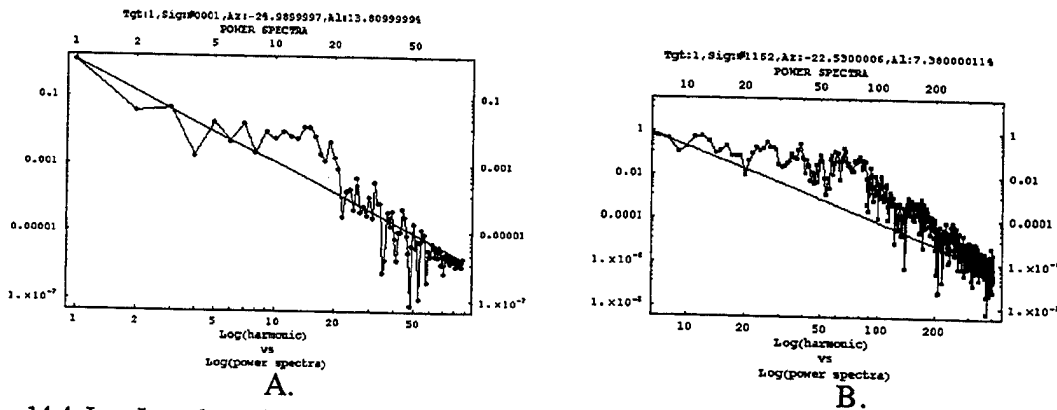


Fig. 14.4. Log-Log plots of spatial frequency versus the power spectrum. The solid line indicates the fractal power spectrum relation: $P(f) = 1/f^\alpha$. The slope of A is -2.98985; of B is -2.89493.

In the case of fractal processes, the moments (mean, variance, etc.) depend on the resolution used to measure them. Therefore, multiple sampling of the signals shown in Fig. 1 at different average temporal sampling windows, reveals the dependency of the moments on the sampling window resolution. The scaling relationship describes this dependency on the resolution and it is characterized by the *fractal dimension*, d . Again, calculating the slope of a *log-log* plot, this time of the moments, which for Fig. 14.5 are the standard deviations, versus the temporal sampling window, provides the method. The differing values of d are given in the caption to Fig. 14.5.

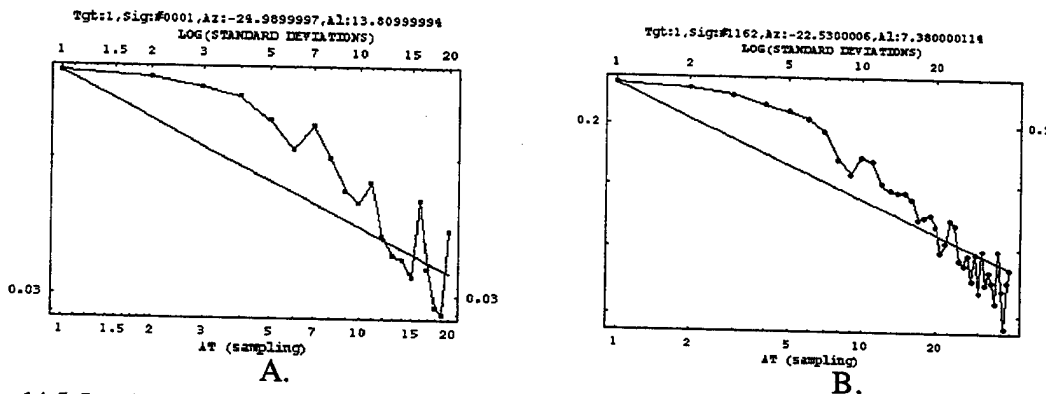


Fig. 14.5. Log-Log plots of the standard deviations versus sampling time windows. The solid line indicates how a moment - in this case the standard deviation, depends on the resolution (temporal sampling window duration) used to measure it. The slope of A is 0.1385; of B is 0.05425.

According to Takens' theorem⁶, the entire phase space set of a deterministic chaotic process can be constructed from one independent variable. A consequence of the theorem is that a deterministic chaotic process will exhibit a phase space set with increasing N , the dimension of the phase space, or the number of values of the data taken at a time to produce the phase space set (*the embedding dimension*). Thus, the fractal dimension of a deterministic chaotic process will reach a limiting value. However, if the process is random, the fractal dimension of the phase space set increases as the embedding dimension increases, i.e., as the number of values of the data taken at a time to produce the phase

⁶ Takens, in Rand & Young, (Ed.s) *Dynamical Systems and Turbulence*, Springer-Verlag, NY, pp. 366-381, 1981.

space set increases. In the case of the deterministic chaos process, the time series was generated by a finite set of independent variables, and in the case of a random process, the time series is generated by an infinite set of independent variables.

Fig. 14.6 shows that as the embedding dimension increases, both signals do not show a steadily increasing fractal dimension. Rather, both signals reach limiting values slightly less than 3. Thus, the time series for both signals were generated by a deterministic rule that can be described by 3 equations with 3 independent variables.

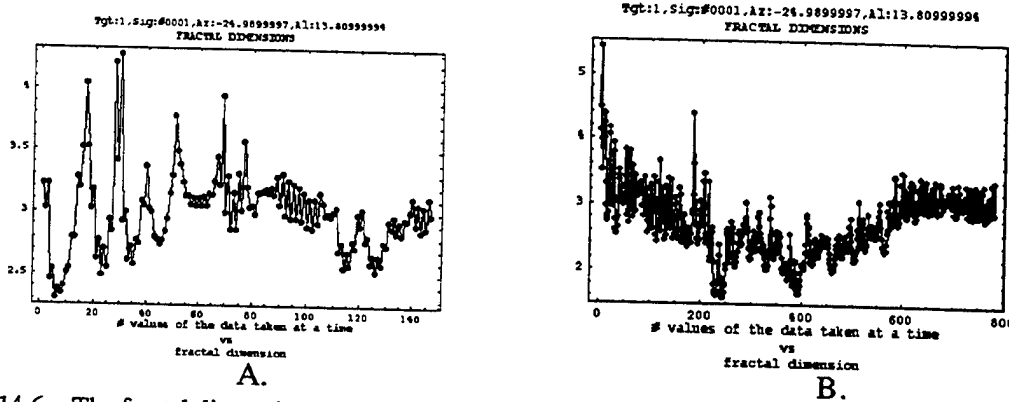


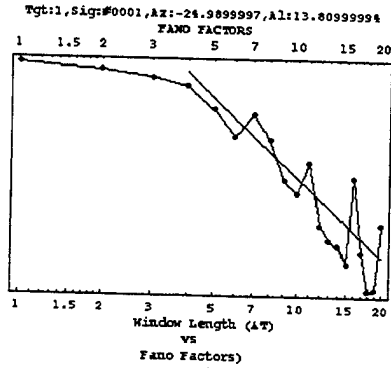
Fig. 14.6. The fractal dimension of a phase space set of a random time series increases as the embedding dimension increases. Here, it is shown that as the embedding dimension increases (= number of values of the data taken at a time to produce the phase space set), the fractal dimension of the phase space set approaches a limiting value. The fractal dimensions are of the power spectra as in Fig. 14.4 above. The final fractal dimension of A is 2.98985 which agrees with Fig. 14.4. The final fractal dimension of B. is 2.89493 which also agrees with Fig. 14.4.

As the statistical properties (e.g., the mean and variance) of a fractal time series depend on the resolution used to measure them, it is not appropriate to measure these statistical properties at only one resolution. However, it is appropriate to determine how these statistical properties depend on the resolution used to measure them. The *Fano Factor* is a statistical measure appropriate for measuring the statistical properties of fractal processes and is defined as the variance divided by the mean. The Fano Factor has a power law form that is proportional to r^b , where r is the resolution and b is related to the fractal dimension. Thus b can be calculated from the slope of a *log-log* plot of the Fano Factor versus the temporal length, $r = T$, of the sampling window of the time series. Fig. 14.7 shows such plots for both the signals of Fig. 1.

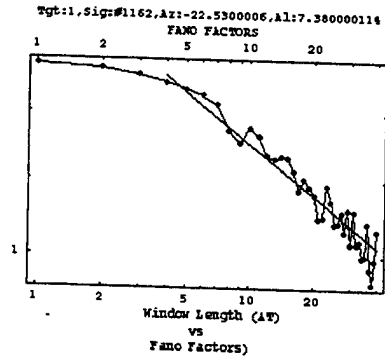
The fractal dimension, d , is related to b by:

$$d = \frac{\beta - b}{\alpha},$$

where α and β are exponents determining how the measured property depends on the number of samples and the resolution. We have established (Fig. 14.6) that the process generating the signals is deterministic chaotic and described by 3 independent variables. Therefore $\beta = 3$ (and $\alpha = 1$). From the values for b calculated from Fig. 14.7 and shown in the caption, we calculate $d = 3.27$ (Signal #1) and $d = 3.09$ (Signal #2), which values are different by 9% and 7% from those values for d shown in Figs 14.4 and 14.6, or within the range of acceptable error.



A.



B.

Fig. 14.7. The Fano factor, F , is equal to the variance divided by the mean. Here are Log-Log plots of the Fano Factor as a function of the temporal length of the sampling windows. There is a power law relationship of the Fano factor with respect to the temporal sampling window length, $T: F = T^b$, where b is related to the fractal dimension (solid line). In the case of A. $b = -0.268646$ B. In the case of B: $b = -0.0939912$.

15.0 Summary Recommendations

As was stated in **1.3 State of the Art Benchmark from which BSEI Research Proceeds**, we have sought to either identify or create methods different from state-of-the-art for solving the BMDO problem of providing an ultrahigh resolution sensor which can identify missile from decoy. We advocate sensor/radar systems using pulses shorter than the length of the target, adaptive time-frequency analysis methods which preserve target backscattering centers and resonances, and pattern identification of target and decoy.

In particular, we have created

- extensions of the Gabor transform (CQOW)
- adaptive methods
- methods involving the instantaneous phase
- mutual information methods
- Zak transform methods

which can achieve preserve target backscattering and target resonance and provide the input for procedures permitting pattern identification of target and decoy.

Furthermore, we have created methods using

- the bootstrap
- fractal dimension
- Fano number
- deterministic chaos methodologies

to provide precision in identification of target and decoy.

Our recommendation for the next step to be taken is to implement these new methods in emulation or real-time systems.